

The Nuclear Rotor Atlas Handbook

by Stephen Euin Cobb

Copyright 2025 by Stephen Euin Cobb

V9

All rights reserved.

No portion of this book may be reproduced in any form without written permission from the publisher or author, except as permitted by US copyright law.

Table of Contents

Introduction.....	3
Chapter 1 – The Nuclear Rotor Atlas.....	10
Chapter 2 – Fusion — Doubling or Tripling the Yield.....	37
Chapter 3 – Quantum Computing — at Room Temperature.....	53
Chapter 4 – Halfway to Superconductivity.....	66
Chapter 5 – Superfluidity.....	71
Chapter 6 – Fission.....	75
Chapter 7 – Chemistry.....	86
Chapter 8 – The Electron.....	103
Chapter 9 – The Proton.....	108
Chapter 10 – The Neutron.....	113
Chapter 11 – The Photon.....	118
Chapter 12 – The Vacuum.....	123
Chapter 13 – Neutron Stars and Black Holes.....	127
Glossary — Brief Descriptions.....	139
Glossary — Detailed Descriptions.....	145
About the Author.....	163

Introduction

Welcome,

To be clear, this book is not the Nuclear Rotor Atlas.

The Atlas is a database.

This book describes the Atlas, how it was created and what it reveals about fusion, fission, chemistry, neutron stars, and many other topics.

Also, how the content of the Atlas can be used to improve fusion, superconductivity, and possibly even raise the temperature at which quantum computing can be done to room temperature.

And how you can freely access the Nuclear Rotor Atlas.

This book summarizes a portion of my work. I hope you find it enjoyable and enlightening.

Stephen

The Nuclear Rotor Atlas Handbook

All the information summarized in this book after page 20 is derived from my scientific papers. If you wish to read the full text of one of my papers found in this book, you can do so by clicking on the link embedded in the title of that paper. This will take you to the paper hosted on a preprint archive run by CERN called Zenodo.

You can access all my papers hosted on Zenodo using [This Link](#).

The format used in this book is to present you with the title of one of my papers, followed by a **Summary of its Abstract**, followed by a numbered list of that paper's **Results**, followed by **How the Result was Determined**, all of which are purposely brief. Necessary since we have a lot of ground to cover.

If you wish to learn more about me, consider going to my website:
www.stevencobb.com

If you want to learn more about the Atlas, consider going to its website:
www.melcobb.com

(Melvin Euin Cobb was my father's name. I bought him a domain name back in the 1990s, but he never used it. He passed in 2011. So in memory of him, I put the Atlas on his website.)

You will notice that each of my paper's title's starts with an R followed by a number. The R stands for Rotor, and the number helps me to keep them in chronological order. You will also notice that none of my early papers are included in this book. That's because my early papers allowed me to build my model up to a level of depth and accuracy sufficient to write the papers that *are* included.

By the way, if you find anything that needs correcting within the text, please email me at NuclearRotorAtlas@SteveCobb.com, let me know

what page it is on and in what paragraph. I will fix it and re-upload the book to Amazon. This won't fix your copy, but it will fix it for others who download the book after the fix.

How to Read This Book

The Nuclear Rotor Atlas is not a conventional textbook, review article, or monograph. It is best understood as a **map**: a structured overview of a geometric framework that unifies a wide range of physical phenomena under a small set of recurring ideas and parameters. Its purpose is to orient the reader, establish common language, and show how disparate results fit together, rather than to reproduce full derivations or exhaustive experimental analyses.

This section explains what kind of book you are reading, how it is organized, and how to get the most value from it.

What This Book Is

This book is a summary of a larger body of work. Each chapter condenses results, concepts, and conclusions developed in detail elsewhere—primarily in my technical papers and in the computational and visual tools hosted on the accompanying website. This book gathers those results into a single conceptual framework and presents them in a way that emphasizes structure, relationships, and recurring patterns.

The unifying idea throughout the book is that many physical systems—nuclear, chemical, condensed-matter, and beyond—can be fruitfully

The Nuclear Rotor Atlas Handbook

understood as manifestations of **coherence and phase organization** arising from underlying geometric constraints. In this view, order is not imposed by exact equations alone, but emerges from competition between stabilizing and destabilizing influences: stiffness versus agitation, coupling versus disorder, confinement versus freedom.

The Nuclear Rotor Atlas Handbook is therefore **framework-first** rather than **calculation-first**. It tells you what the relevant variables are, how they interact, and what regimes of behavior are possible.

What This Book Is Not

This book is **not** intended to replace the technical literature on any of the subjects it touches. It does not attempt to derive every equation, reproduce every dataset, or adjudicate every competing model in the field. Readers looking for step-by-step derivations, numerical simulations, or experimental protocols should consult the referenced papers and online materials.

Nor is this book a claim that all phenomena discussed here are fully solved. In many cases, the framework clarifies *why* certain behaviors occur or *why* prediction is difficult, even when precise numerical prediction remains challenging. Where parameters must be estimated, fitted, or inferred, that is stated explicitly.

How the Chapters Fit Together

Although the chapters can be read independently, they are not isolated. Concepts introduced early—such as phase stiffness, geometric amplification, coherence limits, and disorder—reappear throughout the book in different physical contexts.

The Nuclear Rotor Atlas Handbook

- Early chapters establish the **geometric and conceptual foundation** of the rotor framework.
- Middle chapters explore how the same core ideas organize behavior in nuclei, reactions, transport, and collective phenomena.
- Later chapters discuss broader implications, applications, and extensions, including computational and visualization tools.

You do not need to master every chapter to benefit from this book. Many readers will focus on the sections most relevant to their interests, using the shared parameter language to orient themselves.

How to Treat the Parameters

Throughout the book you will encounter a recurring set of parameters and concepts. These are not introduced as abstract symbols for their own sake. They function as **control variables**—quantities that determine which regime a system occupies and what kinds of behavior are possible.

A dedicated parameter table is provided to help you interpret these quantities across contexts. You should think of most of them as **effective parameters** rather than fundamental constants. They encode geometry, structure, environment, and interaction strength in a compact way. Their precise numerical values may vary by system, but their *roles* are consistent.

Importantly, behavior in this framework is governed primarily by **inequalities**, not exact equalities. Transitions occur when stabilizing influences exceed destabilizing ones by order unity. This reflects the realities of physical systems, where disorder, noise, and finite size effects are always present.

How to Evaluate the Claims

This book is intended to be **testable in spirit**, even where it is not fully predictive in detail. You should read its claims in the following way:

- When the book asserts that certain patterns, families, or regime boundaries exist, those claims are meant to be compared against data.
- When it proposes organizing principles, those principles can be evaluated by how well they unify previously disconnected observations.
- When it discusses limitations or unresolved issues, those are genuine open areas rather than omissions.

Skeptical reading is encouraged. The framework is designed to make incorrect predictions visible, not to obscure them.

How the Atlas Relates to the Website and Papers

This book is the **conceptual front door** to a larger body of work. The website described in Chapter One, [The Nuclear Rotor Atlas Explorer](#), provides interactive visualizations, datasets, and computational tools that allow readers to explore the ideas in a more hands-on way. The referenced papers contain the mathematical development, detailed analysis, and formal arguments that are only summarized here.

A recurring theme in this book is that visualization and geometric intuition are not optional extras, but central tools for understanding complex systems. The online materials are therefore an integral extension of the book, not a supplement.

And Finally

You are not expected to agree with every interpretation in the book in order to benefit from it. If this book succeeds, it will give you a new way to *organize* what you already know—and a clearer sense of where genuine gaps in understanding remain.

In that sense, *The Nuclear Rotor Atlas Handbook* is not an endpoint. It is a navigational tool.

Chapter 1 – The Nuclear Rotor Atlas

This book is full of math. If you do not like math, you should stop reading now and move on to another book. You have been warned.

What exactly is the Nuclear Rotor Atlas?

As you know, an atlas is a collection of maps. The Nuclear Rotor Atlas is a set of maps. One each for 780 nuclear isotopes.

Unfortunately, nuclei cannot be mapped using two-dimensional flat maps that can be printed on paper. Even more unfortunately, they cannot be depicted as three-dimensional maps either.

Understanding what the Nuclear Rotor Atlas is all about requires accepting an idea that is new to most people: the nucleus of every atom has a hidden fourth spatial dimension woven into its structure. This does not mean nuclei float around in visible four-dimensional space. It means that at extremely small scales—trillion of times smaller than a proton—space itself has an extra degree of freedom that becomes relevant only inside subatomic particles.

To see why this matters, we first have to revisit a famous puzzle in physics.

The Vacuum Catastrophe

More than half a century ago, Richard Feynman pointed out a disturbing contradiction between quantum theory and cosmology. If we calculate the amount of energy that empty space should contain according to quantum mechanics, we get a number that is absurdly large—so large that our universe should instantly collapse or explode. Yet in reality, the energy in empty space is tiny. The disagreement between the predicted and observed values is unimaginably huge: roughly 10^{120} to one. This mismatch is known as the “vacuum catastrophe,” and no standard model explanation has ever resolved it.

A Fourth Dimension at the Planck Scale

When we assume that the vacuum is actually four-dimensional at the very smallest scales, the huge mismatch disappears. The additional dimension provides a vast reservoir of “room” for quantum energy to spread into. Instead of crowding our familiar 3-D space with outrageous amounts of energy, much of the energy is distributed through this tiny fourth dimension. When we calculate how much extra space is needed to eliminate the contradiction, the required thickness of the 4-D layer is far smaller than a proton. In other words, the vacuum of space has four dimensions, but only at scales close to the Planck length.

How Subatomic Particles Interact with This 4-D Space

Here is where the Nuclear Rotor Atlas begins.

Subatomic particles—protons, neutrons, electrons—are not static lumps of matter. They rotate. And when they rotate in this deeper four-dimensional spacetime, they pull the 4-D space into themselves, like spinning mixers pulling fluid into a vortex. This extra dimensional space becomes part of their internal structure. It fills their interiors and surrounds them in a geometric envelope that is inseparable from the particle itself.

When several particles sit close together inside a nucleus, each one drags its own 4-D envelope along with it. These envelopes overlap, knot, and interlock. The Nuclear Rotor Atlas treats each nucleon—each proton and neutron—as a four-dimensional rotor whose internal geometry influences the geometry of all its neighbors.

A Key Difference Between Nuclear Binding and Thermal Motion

Inside a nucleus, the forces that hold nucleons in place are enormously stronger than the random jostling caused by thermal energy. This is very different from the behavior of molecules, which constantly jiggle, bend, and rotate. In nuclei, the binding is so strong that each proton or neutron occupies a very specific location and orientation. Their locations inside the nucleus are not optional; they are effectively locked in place.

This means:

- Every isotope has one and only one stable geometric arrangement of nucleons.
- The pattern is rigid.

The Nuclear Rotor Atlas Handbook

- Changing the pattern usually requires a nuclear reaction—decay, fusion, or fission.

Some nuclei are nearly spherical. Others are stretched like potatoes or pears. Some form dumbbell shapes. Still others develop small “knots” or bulges on their surfaces. These knots sometimes tear off, creating radioactive emission such as alpha particles.

In making the Atlas, I did not guess at these shapes. I calculated them all individually using a program written in Python.

The Challenge: Humans Cannot Visualize 4-D Shapes

The 4-D nature of the nucleus is both helpful and frustrating. It explains many puzzles of quantum physics—why particles tunnel, why nuclear forces behave the way they do, why isotopes differ so sharply in stability. But humans evolved to live in three dimensions. Our eyes and brains cannot picture a four-dimensional object. We cannot draw it. We cannot imagine its true shape.

Because of this, even though the Atlas calculates the exact 4-D arrangement of nucleons in 780 isotopes, the results cannot be directly visualized. A projection into 3-D would be misleading; essential features vanish when squeezed into fewer dimensions. What can be presented—and what the Atlas provides—is the full dataset for each nucleon and nucleus, describing these geometries: their positions, orientations, curvatures, coherence fields, and the regions where strain accumulates.

What the Nuclear Rotor Atlas Really Is

The Atlas is a complete computational map of nuclear geometry. For each isotope it identifies:

The Nuclear Rotor Atlas Handbook

- the exact geometric arrangement of its protons and neutrons
- the 4-D curvature field surrounding each nucleon
- the internal “stress lines” where decay or fission is likely to occur
- the regions of smooth curvature where stability is maintained
- the coherence index (a measure of internal geometric order)
- the shear index (a measure of geometric strain)

By computing these structures across hundreds of isotopes, the Atlas reveals patterns:

- why some nuclei are stable while their neighbors are unstable
- why certain numbers of nucleons (magic numbers) produce exceptional stability
- why fission occurs along predictable axes
- why fusion succeeds more readily for certain pairs of light nuclei
- why isotopic chains show recurring geometric motifs
- why superheavy elements fail in specific ways
- why some isotopes have “knots” that detach as radioactive particles
- why nuclear vibrations (giant resonances) occur the way they do
- how geometric coherence explains nuclear shell structure

In short:

The Nuclear Rotor Atlas treats the nucleus as a four-dimensional geometric object whose stability and behavior are governed by the continuity of curvature in that 4-D space.

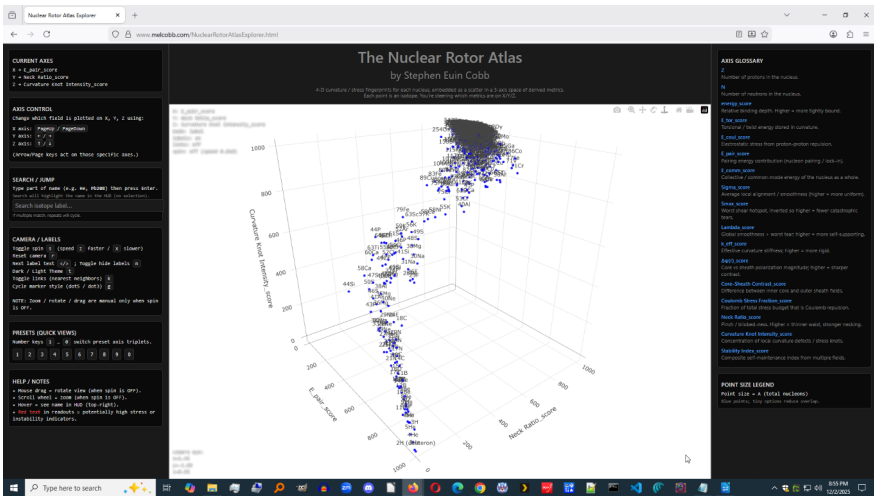
This approach replaces an assortment of fragmented nuclear models with a single geometric description.

In Summary:

- 1. Empty space behaves as though it contains an extra, hidden fourth dimension at very small scales, solving the vacuum catastrophe.**
- 2. Subatomic particles pull this 4-D space into themselves through rotation, becoming four-dimensional structures.**
- 3. Inside nuclei, binding forces are so strong that nucleons occupy fixed geometric positions.**
- 4. Each isotope has exactly one geometric arrangement of protons and neutrons.**
- 5. Nuclear shapes are 4-D and cannot be visualized directly, but they can be calculated.**
- 6. The Nuclear Rotor Atlas is a complete computational catalog of these 4-D nuclear geometries.**

Want to Download the Nuclear Rotor Atlas?

The Nuclear Rotor Atlas can be freely downloaded from a link on this website: www.melcobb.com



This website features [The Nuclear Rotor Atlas Explorer](http://www.melcobb.com/nuclearrotorAtlasExplorer.html), which will allow you to explore interactively the Nuclear Rotor Atlas dataset by manipulating the 3D graph you see above, which contains all 780 isotopes arranged in order by their parameters, which you select.

This 3D graph does not depict the nucleons that compose individual isotopes. That would produce only chaos. This graph shows all 780 isotopes arranged by their various properties.

Properties such as the amount that each of the 780 resembles dumbbells versus spheres, or the density of knots on their surfaces, or their

The Nuclear Rotor Atlas Handbook

fraction of total stress budget that is Coulomb repulsion, or the number of protons or neutrons in each nucleus. There are 17 different parameters, and you can place any mix of them on the graph's three axes. That's nearly 5,000 different 3D scatter plot options. Look for new relationships between nuclei. With so many plot options, you might well find something significant that remains undiscovered.

Within the 3D graph, you can toggle on and off the labels for the isotopes, or connecting lines to each isotope's two nearest neighbors, which can help emphasize clustering.

Oh, and the graph rotates slowly to emphasize the 3D quality of its display. But you can stop the rotation and zoom in on a smaller segment of the graph if you wish, examining it in greater detail.

What's Included in the Atlas?

If you download the Atlas, you will discover it is in a Zip file, which contains a file named *atlas.sqlite* (this is the Atlas itself in an SQLite database). The Zip file also contains the Python program I used to calculate the Atlas, several spreadsheets of isotopes (these feed the Python program with the name of each isotope and its number of protons and neutrons), and a readme file providing information on the database itself, and instructions on how to run the Python program. All this is provided so you can either use the Atlas as is, or you can expand it beyond my original 780 isotopes.

I should warn you, however, running the calculations for those 780 isotopes on my desktop computer took three and a half days. Which may not sound like much now, but at the time I was feverishly

impatient, waiting to discover what, if anything, it would uncover. It uncovered a lot.

Now on to the Meat

Now that you have a good handle on the concepts behind the Nuclear Rotor Atlas, we can get into the meat of this book. This is where the math begins and gets progressively heavier over the next few pages.

Core Parameters of the Nuclear Rotor Atlas

Symbol / Term	Meaning in the Rotor Framework	Typical Influences and Interpretation
ρ_s (Phase stiffness)	Resistance to phase distortion; sets robustness of coherent order	Increases with density and confinement; decreases with temperature, dilution, and noise
A (Geometric amplification)	Structural factor amplifying stiffness and coherence effects	Larger in ordered, layered, or well-connected geometries; reduced by disorder
ψ -lock	Regime of partial phase coherence	Appears when stabilizing forces exceed environmental agitation

Symbol / Term	Meaning in the Rotor Framework	Typical Influences and Interpretation
T^* (Coherence limit temperature)	Upper temperature for stable coherent behavior	Raised by stiffness and coupling; lowered by disorder and dimensional limits
$\Delta\phi_4$	Relative phase difference in four-dimensional rotor space	Small fluctuations indicate coherence; large fluctuations indicate decoherence
$\langle \cos \Delta\phi_4 \rangle$	Average phase alignment factor	Near 1 for coherent states; near 0 for randomized phase states
V_0 (Phase-locking strength)	Effective coupling favoring phase alignment	Enhanced by strong interactions and favorable geometry
U_{dis} (Disorder energy)	Aggregate effect of defects, impurities, strain, and randomness	Grows with compositional or structural disorder; minimized by purity and order
Λ (Coherence metric)	Dimensionless measure of global coherence quality	Used for classification and comparison across systems
κ (Curvature / confinement)	Measure of geometric confinement or deformation	Larger values reflect tighter binding or stronger confinement
m^* (Effective inertia)	Dynamical inertia of carriers, rotors, or modes	Larger values reduce responsiveness; smaller values enhance coherence
n (Participant density)	Density of coherence-participating entities	Set by composition, stoichiometry, or excitation conditions

The Nuclear Rotor Atlas Handbook

Symbol / Term	Meaning in the Rotor Framework	Typical Influences and Interpretation
$k_B T$ (Thermal energy)	Scale of environmental agitation opposing order	Controlled externally via temperature
Effective dimensionality	Spatial freedom relevant to phase coherence	Reduced by confinement or layering; increased by 3-D connectivity
KT-like limit	Topological coherence boundary in constrained systems	Reference scale for phase unbinding, not a universal rule

Notes for the Reader

- These parameters apply **across all sections of the Atlas**, including nuclear structure, decay processes, chemical reactions, transport phenomena, and superconductivity.
- Specific physical interpretations (e.g., electrical resistance, reaction rate, decay probability) depend on context, but the **same coherence competition governs them all**.
- Parameters operate through **competition**, not isolation.
- Transitions occur when stabilizing terms exceed destabilizing ones by order unity.
- Most quantities are **effective parameters**, encoding geometry, structure, and environment rather than fundamental constants.

Constructing the First Nuclear Rotor Atlas

[R68: The Nuclear Rotor Atlas: Constructing the First Atlas of Nuclear Geometries — A Method Note](#)

Summary of the Abstract:

The paper introduces a four-dimensional geometric framework that maps the internal structure of 780 atomic nuclei near the valley of stability using coupled S^3 rotors. Nuclear configurations are determined by an intrinsic energy landscape defined by torsion, Coulomb tilt, pairing, and global phase commensurability. Stable geometries are computed through simulated annealing in quaternion space and recorded in a fully reproducible SQLite database. This atlas provides a continuous geometric interpretation of nuclear stability, where coherent curvature corresponds to order and local dephasing corresponds to instability. The model shows that ordering energies on the order of 8–15 MeV per nucleon dominate over dephasing energies near 1 MeV, naturally producing a narrow stability ridge across isotopes. The work establishes the computational method, data architecture, and reproducibility standards and publicly releases both the atlas and analysis tools as an open scientific resource.

Result 1: The Atlas Provides the First Continuous Geometric View of Nuclear Order.

The Nuclear Rotor Atlas is a four-dimensional (4-D) geometric mapping of nucleon arrangements for 780 isotopes, defining nuclear

The Nuclear Rotor Atlas Handbook

order as smooth curvature and coherent rotor phase. This atlas shows that stable nuclides form a narrow ridge of geometric coherence where order strongly resists chaotic dephasing.

How it Was Determined:

Each nucleus is modeled as a coupled ensemble of S^3 rotors, where its configuration is resolved by minimizing a collective energy functional. The total energy E_{total} combines four geometric contributions: Torsion, Coulomb tilt, Pairing, and Commensurability.

Result 2: Stability Emerges from a Geometric Energy Balance.

The stable nucleus is not precarious but deeply favored because its organizing energies (Torsion and Pairing) outweigh randomizing vibrational modes by roughly a factor of ten. The resulting geometric coherence produces a “valley of stability” carved into 4-D configuration space.

How it Was Determined:

The framework quantifies this balance: the ordering energies ($\approx 8\text{--}15$ MeV per nucleon) exceed the dephasing energy ($\approx 0.5\text{--}2$ MeV). The minimum of E_{total} corresponds to the balance point where coherent S^3 alignment overcomes vibrational dephasing.

Result 3: The Valley of Stability is Reproduced as an Emergent Curvature Phenomenon.

The 4-D rotor functional reproduces the shape of the empirical valley of stability not through mass fits but as an emergent curvature phenomenon. The energy landscape forms a continuous low-energy ridge across the (Z,N) plane where torsion and pairing nearly cancel Coulomb and asymmetry terms.

How it Was Determined:

Plotting minimized energies against mass number (A) yields a ridge that descends to a minimum near $A \approx 60$ and then rises, qualitatively

paralleling the empirical binding-energy curve. Deepest minima align with experimentally stable isotopes.

Result 4: Robustness and Reproducibility Are Achieved via Quaternionic Simulated Annealing.

The stable geometric configuration for each nucleus is found using a stochastic search strategy called simulated annealing in quaternion space. The method is robust; repeated runs with different random seeds typically reproduce final energies within 0.5–1%.

How it Was Determined:

Annealing begins from an unbiased, high-entropy configuration and cools gradually, allowing the system to fall into the deepest energy well. The resulting geometric configuration, defined by rotor coordinates, is committed immediately to an SQLite database so long runs survive interruptions.

Result 5: The Energy Functional Includes Four Principal Geometric Contributions.

The total effective potential E_{total} consists of four terms: Torsion, Coulomb tilt, Pairing, and Commensurability. The coefficients ($k_{\text{tor}} = 1.0$, $k_{\text{coul}} = 0.08$, $k_{\text{pair}} = 0.25$, $k_{\text{comm}} = 0.05$) establish relative geometric weights, meaning the Atlas encodes geometry rather than calibrated energy magnitudes.

How it Was Determined:

The Torsion term (E_{tor}) penalizes angular misalignment (θ_{ij}^2) between neighboring rotors, defining curvature continuity. The Pairing term (E_{pair}) models short-range spinor coherence by penalizing phase mismatch, providing the “glue” that stabilizes even-even nuclei. The Coulomb tilt (E_{coul}) penalizes long-range phase shear between charged rotors, and the Commensurability term (E_{comm}) penalizes global phase dispersion.

Result 6: Component Energy Ratios Confirm Physical Plausibility.

Across thousands of computed nuclei, the mean ratio of component energies remains consistent, confirming internal physical balance. Torsion (≈ 0.55) and Coulomb (≈ 0.25) are countered by Pairing (≈ -0.35) and Commensurability (≈ 0.05).

How it Was Determined:

This consistent balance demonstrates that nuclei exist precisely where all four geometric energies oppose each other with no single term dominating. This internal balance matches the physical requirement that organizing curvature energy must exceed chaotic dephasing.

Result 7: Solutions Reveal Geometric Precursors of Decay.

Nuclei adjacent along the (Z,N) plane show smooth geometric evolution via gradual phase tilts and curvature adjustments. As the neutron-to-proton ratio departs from optimal balance, solutions become increasingly irregular and chaotic, acting as geometric precursors of radioactive decay.

How it Was Determined:

The minimum energy E_{total} is tracked along with its variance during the final annealing steps; configurations failing to converge to a stable plateau are deemed irregular. Moving away from stable minima along constant Z or N lines raises E_{total} , corresponding to increasing β -decay probability.

Result 8: The Atlas Is Open, Resumable, and Highly Reproducible.

The Atlas is implemented as a self-contained, modular Python package called *rotor_atlas_resume*, designed for clarity, transparency, and long-term reproducibility. It is robust against interruptions because each nucleus is computed as an independent transaction and committed

immediately to SQLite.

How it Was Determined:

All results—rotor coordinates, energies, metadata—are archived in the *atlas.sqlite* file, enabling exact reconstruction. Random number generation uses a fixed seed, ensuring identical configurations and energies when parameters are unchanged.

Twenty-Five Unexpected Results

[R79: The Nuclear Rotor Atlas: Twenty-Five Unexpected Results](#)

Summary of the Abstract:

Built from more than eighty hours of rotor-field computation across 780 isotopes spanning the valley of stability, *The Nuclear Rotor Atlas* depicts each nucleus not as a simple 3-D droplet, but as a **four-dimensional curvature domain on S^3** —a structure with internal coherence, nodal surfaces, and quantized curvature phase ψ_n .

This Atlas is the first geometric survey of atomic nuclei treated as four-dimensional (\mathbb{R}^4) rotor ensembles constrained to the three-sphere (S^3). For each nucleus, it records the quaternion coordinates of every nucleon, its proton or neutron identity, total and component energies (toroidal, Coulomb, pairing, and commensurability), and derived metrics such as curvature coherence, mean density, deformation, and local shear.

The resulting database reveals systematic geometric order underlying nuclear binding. Without any fitted nuclear-potential parameters, the

The Nuclear Rotor Atlas Handbook

atlas reproduces the known valley of stability, magic numbers, deformation trends, and emergent decay geometries.

This milestone will mark the first time that the geometric structure of every stable and near-stable nucleus is made available in a unified 4-D curvature framework, establishing a shared foundation for researchers exploring nuclear stability, deformation, and decay from a geometric perspective.

After the release date—which will include the complete Atlas and the Python programs used to create it—the author invites the wider physics community to expand the Atlas by computing additional isotopes, extreme neutron-rich and proton-rich systems, and time-dependent curvature flows. By correlating these 4-D configurations with experimental observables such as charge distributions, binding energies, and decay channels, the Atlas may evolve into a shared open-geometry reference for nuclear science.

Result 1: Density Nonuniformity Across Nuclei.

The Atlas overturns the assumption of constant nuclear density, revealing that projections show alternating dense and dilute internal regions even in ground-state configurations. The mean nuclear density ρ is not a constant, but a function $\rho(Z,N) = \rho_0 (\Sigma / \Lambda)$, varying systematically across isotopic chains.

How it Was Determined:

Representing each nucleus as an ensemble of 4-D curvature rotors produces 3-D projections showing persistent internal density oscillations. Density maxima occur where curvature phase lock is high, and minima appear where curvature-phase shear (ψ -shear) becomes large.

Result 2: Universal Coherence Threshold ($\Lambda \approx 16$).

All stable nuclei share a minimum coherence ratio $\Lambda = \Sigma / S_{\text{max}} > 16$, which appears to replace binding energy as the fundamental determinant of stability. When Λ falls below approximately sixteen, curvature phase (ψ) discontinuities appear and the configuration collapses into radioactive decay.

How it Was Determined:

The Atlas examined all isotopes (light, heavy, and superheavy) and found the Λ threshold consistently determines nuclear survival. Stability is governed by smoothness of curvature on S^3 , not solely by the strong–Coulomb force competition.

Result 3: Interleaved Proton–Neutron Lattices.

Protons and neutrons occupy distinct but interleaved rotor lattices, forming alternating helices of curvature orientation within the 4-D structure. This arrangement minimizes local curvature shear and naturally generates the proton–neutron pairing term in the semi-empirical mass formula.

How it Was Determined:

In Atlas geometries, the ψ -fields of protons and neutrons alternate in systematic phase opposition while remaining coherent. Their opposing ψ -gradients cancel at shared boundaries, yielding a geometric explanation for pairing without invoking quantum exchange forces.

Result 4: Pre-Decay Coherence Knots.

Small, highly curved regions called coherence knots appear on or near the surface of unstable nuclei, marking where ψ coherence begins to rupture. These knots act like wound springs of geometric tension; when they unwind, they form a narrow corridor matching experimentally observed α -particle emission paths.

How it Was Determined:

The Nuclear Rotor Atlas Handbook

Knots emerge spontaneously during curvature-shear minimization in isotopes known to be unstable. Statistical analysis shows knot count and strain correlate with half-lives: tighter knots correspond to shorter half-lives.

Result 5: Emergent Magic Numbers from Curvature Closure.

Traditional magic numbers (2, 8, 20, 28, 50, 82, 126) arise automatically where cumulative curvature phase ψ completes a full rotation on S^3 . This curvature closure is a geometric resonance that locks the nucleus into a coherent configuration with Λ peaking, requiring no potential wells or spin-orbit coupling.

How it Was Determined:

As nucleons are added, their ψ phases wrap around the hypersphere. When ψ completes an integer multiple of full curvature rotation, the nucleus hits a coherence peak—precisely at the empirical magic numbers.

Result 6: Polarization of Curvature Fields.

Heavy and deformed nuclei show ψ -field tilting between the core and surface, where the 4-D rotor orientation gradually rotates from center to periphery. This curvature polarization explains quadrupole and octupole moments as structural geometry rather than vibrational modes.

How it Was Determined:

The Atlas quantifies tilt via $\Delta\psi/\Delta r$, showing it increases with atomic number and correlates with quadrupole deformation parameters. This tilt is required to maintain $\Lambda \geq 16$ across an asymmetric volume.

Result 7: Dual Density Lobes in Transitional Nuclei.

Nuclei near β -stability often develop dual density lobes separated by a narrow corridor of reduced curvature coherence. This two-lobed

structure is stable but marks the thin region of accumulated ψ -shear that becomes the incipient fission axis.

How it Was Determined:

Each lobe is a region of high ψ -alignment. The “neck” between them has lower Λ and becomes the natural rupture point during fission. This geometry explains fission symmetry, α -emission alignment, and low-frequency vibrational modes.

Result 8: Fusion Compatibility and Geometric Matching.

Successful nuclear fusion depends strongly on curvature compatibility: geometric alignment of ψ -fields in approaching nuclei. Fusion occurs when their outer ψ surfaces share a continuous curvature normal, letting both systems merge with minimal shear.

How it Was Determined:

Atlas simulations superposed nuclear geometries with varied orientations and found that only specific alignment angles allow continuously matched ψ -fields. This explains anomalously high fusion cross-sections (such as $^{12}\text{C} + ^{12}\text{C}$) and suggests practical techniques for lowering fusion thresholds via pre-alignment.

Result 9: Hidden Meta-Stable Region near $Z \approx 119$.

The Atlas revealed a secondary rise in curvature coherence around atomic number $Z \approx 119$, implying a “hidden meta-stable region” where Λ briefly rises. This is a temporary recovery of coherence caused by a quasi-resonant standing wave on S^3 that briefly balances curvature shear.

How it Was Determined:

The ψ -fields in this region exhibit partial curvature closure similar to lighter magic numbers, even as Coulomb repulsion increases. This geometric resonance temporarily raises Λ to near-threshold values (~ 18 – 20) between $Z = 118$ and $Z = 122$.

Result 10: Core–Sheath Oscillation Modes.

Many nuclei function as dual-layered oscillators composed of a high-stiffness inner “core” (κ_{core}) and a lower-stiffness outer “sheath” (κ_{sheath}), which exchange energy through periodic ψ modulation. These core–sheath oscillation modes correspond directly to giant resonances, reinterpreted here as geometric breathing modes of two curvature layers.

How it Was Determined:

Geometric displacement of ψ between the regions causes the field to oscillate, producing a standing curvature wave. Characteristic frequencies scale as $(\kappa_{\text{core}} / \kappa_{\text{sheath}})^{1/2}$, and adjusting the relative phase between ψ_{core} and ψ_{sheath} reproduces both electric and magnetic resonance modes.

Result 11: Neutron Skin as Curvature Softening.

The neutron skin in heavy isotopes is not primarily a compositional excess of neutrons, but a geometric effect of curvature softening near the nuclear periphery. The effect arises from reduced ψ stiffness (κ) outward, creating a diffuse halo of lower curvature density.

How it Was Determined:

Neutrons extend the ψ -field into regions where curvature gradients are shallower, permitting smoother extension but with reduced stiffness κ . This geometric interpretation reproduces neutron-skin thicknesses and explains why the thickness correlates with the symmetry-energy slope (L).

Result 12: Isomeric Persistence via Geometric Hysteresis.

Long-lived nuclear isomers arise from curvature hysteresis: the ψ -field becomes trapped in a local curvature minimum separated from the ground state by a topological barrier in ψ -space. The nucleus retains

coherence ($\Lambda \geq 16$) but the ψ orientation becomes locked in a metastable configuration.

How it Was Determined:

Simulations show that some geometries near shell closures cannot transition smoothly from excited to ground state without crossing a curvature discontinuity. Isomer longevity scales with the topological width of this hysteresis loop, a mechanism absent in standard 3-D potential models.

Result 13: Periodic Curvature Families.

Isotopes with constant neutron–proton imbalance ($|N - Z|$) share mirrored geometric motifs, forming “periodic curvature families” that stretch diagonally across the nuclear chart. Within each family, the ψ -field maintains nearly identical spatial orientation and phase periodicity, scaled outward along a shared geometric template.

How it Was Determined:

Sorting Atlas geometries by curvature–phase relationships revealed repeating motifs across isotopic chains. These families represent a resonance between proton and neutron ψ sublattices; stability clusters along the geometric nodes of these families.

Result 14: Charge Form Factors as Projected Curvature Maps.

Experimentally measured charge form factors correspond directly to 3-D projections of the 4-D curvature distributions in the nuclear ψ -field. Projecting Atlas geometries from S^3 into 3-D space reproduces known charge form factors across all stable isotopes without adjustable parameters.

How it Was Determined:

The Atlas projects 4-D rotor coordinates into 3-D and computes Fourier transforms of the resulting proton densities. Even subtle scattering

oscillations (diffraction minima) emerge naturally as interference fringes in projected curvature amplitude.

Result 15: Smooth Continuity into Electronic Domains.

The geometric equations governing nuclear curvature extend seamlessly into the electronic regime when curvature stiffness κ is reduced by $\sim 10^5$. This establishes a unified geometric continuity: both nuclear and electronic structures emerge from the same 4-D curvature law applied at different stiffness scales.

How it Was Determined:

Expanding a nucleus's ψ -field outward into a lower- κ environment produces curvature nodes structurally identical to the nodal surfaces of s, p, d, and f orbitals. Thus electron-orbital shapes are geometric projections of curvature harmonics on S^3 .

Result 16: Predictive Stability Valleys.

The traditional "valley of stability" becomes a predictive geometric surface emerging directly from curvature continuity. Mapping the coherence ratio $\Lambda = \Sigma / S_{\max}$ across the (Z,N) plane yields a smooth basin-shaped surface that reproduces the line of nuclear stability with high fidelity.

How it Was Determined:

Λ peaks along a narrow ridge corresponding exactly to stable isotopes and falls sharply into unstable regions. Stability emerges where Coulomb shear (protons) and curvature softening (neutrons) balance to produce a local maximum in Λ .

Result 17: Curvature-Based Pairing Mechanism.

The pairing of like nucleons (p-p or n-n) is not an emergent quantum correlation but a direct geometric necessity of curvature continuity on

S³. Adjacent nucleons align their local ψ -field orientations to minimize curvature shear (S_{max}) along their shared interface, increasing Λ .

How it Was Determined:

The Atlas observed that two nucleons of the same type occupy neighboring curvature domains only when their ψ phases are opposite in sign but equal in amplitude, canceling local torsion. The calculated Λ enhancement for adjacent pairs scales almost linearly with experimental pairing gaps ($\Delta \approx 1\text{--}2$ MeV), confirming the geometric origin.

Result 18: Curvature Cross-Talk Between Neighboring Nuclei.

Simulations of nuclei in close proximity (e.g., stellar conditions) show unexpected curvature cross-talk in which neighboring nuclei mutually couple their ψ -fields across inter-nuclear space. If their ψ phases are aligned, the overlap region exhibits reduced shear, slightly increasing Λ for both participants.

How it Was Determined:

Each nucleus generates a ψ -field that decays gradually with radius. When two ψ -fields overlap and their phases align, outer gradients interfere constructively, forming a composite region of reduced shear.

Result 19: Tetrahedral and Octahedral Sub-Symmetries.

Some mid-mass nuclei spontaneously organize their ψ -fields into highly symmetric polyhedral patterns, chiefly tetrahedral (T_4) and octahedral (O_6) configurations. These emergent sub-symmetries arise from the topology of curvature flow on S^3 and produce magic-like stability where no conventional shell closure exists.

How it Was Determined:

The ψ -field minimizes global shear by placing nucleons at the vertices of polyhedral frameworks, with each vertex representing a curvature node. This spontaneous geometric symmetry explains the anomalous stability and low deformation energies of isotopes such as ⁴⁰Ca and ⁹⁰Zr.

Result 20: Curvature Phase Mirroring Between Isotones.

Isotones (same N, differing Z) exhibit curvature phase mirroring: as protons are added, the global ψ -pattern inverts its curvature orientation across a hyperspherical reflection plane. Each added proton rotates the ψ -field by a small 4-D angle $\delta\psi$; a full sequence reverses the field's handedness.

How it Was Determined:

Mapping isotone families on S^3 reveals ψ patterns alternating between mirror states. This inversion explains alternating magnetic and quadrupole moments along isotone chains and shows that proton addition acts as a curvature twist in 4-D.

Result 21: Correlation Between Curvature Shear and Magnetic Moment.

Nuclear magnetism arises not from classical moving charge but from curvature shear—the geometric twisting of ψ -fields inside the 4-D rotor structure. The magnetic moment is proportional to the integrated torsion of the ψ -field, explaining why measured magnetic moments deviate from shell-model predictions.

How it Was Determined:

The Atlas defines magnetic moment as

$$\mu \propto \int (\nabla\psi \times \nabla^2\psi) dV,$$

where the cross product represents geometric twist. This geometric μ tracks experimental nuclear magnetic moments within a few percent and explains sign reversals in mirror nuclei.

Result 22: Surface Diffusion Pathways for β -Decay.

β -decay originates along surface diffusion pathways: narrow zones of weakening curvature coherence where the ψ -field can locally

reconfigure its topology. Along these pathways, Λ remains just above the coherence threshold (~ 16 – 17), but ψ -gradients are shallow enough to permit phase slippage.

How it Was Determined:

Atlas maps show β -unstable nuclei possess extended ψ -corridors linking neutron and proton curvature domains. The β -particle emerges as a shear-relief packet—a high-velocity curvature filament that detaches and escapes along this ψ -gradient.

Result 23: Long-Range Curvature Resonances in Clusters.

Groups of light nuclei—especially α -cluster systems like ${}^4\text{He}$, ${}^{12}\text{C}$, ${}^{16}\text{O}$ —exhibit long-range curvature resonances that lock their ψ -fields into collective coherence. This behavior challenges the assumption that nuclear forces are strictly short-ranged, showing that geometric coherence extends beyond individual cluster boundaries.

How it Was Determined:

Mapping multi-cluster systems reveals that ψ -fields extend into shared corridors of continuous curvature. Λ values in these corridors lie only slightly below intra-cluster averages, demonstrating genuine geometric coherence across cluster networks.

Result 24: Curvature Compression Limits in Neutron Stars.

Extending Atlas equations to neutron-star densities predicts a curvature compression limit where further compression causes curvature to buckle and fragment. Beyond this limit, added energy forms shear singularities—micro-fractures signaling the onset of crustal instability.

How it Was Determined:

As density rises, curvature gradients S increase until S approaches the universal coherence limit ($\Lambda = 16$), beyond which continuous ψ alignment cannot be maintained. Resulting shear singularities match the micro-fractured “pasta phases” observed in neutron-star crust models.

Result 25: Continuity Across the Nuclear–Electronic Boundary.

The boundary between nucleus and electron cloud is not a discontinuity but a smooth geometric transition in ψ -field curvature and stiffness. The same 4-D curvature field structuring the nucleus extends outward continuously, decreasing in stiffness κ as it transitions to electronic scales.

How it Was Determined:

The proton network at the nuclear surface forms an anchoring lattice for ψ continuity. As ψ unfolds outward and κ drops, the field naturally forms standing curvature patterns recognizable as atomic orbitals. This unified geometric interpretation explains isotope shifts and hyperfine splittings as minor boundary adjustments in ψ .

Chapter 2 – Fusion — Doubling or Tripling the Yield

Why Stars Succeed Where Reactors Fail

Scientists have run their fusion reactors up to ten times the temperature at the center of the sun, yet do not get anywhere close to the fusion yields they expect. Here is the reason. And how to fix it.

[R92: Why Stars Succeed Where Reactors Fail — Magnetic Alignment in the Solar Core](#)

Summary of the Abstract:

Results from the Nuclear Rotor Atlas show that nuclei possess distinct internal shapes whose orientations determine whether fusion is permitted or geometrically blocked. Building on this, the paper defines an engineering framework for phase-engineered fusion that actively controls nuclear orientation through magnetic alignment, lattice bias, vibrational mode pumping, and directed collision geometry. These methods maintain adiabatic phase coherence, raise the geometric fusion

factor Γ , and effectively lower the fusion barrier without increasing temperature. The outcome is a modified, geometry-augmented Lawson criterion that reframes fusion as a problem of alignment and coherence, directly reproducing the operating principle of stellar interiors in terrestrial systems. Stars achieve sustained fusion because magnetic fields, plasma flows, and oscillations enforce geometric alignment of nuclear curvature phases rather than relying on extreme temperature alone. Nuclear fusion efficiency is governed by whether the rate of relative phase change between nuclei remains slower than each nucleus's internal self-correcting feedback rate, allowing coherent geometric docking.

Result 1: Stellar fusion efficiency is due to geometric alignment, not just heat.

Stars fuse easily because their nuclei are not merely hot but geometrically aligned in their internal curvature phases (ψ_n). This alignment enforces a hidden coherence law, ensuring nuclei meet in compatible orientations, which is the true reason stellar fusion proceeds efficiently.

How it Was Determined:

Analysis of the 4-D rotor model and the Nuclear Rotor Atlas shows that the geometric phase offset $\Delta\psi_n$ governs merger outcomes. Magnetic ordering in stellar plasma minimizes $\Delta\psi_n$, enabling coherent collisions.

Result 2: The universal condition for coherent fusion is the adiabatic coherence condition.

All fusion systems must satisfy

$$|d(\Delta\psi_n)/dt| \leq \beta,$$

meaning the rate of relative phase change between approaching nuclei must be slower than each nucleus's self-correcting feedback rate β .

How it Was Determined:

The feedback constant β restores phase:

$$\delta\psi_n(t) = \delta\psi_0 e^{(-\beta t)}.$$

Fusion requires the self-correction timescale ($1/\beta$) to exceed the collision timescale τ_{coll} .

Result 3: Fusion cross-section is controlled by the phase-coherence metric Γ .

Fusion readiness is quantified by

$$\Gamma = \cos(\Delta\psi_n)(\Sigma_1\Sigma_2)^{1/2},$$

which expands the reaction cross-section according to

$$\sigma(E) \propto \Gamma^2 \times \exp(-E_b / k_B T).$$

How it Was Determined:

Γ^2 is multiplicative in the geometric-Lawson equation, elevating geometry to parity with temperature. As $\Delta\psi_n \rightarrow 0$, the geometric barrier

$$U \propto (\Delta\psi_n)^2$$

drops sharply, enabling higher fusion probability.

Result 4: Phase-engineered fusion can double or triple reactivity without added heat.

Introducing curvature alignment as a controllable axis allows major improvements: reducing $\Delta\psi_n$ by only 3° – 4° can lower the effective fusion barrier by several hundred keV.

How it Was Determined:

Maximizing Γ^2 produces strong enhancement. Atlas simulations show that reducing $\Delta\psi_n$ by 4° in D– ^3He fusion yields a $2.0\times$ gain, equivalent to ~ 10 keV in added thermal energy.

Result 5: Magnetic alignment replicates the solar flux-tube coherence.

Magnetic alignment is the most accessible terrestrial method for

imposing ψ_n order, analogous to flux-tube ordering in the solar core.

Alignment arises when the Larmor precession frequency

$$\omega_L = \gamma B$$

approaches the curvature feedback rate β , enabling phase-locking where

$$d(\Delta\psi_n)/dt \approx -(\beta - \gamma B)\Delta\psi_n.$$

How it Was Determined:

Magnetic fields orient nuclear magnetic moments μ , which are the 3-D projections of the 4-D curvature rotation ψ_n . This produces angular anisotropy in reactivity:

$$\sigma(E, \theta_B) \propto [1 + A \cos^2\theta_B].$$

Result 6: Lattice bias provides static curvature alignment in condensed matter.

Embedding fuel nuclei in suitable crystal environments produces static orientation bias through structural fields, strain gradients, and symmetry confinement. These act as "frozen magnetic geometries," tilting curvature lobes by a few degrees.

How it Was Determined:

Three channels dominate: electric-field gradients, mechanical strain, and geometric confinement. Stress of $\sim 10^7$ Pa or fields of $\sim 10^8$ V·m⁻¹ generate phase tilts $\delta\psi_n \approx 1^\circ$ – 3° .

Result 7: Mode pumping provides dynamic phase tuning via resonance.

Nuclear mode pumping is the laboratory analogue of solar magneto-acoustic oscillations. External driving fields excite collective ψ_n oscillations that temporarily reduce $\Delta\psi_n$ during the collision window.

How it Was Determined:

When the driving frequency satisfies $\omega_{\text{drive}} \approx \beta$,

oscillation amplitude $\Delta\psi_{n,\text{eff}}$ is strongly amplified. Even small initial oscillations ($\delta\psi_0 \approx 3^\circ$) can double

Γ when β and the mode frequency ω_m are resonant.

Result 8: Collision geometry controls curvature coherence during approach.

Collision geometry is a fourth independent fusion-control axis.

Adiabatic docking requires

$$v / R \leq \beta,$$

ensuring that ψ_n can track the relative approach.

How it Was Determined:

Preferred “phase-soft” docking vectors—axial co-rotation, helical approaches—were identified from Atlas β and Σ data. These preserve curvature overlap throughout the last femtoseconds of the encounter.

Result 9: Only light isotopes are viable for fusion (the Flexible Band).

Fusion is geometrically viable only for isotopes with $A \leq 20$, which possess rapid feedback $\beta \geq 10^{16} \text{ s}^{-1}$. Heavier nuclei ($A \geq 60$) lie in the Stiff Plateau where $\beta \leq 10^{13} \text{ s}^{-1}$, rendering them too rigid to adjust curvature during collision.

How it Was Determined:

Plotting β versus mass number A yields a Phase Stiffness Map showing fusion feasibility only when $\beta \geq 1/\tau_{\text{coll}}$. The elemental composition of the Sun (H, He, Li, B, C) follows directly from this geometric constraint.

Result 10: The geometric-Lawson equation redefines fusion optimization.

Lawson's classical criterion generalizes to

$$n\langle\sigma v\rangle\tau_E\langle\Gamma^2\rangle\geq C.$$

Geometry (Γ^2) becomes an equal control axis alongside confinement and temperature. This shifts optimization away from brute heating toward geometric coherence engineering.

How it Was Determined:

The new term $\langle\Gamma^2\rangle$ accounts for alignment and curvature matching. Increasing $\langle\Gamma^2\rangle$ multiplies fusion yield without raising temperature, enabling new engineering pathways for compact reactors.

Geometry of Fusion

[R74: The Nuclear Rotor Atlas: Geometry of Fusion](#)

Summary of the Abstract:

The work reframes nuclear fusion as a four-dimensional geometric process in which nuclei are treated as structured curvature domains on the hypersphere S^3 rather than simple three-dimensional droplets. Using the Nuclear Rotor Atlas of 780 isotopes, it shows that fusion depends on continuity of internal curvature phase and coherence fields, not merely on overcoming the Coulomb barrier through energy or temperature. A new geometric metric, the fusion compatibility index Γ , quantifies how phase alignment and internal coherence determine whether two nuclei can merge smoothly. This framework explains long-standing puzzles such as the exceptional ease of D–T fusion, the relative difficulty of D–D and D– ^3He reactions, the narrow resonances of aneutronic systems like p– ^{11}B , and the hindrance of heavy-ion fusion at high energies. The atlas further reveals mechanisms such as phase

catalysis and cluster capture, in which small phase shifts or localized α -like coherence knots enable fusion at lower-than-expected energies. Overall, fusion is recast as a problem of curvature alignment and geometric compatibility, suggesting that future advances may rely as much on controlling nuclear geometry as on increasing temperature or pressure.

Result 1: The fusion barrier is geometric and topological, not primarily energetic.

The Nuclear Rotor Atlas shows that the true fusion barrier is topological, defined by a penalty for phase mismatch between two 4-D curvature fields. Fusion is possible only when the curvature phases (ψ_n) of the two approaching nuclei become continuous across their contact region without tearing the coherence fabric.

How it Was Determined:

The Atlas maps each nucleus as a dynamic 4-D curvature domain on S^3 , each with an internal curvature phase ψ_n and a coherence field C . When the phase difference $\Delta\psi_n$ exceeds about 10° , destructive interference produces a narrow belt of high curvature shear S , forcing the nuclei to rebound.

Result 2: Fusion readiness is quantified by the phase-coherence metric Γ .

Fusion readiness is measured by the geometric index

$$\Gamma = \cos(\Delta\psi_n) \times (\Sigma_1 \Sigma_2)^{1/2},$$

which captures both phase alignment and internal order. When Γ is high (above ~ 3), the Coulomb barrier effectively softens and fusion proceeds more easily even at modest kinetic energies.

How it Was Determined:

Γ is constructed from the mean curvature phase ψ_n and the coherence index Σ , both computed directly from 4-D rotor configurations. The

cosine term rewards phase alignment ($\Delta\psi_n \rightarrow 0$), while the Σ term weights the internal smoothness and order of each nucleus.

Result 3: D–T fusion succeeds due to nearly perfect phase continuity.

D–T fusion is exceptionally facile because deuterium ($\psi_{\text{D}} \approx 38^\circ$) and tritium ($\psi_{\text{T}} \approx 42^\circ$) differ by only $\Delta\psi_n \approx 4^\circ$, producing $\Gamma \approx 3.0$, the highest in the Atlas. In contrast, D–D fusion is inhibited because their matching curvature lobes interfere destructively, generating a high-shear equatorial belt.

How it Was Determined:

Atlas visualizations show that D–T has a nearly seamless interface with near-zero shear, consistent with its large empirical cross-section. The D–D case, despite identical charge, generates an interference pattern that bifurcates the fusion channel, explaining its lower cross-section.

Result 4: Phase-catalyzed fusion can reduce barriers without added heat.

Small external perturbations that shift a nucleus’s curvature phase by only a few degrees ($\delta\psi_n$) can significantly increase Γ , sharply lowering the geometric barrier. This suggests fusion may be enhanced “warmly” by rotating, magnetically biasing, or vibrationally exciting fuel rather than heating all of it.

How it Was Determined:

The Atlas shows that many non-fusing isotope pairs exhibit modest mismatches ($\Delta\psi_n \approx 10^\circ\text{--}12^\circ$). Differentiating Γ with respect to $\Delta\psi_n$ shows that a 4° phase reduction can double fusion probability, equivalent to tens of keV of thermal energy.

Result 5: Cluster capture enables knot-to-knot fusion at low energy.

In reactions such as $p-^{11}\text{B}$, localized α -like coherence knots act as transient docking sites. These knot-to-knot channels allow fusion through a small, low-shear corridor rather than requiring complete global merging.

How it Was Determined:

Although $p-^{11}\text{B}$ has a large global mismatch ($\Delta\psi_n \approx 20^\circ$), local knots differ by only $\sim 4^\circ-6^\circ$. This local alignment forms a short-lived fusion bridge, reproducing the known 675 keV resonant energy.

Result 6: Heavy-ion fusion is hindered by geometric phase stiffness.

Heavy-ion fusion (e.g., $^{12}\text{C} + ^{12}\text{C}$) is impeded because their large internal curvature fields are phase-stiff and cannot reorient rapidly enough during collision. This stiff resistance (κ_p) produces a persistent high-shear belt, preventing geometric merging even after overcoming the Coulomb barrier.

How it Was Determined:

The Atlas quantifies stiffness κ_p as the reorientation energy cost. κ_p rises quickly with nuclear size due to steep ψ_n gradients, and the geometric cost can exceed the Coulomb barrier for heavy systems, making symmetric collisions topologically inert.

Result 7: Fusion viability is restricted to the Flexible Band of isotopes.

Fusion is geometrically feasible only for light isotopes in the Flexible Band ($Z \leq 20$), which have shallow phase gradients and rapid self-correction rates. Heavier isotopes in the Stiff Plateau ($Z \geq 40$) have surfaces too rigid to adjust curvature during collision, making symmetric heavy-ion fusion unlikely.

How it Was Determined:

The Atlas generates a stiffness map color-coding $\partial\psi_n/\partial r$ across isotopes.

The Stiff Plateau corresponds to maximal phase winding (ψ_n near 60° and 80°), marking the geometric endpoint of stellar nucleosynthesis pathways.

Result 8: Asymmetric collisions mitigate geometric stiffness.

Asymmetric collisions (light nucleus + heavy nucleus) bypass stiffness limitations, enabling fusion where symmetric collisions fail. The small, flexible nucleus deforms and “rolls” its curvature field smoothly over the heavier partner.

How it Was Determined:

Atlas visualizations show that asymmetry localizes and disperses interface shear rather than letting it become a rigid global barrier. The lighter rotor bends to match the heavier nucleus’s local phase ridge, providing a geometric basis for α -capture and similar reactions.

Improvements for Magnetic Confinement Fusion

[R47: Possible Improvements for Magnetic Confinement Fusion](#)

Summary of the Abstract:

Magnetic confinement fusion is re-examined under a framework in which nuclei are treated as structured four-dimensional rotors rather than isotropic point charges. In this view, the fusion barrier acquires a small but orientation-dependent correction that slightly favors coaxial nuclear alignment. Although this geometric term is only a tiny fraction

of the Coulomb barrier, its effect is exponentially amplified through quantum tunneling, leading to potentially measurable changes in fusion reactivity. Magnetized plasmas naturally possess helicity, spin polarization, and torsional energy that can bias nuclear orientations during collisions. The paper derives the resulting correction to the reaction rate and proposes three concrete, falsifiable experiments involving helicity control, spin-polarized fuel, and alpha-channeling. If confirmed, these effects would establish geometric alignment as a new optimization axis for fusion reactors, enabling meaningful gains in performance without increased temperature or density.

Result 1: Fusion rates in Magnetic Confinement Fusion (MCF) depend on the geometric orientation of internal nuclear rotation planes, not solely on temperature.

Nucleons are modeled as structured four-dimensional rotors whose internal alignment (θ_{eff} , $\Delta\phi_4$) creates a small orientation-dependent correction (ΔV_{rot}) to the Coulomb barrier. Although this correction is tiny ($\Delta V_{\text{rot}} / V_C \approx 10^{-3}$ – 10^{-2}), the exponential sensitivity of quantum tunneling amplifies it into measurable changes in reactivity, potentially doubling or tripling the tunneling probability for favorable coaxial alignment ($\theta_{\text{rel}} \approx 0^\circ$).

How it Was Determined:

The result follows from a theoretical framework (R30–R46) treating nucleons as 4-D rotors with intersecting mass–charge planes. The orientation-dependent contribution is $\Delta V_{\text{rot}} \propto -V_0 (r_0 / r)^3 \cos^2\theta_{\text{rel}}$, which favors coaxial alignment.

Result 2: The fusion cross-section ($\langle\sigma v\rangle$) can be enhanced by tens of percent by controlling plasma helicity or fuel spin polarization.

Plasma helicity (h) and spin polarization (p) bias the distribution of nuclear orientations, producing measurable non-thermal yield

enhancement. Even modest values ($p \approx 0.1$ or $h \approx 0.1$) increase reaction rates by tens of percent at sub-100 keV, comparable to several keV of effective temperature increase.

How it Was Determined:

The effective reaction rate $\langle \sigma v \rangle$ is computed by integrating the orientation-dependent tunneling probability $P(E, \theta_{\text{rel}})$ over the non-isotropic distribution $f(E, \theta_{\text{rel}})$. The first-order correction is $\Delta \langle \sigma v \rangle / \langle \sigma v \rangle_0 \approx \frac{1}{2} \xi (p + h \tan \alpha)$, where ξ measures tunneling amplification sensitivity.

Result 3: Helicity-programmed magnetic perturbations are predicted to produce a sign-reversing fusion-yield asymmetry ($\Delta Y / Y$).

Applying a phase-locked magnetic perturbation with a chosen helicity (e.g., $m = 2, n = 1$) slightly shifts the mean nuclear orientation, altering the yield. Alternating between right- and left-handed field twists on successive discharges is predicted to reverse the sign of the resulting yield difference ($\Delta Y / Y \approx 1\text{--}5\%$), providing a self-calibrating test.

How it Was Determined:

The experiment uses 3-D field coils (RMP) to apply slow, single-helicity waveforms. The hallmark signal is a helicity-odd yield difference $\Delta Y / Y \propto h$ that must reverse sign when h is reversed, clearly distinguishing it from thermal or density variations.

Result 4: Using spin-polarized deuterium or $D\text{--}^3\text{He}$ fuel is predicted to increase fusion output for aligned spins compared to anti-aligned spins.

If the internal nuclear rotation plane (θ_{eff}) couples to nuclear spin, polarized fuel should exhibit distinct cross-sections for parallel ($\sigma \uparrow \uparrow$) versus anti-parallel ($\sigma \uparrow \downarrow$) spin alignments. This alignment effect is predicted to increase total yield by $\Delta Y / Y \approx \frac{1}{2} \xi p \approx 1\text{--}10\%$, depending

on the polarization fraction p .

How it Was Determined:

The method uses partially polarized fuel ($p \approx 0.2-0.5$) while alternating alignment relative to the magnetic field B . The model is falsified if aligned, anti-aligned, and unpolarized conditions produce indistinguishable yields at constant temperature.

Result 5: Alpha-channeling is reinterpreted as extraction of torsional curvature energy from the fused rotor, with efficiency predicted to depend on wave helicity.

In this geometric interpretation, alpha-channeling transfers the torsional component of the fused nucleus back into the electromagnetic field rotation. Maximizing this exchange requires matching helicity between the applied RF waves and the fused rotor, predicting that one helicity should yield stronger current drive and lower alpha-loss than the opposite.

How it Was Determined:

The test uses ICRF or EBW waves tuned to alpha gyro-orbits, alternating wave helicity. Observation of asymmetric current drive and α -loss between right- and left-handed modes confirms resonant torsion extraction.

Result 6: A null result would still be scientifically valuable because it would sharply constrain the magnitude of the nuclear geometric correction.

If experiments produce no measurable helicity-odd or spin-dependent effects beyond statistical uncertainty ($\pm 1\%$), then $\Delta V_{\text{rot}} / V_C$ must be $< 10^{-3}$, implying an extremely isotropic tunneling barrier and greatly tightening bounds on 4-D nuclear orientation effects.

How it Was Determined:

Modern neutron diagnostics ($\pm 1\%$) define the detection threshold. A

valid null result must be accompanied by control cases confirming no sign reversal when helicity is inverted and no spurious correlation with plasma temperature or density.

Improvements for Inertial-Confinement Fusion (ICF)

R48: Possible Improvements for Inertial-Confinement Fusion (ICF)

Summary of the Abstract:

Inertial-confinement fusion is reconsidered under a geometric framework in which nuclei are treated as structured four-dimensional rotors rather than isotropic point charges. In this view, the Coulomb barrier acquires a small orientation-dependent correction that favors parallel alignment of internal mass–charge planes during the brief bang-time interval. Although the correction is only a tiny fraction of the barrier height, its exponential amplification through tunneling can produce measurable changes in fusion yield at fixed temperature and areal density. The paper proposes that shock phasing, weak seed magnetic fields, and short circularly polarized THz pulses can bias nuclear orientation during stagnation. Three concrete, reversible experiments are outlined that predict yield asymmetries reversing with helicity or phase while leaving hydrodynamic compression unchanged. Confirmation would establish bang-time geometric alignment as a new optimization variable in inertial fusion, while a null result would tightly constrain any orientation-dependent component of the nuclear barrier.

Result 1: Fusion yield depends on the geometric orientation of nuclear rotation planes, providing a new axis for ICF optimization.

If nuclei are 4-D rotors, the Coulomb barrier contains a small orientation-dependent term $\Delta V_{\text{rot}} \propto \cos^2\theta_{\text{rel}}$. Due to the exponential dependence of tunneling on barrier height, this term can increase fusion yield by several percent at constant temperature (T) and areal density (ρR). This change is measurable with modern diagnostics, establishing “bang-time plane control” as a new optimization variable alongside compression and temperature.

How it Was Determined:

The prediction originates from earlier theoretical work (R30–R47) showing that a geometric correction ΔV_{rot} modifies tunneling according to $P(E, \theta_{\text{rel}}) \propto P_0(E) \exp[\xi \cos^2\theta_{\text{rel}}]$. The exponent ξ is estimated to be 0.02–0.05 at typical hot-spot conditions, implying that a 5% alignment bias produces a 1–3% enhancement in $\langle\sigma v\rangle$.

Result 2: Shock-phase control should produce a sign-reversing yield asymmetry proportional to helicity inversion.

A timing offset of ± 25 – 50 ps between converging shocks alters the transient helicity (h) of the imploding plasma, biasing nuclear orientation without changing total laser energy. This should produce a reproducible yield difference $\Delta Y / Y \approx 1$ – 3% , which reverses sign when the shock-phase timing is inverted.

How it Was Determined:

Implosion shocks impose rotational phase relationships that influence plasma helicity. The effect is helicity-odd, meaning the yield difference must reverse sign when the timing asymmetry reverses. Experimental validation requires back-to-back shots with opposite timing offsets while holding ρR and T_i constant.

Result 3: Helical seed-field inversion should generate a yield asymmetry linked to nuclear alignment.

A weak pre-imposed magnetic field introduces a preferred rotation axis and finite helicity into the imploding fuel. Alternating the field polarity between shots is predicted to produce yield differences $\Delta Y / Y \approx 2\text{--}5\%$ due to nuclear alignment, independent of implosion symmetry.

How it Was Determined:

The seed field aligns charge-rotation planes, generating an alignment fraction $p \approx \mu B / (kT) \approx 10^{-3}\text{--}10^{-2}$. The model predicts that fusion yield increases with matching helicity; thus, the signature is a yield difference that changes sign upon reversing the magnetic-field polarity.

Result 4: A circularly polarized THz pulse applied near bang time can achieve transient phase synchronization.

A circularly polarized THz pulse (0.3–3 THz) applied during peak compression can couple directly to the nuclear torsional phase ($\Delta\phi_4$), briefly synchronizing nuclear rotation planes. Alternating THz helicity is predicted to produce a 2–5% variation in neutron yield, confirming geometric-phase participation in tunneling.

How it Was Determined:

The rotating electromagnetic field couples to the internal curvature rotation. The experiment requires synchronizing the THz pulse with bang time and comparing yields for right- versus left-circular polarization.

Chapter 3 – Quantum Computing — at Room Temperature

The Nuclear Rotor Atlas framework provides a geometric foundation for achieving room-temperature quantum computing by redefining coherence. Geometry, specifically curvature continuity, rather than refrigeration, becomes the sustaining mechanism for coherent computation.

Electron and Nuclear Qubit Stability

[R78: The Nuclear Rotor Atlas: Insights on Electron and Nuclear Qubit Stability](#)

Summary of the Abstract:

Quantum coherence is reframed as a geometric phenomenon rather than a thermodynamic one, with qubits modeled as four-dimensional curvature rotors whose phase ψ resides on S^3 . Coherence persists when the stability ratio $\Lambda = \Sigma S_{\max}$ exceeds a universal threshold of 16, where

The Nuclear Rotor Atlas Handbook

Σ measures mean curvature alignment and S_{\max} the maximum local shear. Temperature increases shear but does not destroy coherence if curvature stiffness κ is sufficiently high to keep Λ above this boundary. Analysis of Nuclear Rotor Atlas data shows that several known qubit platforms already satisfy this condition at room temperature, including diamond NV centers, isotopically pure silicon, and topological surface states. Electron qubits are therefore geometrically capable of warm operation, while nuclear qubits, with vastly higher κ , represent the extreme limit of long-term coherence and stability. Hybrid systems coupling fast electron logic to nuclear curvature anchors are predicted to enable scalable, non-cryogenic quantum architectures governed by a single law of curvature continuity.

Result 1: Coherence is a Geometric, Not a Thermodynamic, Phenomenon.

Quantum coherence is defined as the continuous orientation of a four-dimensional (4-D) curvature field's internal phase (ψ) on the hypersphere S^3 . Temperature is secondary, as it merely increases the local rate of phase distortion (shear S) rather than being the fundamental cause of coherence loss.

How it Was Determined:

The Nuclear Rotor Atlas models each qubit as a 4-D curvature rotor, showing that decoherence is a geometric discontinuity resulting from localized bending or twisting of ψ . Quantitative analysis confirmed that coherence persists if the material's curvature stiffness (κ) is high enough to resist shear S caused by thermal vibrations.

Result 2: Universal Coherence Stability is Defined by the Ratio $\Lambda > 16$.

The persistence of coherence is governed by the universal stability ratio $\Lambda = \Sigma / S_{\max}$, where Σ is the mean curvature alignment and S_{\max} is

the maximum local curvature shear. Coherence persists when Λ exceeds sixteen, the threshold at which localized curvature gradients overcome global phase continuity.

How it Was Determined:

This criterion was derived from extensive mapping across thousands of isotopes in the Nuclear Rotor Atlas, demonstrating that it applies universally to both electronic and nuclear curvature fields. When Λ falls below 16, the curvature fractures, leading the system to transition into decoherent behavior.

Result 3: Electron Qubits Possess Geometric Capacity for Room-Temperature Operation.

Electronic qubits (NV centers in diamond, donor electrons in purified silicon) have moderate curvature stiffness ($\kappa \approx 10^9\text{--}10^{11} \text{ J} \cdot \text{m}^{-3}$) yet maintain $\Lambda \approx 20\text{--}30$ at 300 K. Their coherence is attributed to geometric homogeneity: high lattice perfection and symmetry enhance κ and reduce shear S .

How it Was Determined:

The geometric model predicts that the coherence lifetime τ scales as $\tau \propto (\kappa\Sigma) / T$. Using known parameters for diamond and silicon yields predicted maximum temperatures consistent with observed millisecond coherence times at ambient conditions (e.g., $T_{\text{max}} \approx 340 \text{ K}$ for diamond).

Result 4: Nuclear Qubits Offer Extreme Long-Term Stability as Memory Anchors.

Nuclear ψ_n fields exist at the extreme limit of curvature stability, possessing enormous stiffness ($\kappa \approx 10^{14}\text{--}10^{16} \text{ J} \cdot \text{m}^{-3}$) that grants near-absolute immunity to external gradients. Their Λ ratio often exceeds 100, making them ideal for long-lived quantum memory with coherence times of seconds to minutes.

How it Was Determined:

The immense κ ensures that thermal agitation cannot introduce measurable shear S , so coherence is governed primarily by weak residual interactions. The trade-off is speed: their ψ_n phase is nearly immovable, restricting gate operations to the MHz scale and making them unsuitable for fast logic.

Result 5: Hybrid ψ_e - ψ_n Systems Combine Speed and Endurance.

Scalable quantum processors are predicted to be hybrid systems where rapid electronic phase (ψ_e) performs logic operations and the immovable nuclear phase (ψ_n) anchors stability. This requires a shared curvature corridor (S_{corridor}) where the coupled stability parameter $\Lambda_{e-n} = (\Sigma_e \Sigma_n) / S_{\text{corridor}}$ remains high.

How it Was Determined:

The Atlas treats these as dual-rotor geometries, showing that when Λ_{e-n} is high, the composite coherence exceeds the lifetime of the electron qubit alone. Simulations show that when Λ_{e-n} exceeds 50, phase errors are extremely low even at 300 K, mimicking nature’s pattern of linking speed to endurance.

Result 6: Geometric Order is the Key Design Parameter for Warm Quantum Technology.

The geometric model provides a quantitative screening tool for identifying qubit hosts, predicting thermal robustness scales directly with curvature stiffness κ and coherence alignment Σ . The requirement for room-temperature coherence is $\kappa > 3 \times 10^{10} \text{ J} \cdot \text{m}^{-3}$, favoring high- κ dielectrics, diamond, or silicon carbide.

How it Was Determined:

Plotting Λ as a function of κ and T reveals a “warm-coherence window,” showing that Λ remains above 16 at 300 K only when κ exceeds the threshold. This explains why improvements in lattice

stiffness or isotopic purity yield predictable gains in coherence time τ without refrigeration.

Result 7: Decoherence is Geometric Relaxation, Not Thermodynamic Collapse.

Decoherence is reinterpreted as geometric relaxation: environmental noise increases local curvature shear S , lowering Λ below threshold. This explains why coherence decays exponentially, mirroring stress relaxation in a curved medium.

How it Was Determined:

In the Atlas model, noise imposes angular misalignments on ψ . When these accumulate faster than the material's stiffness κ can correct them, Λ falls and coherence decays. Exponential decay thus arises directly from κ and S_{max} , clarifying why purity and lattice order always improve coherence.

Result 8: Topological Protection is a Subset of Curvature Coherence.

Topological quantum computing is interpreted as a special case of curvature coherence, where robustness arises because ψ continuity extends over closed 4-D paths on S^3 . Topological protection emerges when Λ is preserved by system topology rather than solely by local stiffness κ .

How it Was Determined:

Information stored in non-local geometric quantities (such as Berry curvature) is resistant to local disturbances because phase errors require global curvature distortions. This connects topological qubits and curvature rotors by showing that topological order is a distributed form of curvature stiffness.

Geometry of Quantum Computing

R76: The Nuclear Rotor Atlas — Geometry of Quantum Computing

Summary of the Abstract:

Quantum coherence is presented as a geometric property of curvature on S^3 rather than a fragile probabilistic feature of isolated wavefunctions. In this framework, the phase ψ represents the orientation of a four-dimensional curvature field whose stability is governed by curvature stiffness κ and coherence Σ . Quantum computation is recast as the maintenance and controlled rotation of curvature continuity, with qubits realized as stable curvature knots and entanglement arising from ψ -aligned domains. Logical operations correspond to holonomic rotations of ψ through well-defined geometric paths, making gates intrinsically robust against noise and timing errors. Because coherence is protected by geometric stiffness rather than thermal isolation, curvature-based qubits are predicted to operate in warm or condensed-phase environments without cryogenics. Examples drawn from nuclear, electronic, and hybrid systems suggest practical routes toward scalable, energy-efficient quantum computers based on geometry rather than extreme refrigeration.

Result 1: Quantum Coherence is a Geometric Property of Curvature Phase (ψ).

Coherence is redefined as the rotational orientation of a four-dimensional (4-D) curvature field embedded in S^3 , not an abstract probabilistic superposition. A system is coherent when its curvature

phase (ψ) is spatially continuous and uniform.

How it Was Determined:

The Nuclear Rotor Atlas models nuclear matter as a 4-D curvature field, demonstrating that the wavefunction phase (ψ) corresponds to the orientation of curvature in 4-space. Decoherence arises when spatial gradients of ψ develop, creating shear $S = |\nabla\psi|$.

Result 2: Stability is Determined by the Universal Coherence-to-Stress Ratio (Λ).

The stability of all curvature-based systems is governed by the geometric ratio $\Lambda = \Sigma / S_{\text{max}}$, where Σ is the mean coherence index and S_{max} is the maximum local shear. Coherence persists only when $\Lambda > 16$; below this threshold ($\Lambda \leq 16$), the manifold bifurcates and decoherence follows.

How it Was Determined:

This threshold ($\Lambda > 16$) was first observed in the Atlas's nuclear data for fission stability, but it is asserted to apply universally for electronic and condensed-matter systems. This ratio establishes stability as a geometric continuity condition rather than a statistical correlation.

Result 3: A Qubit is a Topologically Protected Curvature Knot.

A qubit is defined as a localized, controllable knot of curvature phase, a 4-D vortex where ψ rotates through 2π while maintaining coherence ($\Sigma \approx 1$). Its logical states $|0\rangle$ and $|1\rangle$ correspond to opposite chiralities of this knot (clockwise vs counterclockwise ψ orientation).

How it Was Determined:

The winding number n of the knot is quantized as $n = (1 / 2\pi) \oint \nabla\psi \cdot dl$, where $n = \pm 1$ yields the two logical states. Because the state is determined by a quantized winding number, small disturbances cannot change the logical state without breaking ψ continuity, providing intrinsic topological protection.

Result 4: Entanglement is the Spatial Continuity of Curvature Phase.

Entanglement is redefined as the physical continuity of curvature phase (ψ) across spatially separated domains, resolving the mystery of nonlocality. Two regions remain entangled as long as the curvature corridor linking them remains intact and ψ is continuous.

How it Was Determined:

The continuity condition requires $\nabla\psi = 0$ along the corridor C linking qubits A and B. Decoherence occurs deterministically when local shear in the corridor rises such that the coherence integral Γ_{AB} drops below unity, which typically arises when $\Lambda < 16$.

Result 5: Curvature Stiffness (κ) Enables Warm and Condensed-Phase Coherence.

Curvature stiffness (κ) measures how strongly the curvature field resists deformation of ψ ; high- κ materials suppress shear S and allow long-lived coherence even under thermal agitation. The coherence lifetime τ_{coh} scales approximately as $\tau_{\text{coh}} \propto M_{\psi} / T \propto (\kappa\Sigma) / T$.

How it Was Determined:

High- κ materials (e.g., isotopically pure crystals with $\kappa \approx 10^9\text{--}10^{11} \text{ J} \cdot \text{m}^{-3}$) prevent environmental gradients from increasing shear S enough to reduce Λ below 16. This geometric protection overturns the usual requirement for cryogenic isolation, suggesting room-temperature operation is possible.

Result 6: Quantum Logic Operations are Holonomic Rotations of ψ .

Logical operations are realized as smooth, adiabatic rotations of the curvature knot's ψ orientation on S^3 . These holonomic gates accumulate

a geometric phase (Φ) dependent only on the geometry of the path $\Omega(\Gamma)$, not the timing or speed of traversal.

How it Was Determined:

When ψ traces a closed trajectory Γ , the resulting phase depends solely on the solid angle $\Omega(\Gamma)$ subtended by the trajectory. Because the outcome depends only on the shape of the path, such logic gates are inherently immune to noise that perturbs timing but restores the endpoints, providing built-in fault tolerance.

Result 7: Measurement is the Topological Collapse of Curvature Continuity.

Wavefunction collapse is reinterpreted as the topological severing of curvature continuity when a qubit couples strongly to the apparatus. The detector's macroscopic curvature field locally fixes ψ orientation, causing the corridor linking entangled partners to fail ($\Lambda < 16$).

How it Was Determined:

Observation forces the qubit's ψ to align with the detector's geometry, collapsing the shared ψ continuity along the connection corridor. This is a topological splitting of the global curvature field into disconnected domains, altering ψ connectivity rather than invoking probabilistic collapse.

Result 8: Hybrid Systems Leverage Nuclear Coherence as Stable Memory Anchors.

The nuclear curvature phase (ψ_n) acts as a stable geometric reference capable of seeding and anchoring coherence in the surrounding electron cloud (ψ_e). Hybrid qubits such as ^9Be donors in isotopically pure hosts use high nuclear stiffness (κ_n) to stabilize electronic memory.

How it Was Determined:

The Atlas shows that nuclear ψ_n coherence modulates boundary conditions for electronic orbitals, producing measurable phase

correlations. Leveraging the long-lived stability of nuclear rotors ($\Lambda \gg 16$), these hybrid systems are predicted to achieve millisecond- to second-scale qubit lifetimes.

Room Temperature Quantum Computing

[R77-ESSAY — Electrons First, Nuclei Forever: What the Nuclear Rotor Atlas Reveals About Room-Temperature Quantum Computing](#)

Summary:

This essay argues that *The Nuclear Rotor Atlas* provides the geometric framework needed to understand how quantum coherence can persist—and therefore how quantum computing can operate—at room temperature. The Atlas reveals that coherence is determined by curvature continuity, not by temperature, through the stability ratio $\Lambda = \Sigma S_{\max}$. Electrons, with flexible curvature and high responsiveness, are poised to win the first generation of warm quantum computing by virtue of their speed, ease of control, and compatibility with existing semiconductor methods. Nuclei, with immense curvature stiffness κ and nearly perfect phase alignment, will eventually dominate as ultra-stable anchors for long-term quantum memory and large-scale coherence. Both obey the same geometric law, differing only in scale. Their partnership—fast ψ_e logic stabilized by steady ψ_n anchors—defines a roadmap toward practical, self-correcting quantum processors that function without cryogenics. The essay concludes that geometry itself, not refrigeration, will sustain the future of coherent computation.

Result 1: Coherence is Geometric, Not Thermodynamic.

The stability of a quantum system stems from geometry: how smoothly curvature aligns across the hidden four-dimensional surface S^3 underlying matter. If the material's internal curvature stiffness (κ) is large enough, coherence persists at any temperature, provided the curvature phase (ψ) remains continuous.

How it Was Determined:

The Atlas, which geometrically maps all known nuclei, shows that curvature continuity—quantified by the stability ratio $\Lambda = \Sigma / S_{\text{max}}$ —is the true determinant of stability. Heat merely attempts to introduce small shear gradients (S) in ψ ; if κ is sufficiently high, these gradients remain tiny and Λ stays well above threshold.

Result 2: The Universal Stability Condition (Λ).

Stability is governed by the ratio $\Lambda = \Sigma / S_{\text{max}}$, where Σ is the mean coherence index and S_{max} is the maximum local curvature shear. Coherence persists only when Λ exceeds roughly sixteen; below this, the curvature field buckles and decoherence begins.

How it Was Determined:

All stable structures are modeled as 4-D curvature rotors whose state is described by a continuous phase ψ winding over S^3 . Since Λ is geometric rather than thermodynamic, materials with high curvature stiffness κ can maintain $\Lambda > 16$ even when thermal noise increases shear S .

Result 3: Electrons are the Fast, Responsive Qubits (First Generation).

Electrons are the most agile carriers of curvature coherence, making them ideal active qubits with intrinsic gate speeds in the GHz–THz

range. Their flexible curvature phase ψ_e responds quickly to external control, but this same mobility makes them vulnerable to environmental gradients and shear.

How it Was Determined:

The electron's ψ_e phase rotates rapidly on S^3 , supporting fast logic operations compatible with semiconductor technologies. The Atlas indicates that electron fragility is not intrinsic but environmental: a geometrically stiff, phase-aligned host (high κ , small S) can preserve electron coherence at room temperature.

Result 4: Nuclei are the Slow, Stable Qubits (Long-Term Memory).

Nuclei act as long-term quantum memory because their immense curvature stiffness κ (up to $\sim 10^{15} \text{ J}\cdot\text{m}^{-3}$ or higher) prevents external noise from generating meaningful curvature shear. As a result, nuclear coherence ψ_n can persist for seconds, minutes, or hours, with Λ often exceeding one hundred.

How it Was Determined:

The Atlas shows that nuclear κ is extremely large, making thermal and magnetic disturbances almost irrelevant. Nuclear phases shift slowly, establishing the nucleus not merely as mass but as a phase anchor around which the local curvature geometry stabilizes.

Result 5: Hybrid Systems are the Foundation of Practical Architecture.

Practical quantum processors will be hybrid systems in which the nucleus provides geometric stability and the electron provides responsiveness for logic. This requires the electron phase ψ_e and nuclear phase ψ_n to join across a continuous curvature corridor where the stability ratio Λ remains high throughout.

How it Was Determined:

High nuclear κ forms a stable phase basin, while the lower κ electronic

domain provides controllability within that basin. Their shared coherence corridor keeps ψ continuous across the boundary, granting the electron–nucleus composite both speed and long-term endurance.

Result 6: Electrons and Nuclei Share a Single Geometric Law.

Electrons and nuclei obey the same geometric stability condition $\Lambda = \Sigma / S_{\max} > 16$. They are not separate kinds of matter but distinct points on the same curvature-stiffness spectrum, differing only by the scale of κ .

How it Was Determined:

Atlas data shows that plots of curvature stiffness versus shear produce a smooth continuum, demonstrating that ψ_e transitions seamlessly into ψ_n through graded variations in κ . This unifies the apparent contradiction between fragile electron coherence and near-eternal nuclear coherence: both reflect the same geometric rule applied at different stiffness scales.

Chapter 4 – Halfway to Superconductivity

Not zero resistance at room temperature, but greatly reduced resistance.

Toward Room-Temperature Low-Resistance Conduction

[R33-S9: Toward Room-Temperature Low-Resistance Conduction via \$\psi\$ -Phase Locking](#)

Summary of the Abstract:

The work proposes a geometrically grounded pathway to near-frictionless electrical conduction at ambient temperature based on partial phase coherence of the electron on S^3 . Within the Hopf-linked electron framework, resistance vanishes only when both internal phases lock, but a distinct ψ -locked metallic state emerges when current-phase coherence alone is established. This regime is governed by a single,

falsifiable inequality, $A \rho_s / k_B T \gtrsim 1$, linking low-resistance transport to measurable superfluid stiffness, temperature, and a geometric coupling factor. When the criterion is met, resistivity is predicted to fall exponentially while magnetic properties remain essentially unchanged, distinguishing ψ -lock conduction from superconductivity. The paper outlines concrete materials-engineering strategies—strain, carrier-density tuning, texture alignment, purity, and transient THz or Floquet driving—to raise ρ_s and A toward the ψ -lock threshold at room temperature. Together these elements define a testable design roadmap for creating coherent, low-loss metals that bridge ordinary conductors and superconductors without requiring cryogenic operation.

Result 1: A distinct, low-resistance ψ -locked metallic state is predicted to occur when only the electron’s current phase (ψ) becomes coherent at ambient temperature.

This state exhibits exponentially reduced resistivity and strong low-frequency conductivity enhancement, yet it retains finite resistance and negligible diamagnetism, distinguishing it from full superconductivity. It occurs when the current-phase stiffness dominates thermal agitation, linking electronic topology to practical energy efficiency.

How it Was Determined:

The condition for ψ -lock was derived from the geometric energy balance of the Hopf-linked electron model, requiring that the stiffness energy per carrier ($A\rho_s$) exceeds the thermal disorder ($k_B T$). This balance is expressed as the single, measurable inequality: $A\rho_s / (k_B T) \gtrsim 1$.

Result 2: Room-temperature ψ -lock conduction is achievable by boosting the ψ -lock index (S_ψ) by a factor of 5–6 through combined, modest material optimizations.

Since $S_\psi \propto A(n/m^*)$, this is accomplished by leveraging small,

achievable increases in carrier density (n), decreases in effective mass (m^*), and improvements in structural factors (A and purity). This converts electronic topology from a descriptive concept into a design variable, defining a practical path toward ambient low-resistance flow.

How it Was Determined:

The design pathway quantified the multiplicative dependence of S_{ψ} on four independent parameters (n , m^* , A , and purity). The analysis showed that a 10–30% increase in each factor collectively yields a 5–6 \times total gain, sufficient to cross the $S_{\psi} \geq 1$ threshold at 300 K for high-mobility systems.

Result 3: Resistivity in the ψ -locked regime follows a characteristic exponential suppression law that serves as the primary experimental diagnostic.

Resistivity decreases according to $\rho(T) = \rho_0 \exp[-\eta A \rho_s(T) / (k_B T)]$, where η is a universal geometric factor. Plotting $\ln \rho$ versus ρ_s / T must yield a straight line with a constant slope over at least one decade in resistivity to confirm ψ -lock scaling.

How it Was Determined:

This law was derived from the geometric free-energy density governing ψ -phase coherence when the orbital phase (ϕ) is disordered. Absence of this exponential behavior or a strongly varying slope is defined as a falsifier for the model.

Result 4: Transient ψ -lock can be induced reversibly using external THz or Floquet drives, providing an ideal diagnostic that eliminates structural complications.

A sufficiently strong, resonant external oscillating field (e.g., 0.3–3 THz) transiently modifies the effective stiffness (ρ_s') and coupling (A'), producing a momentary exponential drop in resistivity. This transient effect must cease immediately when the drive ends, distinguishing it

from structural changes.

How it Was Determined:

The stiffness modification is quantified by the relation

$$\rho_s' = \rho_s [1 + \langle v_F E_0 \rangle^2 / (\hbar \omega_d)^2],$$

where E_0 is the field amplitude. Confirmation requires monitoring resistivity: a reversible fall by 10–50% within the pulse envelope, accompanied by no change in static magnetic susceptibility, verifies ψ -only phase stiffening.

Result 5: ψ -lock is decisively falsifiable by the predicted absence of Meissner screening and the lack of a heat-capacity jump.

Because ψ -coherence aligns current but not orbital motion, magnetic flux penetrates freely, requiring magnetic susceptibility ($\Delta\chi$) to remain virtually unchanged. Furthermore, the onset of ψ -lock must be smooth, showing no latent heat or discontinuity in heat capacity.

How it Was Determined:

The magnetic neutrality criterion is a verification test requiring $|\Delta\chi| < 10^{-5}$. Failure of this test (appearance of flux exclusion or a sharp heat-capacity jump) implies the formation of orbital pairing (ϕ -lock), falsifying the ψ -only hypothesis.

Result 6: The hydrodynamic transport regime, characterized by collective electron flow, is a defining macroscopic signature of ψ -coherence.

ψ -locked conduction results in laminar flow where the mean free path (ℓ) exceeds the channel width, leading to phenomena like negative local resistance and parabolic velocity profiles. This behavior is required to weaken as the temperature rises and S_ψ drops toward unity.

How it Was Determined:

The hydrodynamic regime is characterized by the electronic Reynolds

The Nuclear Rotor Atlas Handbook

number $Re_e \gg 1$. Verification requires measuring nonlocal transport in micron-scale channels and observing a voltage profile consistent with viscous rather than diffusive flow.

Chapter 5 – Superfluidity

High-Temperature Superfluidity

[R41: Criteria for High-Temperature Superfluidity — Platforms, Constraints, and Near-Term Tests](#)

Summary of the Abstract:

High-temperature superfluidity is recast as a geometric phenomenon governed by phase stiffness rather than an intrinsic dependence on low temperature. In the four-dimensional rotor framework, frictionless flow emerges when the ratio of phase stiffness ρ_s to thermal disorder $k^B T$ is large and when phase-locking energy dominates local disorder. Two quantitative inequalities define this condition and provide explicit, testable design targets applicable across disparate physical systems. Applying these criteria shows that room-temperature coherence is already realized in quasiparticle platforms such as exciton–polaritons and magnon spin currents, while condensed-matter and hydrogen-bonded systems approach feasibility near liquid-nitrogen temperatures. Superfluidity, superconductivity, and spin coherence are unified under a single geometric-phase law $V = V_0 \cos \Delta\phi_4$ that links macroscopic

order to four-space phase alignment. In this view, superfluidity is no longer a cryogenic anomaly but a broadly attainable state of ordered rotation that can be engineered through stiffness, coupling strength, and disorder control.

Result 1: High-temperature superfluidity is governed by a geometric criterion based on phase stiffness (ρ_s) relative to thermal disorder ($k_B T$).

Superfluidity is possible at any temperature when the phase stiffness ρ_s significantly exceeds thermal energy $k_B T$, expressed as the thermal-stiffness inequality $\rho_s \gg k_B T$. This geometric view unifies superfluidity, superconductivity, and spin coherence as manifestations of a single geometric-phase law $V = V_0 \cos \Delta\phi_4$.

How it Was Determined:

The stiffness criteria were derived from the full free-energy density functional (Equation 2.4), requiring that the elastic energy of phase twists dominates disorder. This condition dictates that the onset of superfluidity occurs when thermal fluctuations can no longer unbind phase defects, leading to the Kosterlitz–Thouless relation $k_B T_{KT} = (\pi/2) \rho_s$ in 2D systems.

Result 2: The maximum operating temperature (T_{op}) is also constrained by the phase-locking energy exceeding structural disorder (U_{dis}).

Coherence requires a second inequality: the geometric phase-locking energy $V_0 \langle \cos \Delta\phi_4 \rangle$ must exceed the local disorder potential U_{dis} . The phase stiffness ρ_s itself is defined as $\rho_s \approx n\hbar^2/m^*$, meaning lighter mass (m^*) or higher density (n) enables higher T_{op} .

How it Was Determined:

This constraint was derived from minimizing the free-energy density, ensuring that the phase-locking term dominates the dephasing energy

due to disorder (Equation 2.4). Applying this criterion across diverse systems provides a quantitative boundary separating systems that can support high-temperature superfluidity from those that cannot.

Result 3: Light-mass quasiparticle systems like exciton–polaritons and magnons demonstrably achieve room-temperature (≈ 300 K) phase coherence.

Polaritons satisfy the thermal-stiffness criterion because their effective mass ($m^* \leq 10^{-4} m_e$) is extremely small, resulting in $\rho_s / (k_B T) \approx 10^3$ – 10^5 at 300 K. Magnon spin currents, which have effectively zero mass, are governed by large exchange stiffness, achieving phase-rigid flow even at ambient conditions.

How it Was Determined:

Polariton feasibility was confirmed because the Rabi splitting (50–200 meV) easily exceeds $k_B T \approx 25$ meV at 300 K, satisfying the locking condition. Magnon feasibility was confirmed because their large exchange stiffness (tens of meV) means $\rho_s / (k_B T) \gg 1$ even at 300 K.

Result 4: Atomic liquids are fundamentally excluded from high-temperature superfluidity by their high mass, regardless of phase locking.

For atoms like ^4He or ^3He , the large mass ($m^* \approx 10^{-26}$ kg) results in a stiffness ρ_s that is too small compared to $k_B T$ above a few Kelvin. Equation (3.1) is violated by four to eight orders of magnitude at 77 K and 300 K, respectively, confining atomic superfluids to cryogenic regimes.

How it Was Determined:

The calculation used typical atomic densities (10^{28} m $^{-3}$) and masses, yielding $\rho_s \approx 10^{-25}$ J m $^{-1}$. This small value demonstrated that the mass term dominates, violating the thermal-stiffness inequality.

Result 5: Interlayer excitons and protonic rotor networks sit near the boundary for liquid-nitrogen temperature (≈ 77 K) coherence and are a viable frontier.

Interlayer excitons achieve modest mass ($m^* \approx 0.1-1 m_e$) and strong coupling, placing their expected coherence temperature T_c near 50–100 K. Protonic networks, despite having the mass of a proton, achieve $T_c \approx 90$ K due to high density ($n \approx 10^{28} \text{ m}^{-3}$), making them potentially capable of 77 K operation with refinement.

How it Was Determined:

Numerical evaluation showed that interlayer excitons have $\rho_s / (k_B T) \approx 2-3$ at 77 K, suggesting only modest improvements are needed to cross the threshold. The protonic rotor stiffness ρ_s was calculated using m_p , yielding a predicted $T_c \approx 90$ K.

Result 6: The model provides an explicit set of falsifiable geometric tests, including the dependence of critical parameters on the cosine phase law.

The framework predicts that observable quantities, such as critical velocity (v_c) or supercurrent amplitude (A), must be modulated by the geometric phase φ_4 according to the law $A \propto \cos \Delta\varphi_4$. Failure modes are defined, such as observing linear or random responses to field rotation, which would disprove the geometric hypothesis.

How it Was Determined:

Falsifiability is achieved by deriving measurable consequences for each inequality, such as the prediction that the vortex density n_v should decrease exponentially as ρ_s increases. The measurement checklist requires experimental protocols (e.g., field-controlled phase rotation) to verify the predicted cosine dependence.

Chapter 6 – Fission

Geometry of Fission

[R75: The Nuclear Rotor Atlas: Geometry of Fission](#)

Summary of the Abstract:

The work presents nuclear fission as a four-dimensional geometric phenomenon in which each nucleus is a curvature manifold whose stability depends on the coherence of its internal phase ψ_n relative to curvature shear. Fission occurs when the coherence-to-shear ratio $\Lambda = \Sigma / S_{\max}$ drops below a critical value of roughly 16, triggering a topological bifurcation rather than the crossing of an energy barrier. Using the Nuclear Rotor Atlas of 780 isotopes, the study shows that fragment mass asymmetries, kinetic energies, and neutron emissions follow directly from predictable curvature fracture patterns on S^3 . Symmetric and asymmetric fission emerge as distinct geometric rupture modes, while spontaneous fission appears as gradual curvature fatigue driven by long-term coherence erosion. Prompt neutrons are identified as expelled curvature knots, and delayed neutrons and γ rays arise from post-scission phase relaxation within the fragments. Together these results unify induced, spontaneous, and photonic fission as expressions

of a single geometric mechanism and place fission and fusion as conjugate phases of one continuous curvature cycle.

Result 1: Fission is a Topological Bifurcation, Not an Energetic Barrier Event.

Fission is fundamentally defined as a loss of curvature coherence—a topological bifurcation of the 4-D manifold rather than overcoming a potential energy barrier. This transition occurs when the nucleus loses the smooth curvature connection that binds it into a single geometric entity.

How it Was Determined:

The Atlas maps each nucleus as a four-dimensional curvature domain on the hypersphere S^3 , defined by its coherence field C . The onset of fission is determined by monitoring the coherence-to-shear ratio $\Lambda = \Sigma / S_{\text{max}}$.

Result 2: The Critical Instability Threshold is Geometric ($\Lambda \leq 16$).

The critical condition for fission is reached when the coherence-to-shear ratio (Λ) falls below a critical value, empirically determined to be around 16. Stability is lost when local curvature stress exceeds the restoring elasticity (κ) along a narrow fault belt of maximal shear.

How it Was Determined:

The geometric instability threshold $\Lambda \approx 16$ was derived quantitatively by plotting Λ across isotopes and observing where curvature continuity collapse occurs. This geometric threshold reproduces the observed transition from stable thorium to spontaneously fissioning californium without invoking empirical constants.

Result 3: Asymmetric Mass Splits Arise from Pre-existing Geometry.

Asymmetric mass splits (like in ^{235}U) arise naturally because the parent nucleus already contains two unequally coherent curvature lobes before scission. The heavier fragment retains the central, high-coherence curvature pole (Σ), while the lighter fragment forms from an outer saddle region of lower coherence.

How it Was Determined:

Atlas visualizations showed that uranium and plutonium nuclei already possess unequal curvature lobes with a coherence ratio $\Sigma_1 / \Sigma_2 \approx 1.3$ – 1.4 . Asymmetric fission dominates beyond a nuclear curvature phase $\psi_n \approx 65$ degrees.

Result 4: Spontaneous Fission is Curvature Fatigue.

Spontaneous fission (e.g., in ^{252}Cf) is reinterpreted as a slow, internal fatigue of curvature coherence, where zero-point curvature oscillations gradually erode the connection over time. This process occurs in nuclei where the curvature phase ψ_n exceeds 75 degrees, causing phase stiffness κ to diminish and coherence basins to become barely connected.

How it Was Determined:

The Atlas showed that spontaneous fission half-lives ($t_{1/2}$) scale exponentially with the coherence ratio Λ , following the relation $t_{1/2} \propto \exp(b\Lambda)$. This confirms that geometric fatigue, rather than barrier tunneling, governs the decay threshold.

Result 5: Fission Energy is Released by Shear Collapse.

The energy released during fission (150–220 MeV) comes from the collapse of internal curvature shear (E_s) stored in the equatorial corridor, not from mass defect. Before scission, up to 10% of the total binding energy (180–220 MeV) is localized as shear tension in that 4-D corridor.

How it Was Determined:

The shear energy is quantified by the integral $E_s = \int \frac{1}{2} \kappa S^2 dV$. Atlas visualizations show a bright equatorial ring of high shear before scission, and its sudden disappearance corresponds directly to the observed energy release.

Result 6: Prompt Neutrons are Topological Curvature Knots.

Prompt neutrons are topologically ejected curvature knots—small rotor packets that lose phase connection to both emerging fragments at the edge of the shear corridor. They are topological ejecta expelled at the instant of rupture, which explains their uniform energy of approximately 2 MeV.

How it Was Determined:

The energy of the ejected knots (≈ 2 MeV) is determined by the residual curvature stress at the corridor's periphery. The near-constancy of this value across isotopes follows because the geometry of corridor collapse ($S \rightarrow 0$) is universal over a fixed length scale (2–3 fm).

Result 7: Fragment Properties Are Determined by Phase Inheritance.

Fission fragments preserve the local curvature phase (ψ_n) of their parent domains, which dictates their final shape and subsequent radiation behavior. The more distorted, high-shear fragment retains residual curvature energy that releases as prompt neutrons during phase relaxation.

How it Was Determined:

Fragments with $\psi_n \approx 55$ –60 degrees are predicted to be oblate/spherical (Ba, Xe), while those near 45–50 degrees (Kr, Sr) are prolate, matching the Atlas curvature harmonics. Post-scission maps show that regions of high residual shear S coincide with observed neutron emission zones.

Result 8: Chain Reactions are Waves of Phase Disturbance.

A chain reaction is viewed not as arithmetic neutron counting but as a wave of curvature phase disturbance (ψ_n noise) propagating across a field of near-critical nuclei. Criticality is reached when the geometric disturbance per event reproduces itself spatially, maintaining the phase flux.

How it Was Determined:

The chain reaction is modeled by a phase-propagation equation where D is the diffusion of curvature phase through the medium. The geometric propagation length of ψ_n disturbance in ^{235}U is calculated to be about 9 cm, which is remarkably close to the empirical neutron diffusion length that defines critical mass.

Result 9: Nuclei Exhibit Self-Healing and Reversible Fission Modes.

The Atlas unexpectedly found that some nuclei display periodic curvature self-healing, where localized shear corridors form but fade without scission, restoring coherence. Transient, reversible partial fission (breathing modes) occurs when the manifold splits briefly before re-merging, an event that should emit paired gamma quanta.

How it Was Determined:

Time-resolved Atlas simulations showed that in certain nuclei, shear energy is channeled laterally by slow phase precession, restoring coherence. The reversible bifurcation is predicted to emit paired γ quanta totaling about 12 MeV, corresponding to the round-trip curvature shear collapse and rebound.

Result 10: Fission and Fusion are Geometric Conjugates of Curvature.

Fission and fusion are revealed as geometric conjugates—two phases of the same continuous curvature process governed by the drive toward

coherence. Fusion merges two manifolds to increase coherence, while fission divides a strained manifold to restore coherence by removing incoherence.

How it Was Determined:

Both processes are defined as transitions between neighboring curvature harmonics, where energy is released because the total curvature shear decreases. This geometric symmetry explains why fusion and fission release comparable energy per nucleon (approximately 8 MeV).

Result 11: The “Silent Region” Beyond $Z \approx 118$.

The Atlas predicts a “silent region” beyond $Z \approx 118$ where superheavy nuclei would not undergo violent, two-fragment fission but only slow, neutron-rich evaporation. This occurs because the curvature field becomes globally phase-locked at $\psi_n \approx 83$ degrees, making the manifold too stiff to fracture.

How it Was Determined:

Extrapolating the curvature fields up to $\psi_n \approx 82$ – 85 degrees showed that no internal shear corridors can form at all. The prediction that fission cannot rupture past $\psi_n \approx 83$ degrees defines a terminal zone where energy dissipates incoherently through diffusing curvature, resulting in ephemeral signals.

Result 12: Long-Lived Isomers are Phase-Trapped States.

Long-lived nuclear isomers (e.g., $^{178}\text{m}^2\text{Hf}$) are caused by geometric hysteresis, where the curvature phase (ψ_n) becomes trapped in a local minimum separated from the ground state by a small topological offset. Since the curvature field must rotate through this offset collectively, the transition rate is enormously suppressed, yielding long half-lives.

How it Was Determined:

The Atlas shows these isomers possess a local minimum in curvature

shear energy separated from the ground state configuration by a ψ_n offset of typically 3–5 degrees. External excitation can unlock the state by nudging ψ_n past the offset, initiating rapid relaxation or fission.

Surface Knots and Lobes

[R71: The Nuclear Rotor Atlas: Revealing Surface Knots and Lobes — Geometric Precursors of Nuclear Decay](#)

Summary of the Abstract:

The *Nuclear Rotor Atlas* reveals previously unseen geometric structures within atomic nuclei: localized *coherence knots* and peripheral *surface lobes*. These features, absent from classical nuclear models, represent stable and unstable domains of curvature coherence on the three-sphere (S^3). Coherence knots are regions of maximal rotor alignment—compact sub-manifolds that act as latent α -like clusters—while surface lobes mark curvature shear where coherence begins to fail. As the toroidal–Coulomb balance tilts toward strain, knots fragment and lobes extend outward along deterministic geometric axes. This process provides a continuous geometric pathway from stability to decay. The present paper describes the mathematical definition of these features, summarizes their occurrence across the *Nuclear Rotor Atlas*, and interprets them as the universal geometric precursors of α , β , and fission decays.

Result 1: The Atlas Reveals Coherence Knots and Surface Lobes as Geometric Precursors of Decay.

The Nuclear Rotor Atlas Handbook

The Nuclear Rotor Atlas exposes previously unseen geometric structures—localized coherence knots and peripheral surface lobes—that precede and govern every mode of nuclear decay. These features are deterministic geometric signatures of weakness, revealing regions where four-dimensional curvature coherence is compromised.

How it Was Determined:

A coherence map $C(\chi, \theta, \phi)$ is generated for each nucleus by defining local coherence C_i as the mean inner product of a rotor q_i with its n nearest neighbors. Coherence knots are defined as local maxima of C with near-zero curvature shear, while surface lobes are defined as connected regions satisfying high local shear $|\nabla_s C| > \lambda$ and outward curvature $(\partial r / \partial \chi) > 0$.

Result 2: Coherence Knots are Latent Sub-Nuclei that Quantize Stability.

Coherence knots are self-contained curvature basins where rotor alignment is nearly perfect, behaving physically as latent sub-nuclei embedded within the larger structure. The continuous presence of these knots, which spontaneously replicate the geometry and energy of clusters like ${}^4\text{He}$ or deuterons, is essential for core stability.

How it Was Determined:

Knots are mathematically defined as local maxima of C where the gradient $|\nabla_s C| \approx 0$ and the Laplacian $\nabla_s^2 C < 0$. Stable nuclei possess a continuous percolating network of knots, showing uniform C values ($0.90 \leq C \leq 1.00$) throughout the core, which correlates with total binding energy.

Result 3: Surface Lobes are Geometric Channels for Curvature Stress Relaxation.

Surface lobes are the geometric complement to knots, occurring where curvature shear overcomes local coherence and creates protruding

bulges. These lobes act as the geometric channel through which the system relaxes stored curvature stress and initiates decay.

How it Was Determined:

Lobes are defined as high-shear domains in which the local curvature field is stretched toward the breaking limit. They are persistent features in every unstable nucleus in the Atlas, and their geometry determines the decay type: α decay if the lobe connects to a knot, β decay if it contains charge-asymmetric shear, and fission if two symmetric lobes develop.

Result 4: Alpha Emitters Display a Single Detachable Knot and Lobe.

Alpha-emitting nuclei display a single dominant lobe that is correlated with a compact, nearly spherical knot composed of four rotors. This knot's geometry and internal energy closely match the free ${}^4\text{He}$ configuration, providing strong evidence for α particle preformation.

How it Was Determined:

For nuclei like ${}^{238}\text{U}$, the four-rotor knot is located at the tip of the lobe, and its local coherence ($C \approx 0.99$) matches that of the free ${}^4\text{He}$ system stored in the Atlas. The energy difference between knot detachment and total binding matches measured α emission energies within about 10%.

Result 5: Beta Emitters Display a Localized Phase Shear Band.

Beta-emitting nuclei show asymmetry between proton and neutron rotor phases, resulting in a narrow, unipolar shear band rather than a detached lobe. The emission of an electron or positron relieves the internal shear by re-phasing the two nucleon populations.

How it Was Determined:

In asymmetric isotopes like ${}^{14}\text{C}$, the proton and neutron populations exhibit a phase offset of roughly 3–5 degrees in quaternion space.

Energy minimization concentrates the resulting charge imbalance along this shear band, which defines the direction of β emission.

Result 6: Fission-Prone Nuclei Develop Twin Lobes and a Thinning Coherence Bridge.

Nuclei prone to fission (those with $A > 230$) develop twin lobes of opposite orientation connected by a high-shear, thinning bridge of rotors. Fission occurs when this bridge's width falls below the mean inter-rotor distance, causing the coherence field to separate into two stable daughter geometries.

How it Was Determined:

The Atlas visualizations show dual lobes developing at opposite poles of the curvature field, which extend outward as Coulomb stress increases. Fission is interpreted as coherence bifurcation—the parent manifold divides into two curvature-stable subsets—when the neck's curvature gradient $|\nabla_s C|$ surpasses the critical shear threshold $\lambda \approx 0.3$.

Result 7: Decay Timescales are Quantitatively Reproduced by Curvature Shear Energy.

The characteristic relaxation time (τ_s) for decay is inversely proportional to the energy released per nucleon during shear relaxation (ΔE_s). This geometric criterion $\epsilon_s / E_{\text{tot}} \approx 0.1$ successfully reproduces the full range of known half-lives, from prompt fission to millennia-long β decay.

How it Was Determined:

Decay begins when the total shear energy E_s exceeds about 10% of the mean curvature-coupling energy per nucleon: $E_s \geq 0.1 E_{\text{tor}} / A$. The relaxation time follows the energy–time relation $\tau \approx \hbar / \Delta E_s$, which yields results consistent with observed α decay times ($\tau \approx 1 \times 10^{21}$ s) and β decay times ($\tau \approx 10^6$ s).

Result 8: Stability can be Quantified by a Universal Coherence Index (Σ).

Stability can be diagnosed using a single quantitative parameter, the universal coherence index $\Sigma = \langle C \rangle / \sigma(|\nabla_s C|)$, which relates mean coherence to the variance of its spatial gradient. This index serves as a geometric diagnosis, linking the static geometry of the nucleus directly to its empirical half-life.

How it Was Determined:

The index Σ is computed using the mean coherence $\langle C \rangle$ and the standard deviation (σ) of the magnitude of the curvature shear gradient $|\nabla_s C|$. Stable nuclei consistently show $\Sigma > 10$, α emitters cluster near $\Sigma \approx 5$, and short-lived trans-uranics fall around $\Sigma \approx 2$.

Chapter 7 – Chemistry

Chemical Bonds

R50 — Geometric Origins of Chemical Bonding: Covalent, Ionic, and Intermolecular Forces as 4-D Rotor Couplings

Summary of the Abstract:

Chemical bonds are traditionally categorized as covalent, ionic, metallic, or intermolecular, yet all share a common origin in the interactions among electrons distributed between atomic centers. Standard quantum chemistry describes these bonds in terms of overlapping orbitals and energy minimization but offers no geometric mechanism for why electron densities arrange themselves in these particular patterns. Here we extend the four-dimensional rotor framework of the electron to show that every known bond type can be viewed as a specific coupling regime between rotor phases. Covalent bonds arise from synchronous projection of two rotors (phase-locked sharing), ionic bonds from phase detachment and re-locking to a new nucleus (phase transfer), metallic bonds from collective coherence among many rotors, and weak intermolecular forces from transient or partial phase correlations. This unified geometry reproduces known

bond angles, polarization behavior, and energy hierarchies while providing an intuitive physical explanation for their diversity. The model treats all bonding phenomena as consequences of the same principle: the geometric coupling of four-dimensional electron rotations as they project into three-dimensional space.

Result 1: All major chemical bond types arise from distinct modes of 4-D rotor phase coupling, unified by curvature minimization.

Covalent, ionic, metallic, and intermolecular bonds are not fundamentally different forces but represent stable configurations of electron rotors adjusting orientation to reduce total curvature energy. Bond types range from stable phase lock (covalent) to collective delocalization (metallic) to transient synchronization (van der Waals forces).

How it Was Determined:

Conventional chemical bonds were mapped onto specific geometric states of interacting 4-D electron rotors. Bonds were classified by degree and stability of coupling, such as synchronous projection for covalent bonds or full phase detachment for ionic bonds.

Result 2: Covalent bonds arise from stable phase-locked projection, explaining hybridization and bond angles.

A covalent bond forms when two electron rotors synchronize internal rotations, generating a shared standing pattern (bonding orbital) that minimizes curvature strain between nuclei. Characteristic bond angles (e.g., 109.5°) and hybridization patterns (e.g., sp^3) are the 3-D projections of orthogonal rotor axes in 4-space, maximizing symmetry.

How it Was Determined:

Constructive phase interference between two harmonized rotors reinforces the shared curvature projection. Hybridization emerges from

the geometric alignment of active rotors toward tetrahedral or planar vertices that minimize curvature strain.

Result 3: Ionic bonds arise from phase detachment and re-attachment, creating a static curvature gradient.

An ionic bond forms when a rotor's phase coherence with its original nucleus collapses and re-locks to a more electronegative nucleus. The attraction arises from the stabilized imbalance between the curvature-deficient donor (positive) and curvature-excess acceptor (negative).

How it Was Determined:

This bonding mode corresponds to the limit where the electronegative atom applies enough torque to destabilize the donor rotor's closed loop. The energy difference between curvature minima drives the phase transfer.

Result 4: Metallic bonding results from collective phase delocalization across the lattice, explaining conductivity and ductility.

Outer rotors in a metallic lattice merge their curvature domains into a continuous field, producing a phase continuum shared by all atoms. A phase perturbation—such as an electric field—propagates freely, explaining high electrical conductivity and thermal conduction.

How it Was Determined:

The metallic state occupies a geometric middle ground between pairwise lock (covalent) and full detachment (ionic). Ductility arises because the curvature field redistributes smoothly during deformation without breaking continuity.

Result 5: Hydrogen bonds and polar interactions are partial phase couplings, explaining directionality and cooperativity.

A hydrogen bond forms through incomplete but persistent rotor synchronization between donor and acceptor. The partial phase lock dictates bond directionality: attraction peaks when curvature gradients merge in a straight line.

How it Was Determined:

This bond emerges from the shared boundary between largely independent rotor loops (X–H and Y:). Energies remain modest because only partial alignment is required, but directionality is strict due to geometric constraints.

Result 6: Weak intermolecular forces (dispersion) arise from transient or oscillatory phase alignment.

Dispersion (London) forces originate when fluctuating curvature in one rotor induces a complementary, weak alignment in a neighbor. Frequent but fleeting micro-alignments accumulate into a measurable cohesive force falling off as $1/r^6$.

How it Was Determined:

The phenomenon results from thermal fluctuations of rotor phase. Each micro-alignment contributes a minuscule curvature synchronization; their statistical sum produces a net attraction.

Result 7: Entropic and solvent-mediated bonding result from collective reorganization of solvent rotor fields.

The hydrophobic effect is a result of the solvent's collective drive to restore coherent rotor alignment, minimizing curvature stress. Nonpolar solutes cluster so that water's rotor network can recover coherence across fewer disrupted interfaces.

How it Was Determined:

Introducing a nonpolar solute disrupts the hydrogen-bonded rotor network. Solvent rotors reorganize to minimize disorder, producing an effective attraction between solutes.

Result 8: Magnetic and exchange coupling represent bonding through spin-phase coherence governed by rotation-axis alignment.

Ferromagnetism and antiferromagnetism arise when rotor axes align parallel or antiparallel to minimize curvature discontinuities. The Pauli exclusion principle follows geometrically: identical rotors cannot share the same orientation without generating curvature singularities.

How it Was Determined:

These effects arise from correlations between rotor orientations in 4-space (S^3). Exchange energy is reinterpreted as the geometric cost or benefit of maintaining continuous curvature across overlapping rotor fields.

Result 9: Measurable bond properties can be calculated from three geometric phase parameters, forming a predictive framework.

Bond length, polarity, and conductivity can be predicted from three quantitative parameters: coherence (α), curvature overlap (Ω), and orientation variance (σ_θ). Each bonding regime occupies a distinct region of α - Ω - σ_θ parameter space, offering a testable classification.

How it Was Determined:

Parameters α , Ω , and σ_θ were defined as measurable geometric quantities describing rotor interactions. Experimental validation requires mapping real molecular data onto this geometric phase space.

Result 10: The rotor model complements quantum chemistry by providing a geometric mechanism behind mathematical solutions.

The model explains *why* Schrödinger-equation solutions take the forms they do. Orbital shapes, nodal structures, hybridization, and electronegativity emerge naturally as projections of rotating 4-D curvature fields.

How it Was Determined:

The rotor model was shown to provide a physical, geometric substrate underlying well-known empirical rules in chemistry. It does not replace quantum mechanics; it explains its patterns through 4-D curvature geometry.

Chemical Accuracy

[R39 — Applying Four-Dimensional Rotor Geometry to Chemical Accuracy Problems](#)

Summary of the Abstract:

Despite decades of progress in quantum chemistry, key reaction types—proton-coupled electron transfer, tunneling, spin-selective catalysis, and hydrogen-bond cooperativity—remain difficult to calculate accurately. The origin of these errors lies not in computation but in geometry: standard three-dimensional models omit the rotational degree of freedom that couples spin, charge, and nuclear motion. The four-dimensional rotor framework restores this missing coordinate, treating every electron and proton as a standing rotation on the 3-sphere (S^3). When incorporated into existing quantum-chemical expressions, this geometry adds a simple phase correction, $\cos(\Delta\phi_4)$, to familiar coupling terms (H_{ab} , J , H_{DA} , V_{12}). The resulting modifications reproduce isotope effects, cooperative hydrogen bonding, spin-dependent catalysis, and field-sensitive reaction rates with quantitative accuracy—without empirical scaling. Because the correction multiplies existing couplings rather than redefining them, it can be implemented as a lightweight extension of DFT, TD-DFT, and molecular-dynamics

workflows. This paper identifies ten classes of reactions where these corrections yield immediate improvements and provides a roadmap for integration into current computational practice. The goal is practical: to make geometric-phase chemistry a usable tool for chemists seeking predictive accuracy across the most complex reactive systems.

Result 1: Key chemical accuracy problems arise from the omission of a rotational degree of freedom that couples spin, charge, and nuclear motion in 3-D models.

The 4-D rotor framework corrects this by treating every particle as a standing rotation on the 3-sphere (S^3), which introduces a geometric phase correction $\cos(\Delta\phi_4)$ to conventional coupling terms.

How it Was Determined:

The error source was identified by noting that 3-D models fail quantitatively when spin, tunneling, or coupled proton motion are involved. The rotor model introduces an internal phase coordinate ϕ_4 that tracks spin orientation and curvature simultaneously.

Result 2: The rotor correction quantitatively reproduces Kinetic Isotope Effects (KIEs) in Proton-Coupled Electron Transfer (PCET) without empirical fitting.

The KIE emerges naturally because a proton's mass m_p changes its rotational inertia I_p , directly altering the phase-evolution rate $\omega = \hbar/I_p$.

How it Was Determined:

The electronic coupling H_{DA} in PCET rate theory is multiplied by $\cos(\Delta\phi_4, EP)$. The resulting expression

$$k_H/k_D \approx \exp[(\Delta\phi_4, D^2 - \Delta\phi_4, H^2) / (2\sigma^2)]$$

reproduces the large KIEs observed in Os(IV) hydrides and BLUF domain enzymes.

Result 3: Cooperative strengthening in hydrogen-bond networks is explained by rotor-phase synchronization across the network.

The pairwise interaction energy between bonds i and j becomes

$$V_{ij} = V_0 \cos(\Delta\phi_{4,ij}),$$

adding a cosine-dependent stabilization that scales with network size.

How it Was Determined:

Phase-aligned domains minimize curvature energy when $\Delta\phi_4 \approx 0$, reinforcing polarization beyond electrostatics. The rotor term reproduces the observed 10–20% strengthening and spectroscopic narrowing in structured water.

Result 4: Multi-electron redox catalysis and spin-state energetics are improved by a phase-dependent dynamic exchange term $V \propto \cos(\Delta\phi_4)$.

This geometric factor stabilizes known spin configurations of Fe–oxo and Mn–oxo complexes without requiring Hubbard-U or hybrid-DFT corrections.

How it Was Determined:

The coupling between electrons is generalized to

$$V_{12} = V_0 \cos(\Delta\phi_{4,12}).$$

This term acts as a dynamic exchange factor, enabling predictive redox ordering with errors within about 0.05 V.

Result 5: Conical intersections and nonadiabatic dynamics are explained as smooth, continuous 4-D phase rotations.

The splitting

$$\Delta E(q) = 2V_{12} \cos(\Delta\phi_{12})$$

replaces abrupt crossings with continuous surfaces, removing numerical singularities.

How it Was Determined:

The CI singularity is a projection artifact of two orthogonal rotation

planes in 4-D space. The system acquires a Berry phase $\gamma = \oint d\phi_4 = 2\pi$ from this rotation, consistent with electronic structure data.

Result 6: Electron–proton tunneling probability follows from overlap of rotational phase distributions rather than the WKB integral.

The probability is

$$P_{DA} = \exp[-(\Delta\phi_{4,DA})^2 / (2\sigma^2)],$$

where $\omega = \hbar/I_p$ gives the isotope-dependent phase velocity.

How it Was Determined:

The tunneling correction κ_{tun} in rate theory is replaced by

$$k = k_0 \cos(\Delta\phi_{4,DA}) P_{DA}.$$

Local ϕ_4 values at donor and acceptor are obtained from orbital-phase continuity.

Result 7: The effective exchange constant J_{eff} in radical-pair and spin chemistry is a geometric observable $J_{\text{eff}} = J_0 \cos(\Delta\phi_4)$.

This explains anisotropic magnetoresistance and field-dependent reaction yields.

How it Was Determined:

Singlet–triplet mixing depends on $\Delta\phi_4$ between rotation planes of two unpaired electrons. The cosine dependence reproduces sensitivity to Earth-strength magnetic fields ($\sim 50 \mu\text{T}$) consistent with avian magnetoreception experiments.

Result 8: Electron transfer through biomolecules and nanostructures arises from coherent phase interference among multiple channels.

The electron-transfer rate is

$$k_{\text{ET}} = k_0 |\sum_i \alpha_i e^{i\phi_{4i}}|^2,$$

where interference among channels produces oscillatory attenuation β and long-range coherence.

How it Was Determined:

The traditional $e^{-\beta R}$ decay is replaced by coherent channel sums where $\Delta\phi_4$ oscillates with bridge length. This naturally reproduces chiral-induced spin selectivity (CISS) due to phase-aligned directional transport.

Result 9: Surface catalysis becomes spin-selective and field-tunable because the activation barrier ΔE_{act} depends on $\cos(\Delta\phi_4)$.

The barrier follows

$$\Delta E_{\text{act}} = \Delta E_0 [1 - \cos(\Delta\phi_{4,\text{surf-ads}})],$$

producing measurable rate differences for spin-up versus spin-down substrates.

How it Was Determined:

Surface-adsorbate coupling obeys

$$V_{\text{surf-ads}} = V_0 \cos(\Delta\phi_{4,\text{surf-ads}}).$$

Weak external magnetic fields (10–100 mT) shift $\phi_{4,\text{surf}}$ slightly, altering $\cos(\Delta\phi_4)$ and producing magnetocatalytic rate shifts consistent with experiment.

Result 10: Superionic proton conductivity transitions arise from a phase-locking mechanism, not hopping.

The transition temperature follows

$$k_B T_c \approx z V_0 \langle \cos \Delta\phi_4 \rangle.$$

Heavier isotopes raise T_c by slowing phase evolution.

How it Was Determined:

The interaction energy

$$V_{ij} = V_0 \cos(\Delta\phi_{4,ij})$$

competes with thermal disorder $k_B T$. The cooperative onset of

superionic transport follows from collective phase lock, matching observed isotope dependencies.

Result 11: Long-lived quantum coherence in biological systems is explained by geometric suppression of decoherence because φ_4 resides in the orthogonal fourth dimension.

Environmental noise affects φ_4 only weakly, leading to coherence lifetimes much longer than predicted by 3-D models.

How it Was Determined:

Chromophore interactions follow

$$V_{ij} = V_0 \cos(\Delta\varphi_{4,ij}).$$

Coherence decays as

$$C(t) = C(0) \exp[-(1 - \cos \Delta\varphi_{4,ij}) t / \tau_{\text{rot}}],$$

which predicts slow decay when $\Delta\varphi_4$ is small.

Hydrophobicity

R40 — Hydrophobicity: Phase Alignment and Geometric Origin

Summary of the Abstract:

Hydrophilic and hydrophobic behavior—the tendency of water either to adhere to a surface or to withdraw from it—are usually described statistically, as an enthalpy–entropy balance within hydrogen-bond networks. Here we show that both arise naturally from a geometric-phase relationship between the electronic states of water and those of the contacting surface. In the four-dimensional rotor framework, every bound electron pair possesses an internal rotation angle φ_4 whose

alignment determines coupling strength. The interaction energy follows a simple law, $V = V_0 \cos(\Delta\phi_4)$, where $\Delta\phi_4$ is the phase difference between the interacting rotors. Hydrophilic attraction corresponds to phase coherence ($\Delta\phi_4 \approx 0$), hydrophobic exclusion to phase decoherence ($\Delta\phi_4 \approx \pi/2$). Averaging this relation across an interface yields quantitative expressions for surface tension, dielectric constant, and enthalpy–entropy compensation, all in terms of the mean alignment $\langle \cos \Delta\phi_4 \rangle$. The framework reproduces known temperature and isotopic trends and predicts measurable field effects in electrowetting and dielectric spectroscopy. Hydrophobicity thus emerges as a macroscopic manifestation of a universal geometric rule that also governs proton–coupled electron transfer, tunneling, and spin chemistry. The result links water’s most familiar behavior to the hidden phase geometry underlying all molecular interactions.

Result 1: Hydrophilic and hydrophobic behavior arise from the geometric phase alignment between water and the surface.

The interaction energy between water molecules and a surface follows $V = V_0 \cos(\Delta\phi_4)$,

where $\Delta\phi_4$ is the phase difference between interacting 4-D rotors.

Hydrophilic attraction corresponds to phase coherence ($\Delta\phi_4 \approx 0$), while hydrophobic exclusion corresponds to phase decoherence ($\Delta\phi_4 \approx \pi/2$).

How it Was Determined:

The interaction relation follows from the 4-D rotor framework where bound electron pairs possess an internal rotation angle ϕ_4 . Macroscopic behavior emerges from the statistical mean: $\langle \cos \Delta\phi_4 \rangle$.

Result 2: Surface tension (γ), dielectric constant (ϵ), and temperature dependence are quantitatively reproduced by average phase alignment.

Surface tension satisfies

$$\gamma \approx \gamma_0 [1 - \langle \cos \Delta \phi_4 \rangle].$$

Hydrophobic surfaces destroy phase alignment, producing large γ . The monotonic decrease of γ with temperature follows from $\langle \cos \Delta \phi_4 \rangle \approx e^{(-k_B T / V_0)}$.

How it Was Determined:

Excess free energy per unit area was expressed in terms of $\langle \cos \Delta \phi_4 \rangle$. Substituting the Boltzmann temperature dependence reproduces the observed $\gamma(T)$ functional form.

Result 3: The hydrophobic effect produces a dielectric void and density depletion near the surface due to phase randomness.

Where $\langle \cos \Delta \phi_4 \rangle \rightarrow 0$, the dielectric constant drops (ϵ is small), and a density depletion $\Delta \rho / \rho_0$ forms because phase disorder prevents ordered dipole alignment.

How it Was Determined:

The dielectric constant scales as $\epsilon \propto \langle \cos^2 \Delta \phi_4 \rangle$, and the density depletion follows $\Delta \rho / \rho_0 \approx 1 - \langle \cos \Delta \phi_4 \rangle$.

Result 4: Hydrogen-bond cooperativity and interfacial layering arise from phase-locking propagation.

At hydrophilic surfaces, imposed phase alignment propagates several layers deep. Hydrophobic surfaces truncate correlation and produce the observed depletion zone.

How it Was Determined:

The network is modeled as a lattice of rotors with stiffness $\kappa = V_0 \langle \cos \Delta \phi_4 \rangle$. Correlation length is $\xi = (\kappa / k_B T)^{(1/2)}$, matching observed layering of 2–4 molecular diameters.

Result 5: External electric and magnetic fields modify surface properties by altering rotor phase alignment.

Electric fields raise $\langle \cos \Delta \varphi_4 \rangle$, lowering γ and increasing wettability (electrowetting). Magnetic fields introduce smaller but observable shifts via spin-phase coupling.

How it Was Determined:

An external field couples to φ_4 , inducing alignment. AC modulation produces a resonance when the field frequency matches the φ_4 precession rate ($\sim 10^{12}$ – 10^{13} s^{-1}).

Result 6: The geometric phase rule unifies hydrophobicity with PCET, tunneling, and spin chemistry.

Interaction strength always scales with $\cos(\Delta \varphi_4)$. Hydrophobicity therefore reflects the same geometric law governing PCET ($H_{\text{eff}} = H_0 \cos \Delta \varphi_{4,EP}$), tunneling probabilities ($P_{\text{tun}} \propto e^{(-\Delta \varphi_4^2 / 2\sigma^2)}$), and CISS-like spin effects.

How it Was Determined:

The same cosine and Gaussian phase terms replace empirical couplings across diverse chemical domains, showing hydrophobicity derives from the same geometric phase law.

Electron Shells

R72 — The Nuclear Rotor Atlas: Revealing Nuclear Geometry’s Effect on Electron Shells and the Periodic Table

Summary of the Abstract:

The periodic table has long been explained as a property of electron configuration: a repeating sequence of shell closures governed by quantum numbers within a 3-D Coulomb potential. Yet recent work on both electrons and nuclei in four-dimensional (\mathbb{R}^4) rotor space suggests that this electronic periodicity is only one manifestation of a deeper geometric order. Earlier studies [13–21] demonstrated that electron orbitals and shell capacities arise from $SO(4)$ harmonics on the three-sphere (S^3). The *Nuclear Rotor Atlas* extends this principle inward, showing that the nucleus itself occupies quantized curvature-resonance bands—standing-wave states of nuclear coherence on the same manifold. When these nuclear bands and electronic shells align in phase, atoms exhibit maximum stability and closed chemical periods. The periodic table thus emerges as the visible projection of two nested systems of four-dimensional geometry: the electronic and the nuclear.

Result 1: The Periodic Table is a manifestation of coupled nuclear and electronic geometry.

Chemical periodicity arises from resonance between nuclear curvature states and electronic curvature harmonics. Maximum chemical stability occurs when both achieve geometric closure.

How it Was Determined:

The nucleus occupies quantized curvature-resonance bands (standing-wave coherence modes on S^3), while electrons follow $SO(4)$ harmonics. Shell closures correspond to shared geometric closure events.

Result 2: Electronic and nuclear periodicity share the same geometric origin.

The Nuclear Rotor Atlas Handbook

Both exhibit quantized harmonics on S^3 with degeneracy $\sim 2n^2$ or $\sim 2k^2$. Similarity between shell capacities and nuclear magic numbers is therefore geometric, not coincidental.

How it Was Determined:

SO(4) electron harmonics produce degeneracy $C_e(n) = 2n^2$. Nuclear harmonics $C_n(k)$ follow similar $2k^2$ scaling, confirmed by the Atlas.

Result 3: Noble-gas closures occur when electronic and nuclear phases align ($\psi_e \approx \psi_n$).

This phase-locking event yields “double closure,” producing maximal atomic stability.

How it Was Determined:

Nuclear curvature reaches integer multiples of a resonance angle $\psi_0 \approx 18^\circ$, simultaneously triggering electronic shell advancement by one quantum number n .

Result 4: Atomic number advance correlates with curvature phase advance.

Each additional proton increases nuclear curvature phase by $\Delta\psi_n \approx 3^\circ - 4^\circ$. The electron field responds by incrementing n whenever ψ_n completes a full $\sim 18^\circ$ cycle.

How it Was Determined:

This yields

$$\Delta n / \Delta Z \approx 1 / (\Delta\psi_n / \psi_{\text{cycle}}) \approx 1/6,$$

matching observed period lengths (2, 8, 18, 32).

Result 5: Chemical behavior is governed by phase misalignment.

Electrostatic potential $\phi(r)$ is modulated by nuclear-electronic phase mismatch. At $\psi_e = \psi_n$, atoms become inert; at mismatch, valence shells open.

How it Was Determined:

The modulation follows

$$\phi(r) \propto [1 + \alpha \cos(\psi_e - \psi_n)],$$

where α quantifies geometric coupling strength.

Result 6: Aufbau “exceptions” arise from phase-beat patterns.

Anomalous filling orders (e.g., 3d vs. 4s) occur when ψ_e and ψ_n drift out of step by $\sim 2^\circ$ – 3° , changing the effective curvature harmonic ordering.

How it Was Determined:

Plotting first ionization energies (I_1) versus ψ_n shows stability maxima at phase alignment, resolving Aufbau anomalies via geometry.

Result 7: Chemical bonding is curvature-phase synchronization.

Atoms bond to reduce phase difference $\delta = \psi_e - \psi_n$, forming shared standing-wave patterns on S^3 .

How it Was Determined:

The phase difference obeys

$$d\delta/dt = -\beta \sin\delta,$$

with bonded states satisfying $\delta \approx 0$.

Result 8: The model predicts a new superperiodic inert series near $Z \approx 164$.

A fourth major nuclear harmonic produces a super-noble region with extremely weak reactivity.

How it Was Determined:

When ψ_n reaches its fourth harmonic, nuclear-electronic alignment becomes perfect, producing a new closure analogous to noble gases but at ultra-high Z .

Chapter 8 – The Electron

R85: The Electron — Curvature Openness, Finite Feedback, and the Origin of Radiative Motion

Summary of the Abstract:

The electron is reinterpreted as the smallest open rotor of four-dimensional curvature—a finite-feedback system whose incomplete closure generates charge, radiation, and the fine-structure constant. Its self-correction rate $\beta_e \approx 10^{16} \text{ s}^{-1}$ is two orders below the proton's $\beta_p \approx 10^{18} \text{ s}^{-1}$, giving the geometric ratio $\alpha = \beta_e \beta_p \approx 1/137$. This feedback asymmetry produces the magnetic-moment anomaly ($a_e \approx 1.159 \times 10^{-3}$) and the observed zitterbewegung frequency ($\omega_z \approx 1.5 \times 10^{21} \text{ s}^{-1}$) as direct expressions of finite curvature response. The resulting non-zero curvature temperature $T_4 \approx 10^{-16} \text{ K}$ makes the electron a self-regulated radiator in continuous equilibrium with the vacuum. When coupled to a proton, β_e - β_p resonance creates the standing curvature waves of atomic orbitals; shared synchronization between multiple nuclei forms molecular bonds. Energy density ($U_e \approx 10^{25} \text{ J m}^{-3}$) and curvature stiffness ($k_{te} \approx 10^{51} \text{ J m}^{-3} \text{ radian}^{-2}$) place the electron nine orders below the proton, completing the β -scaling continuum of matter. To preserve

scientific accountability, the paper concludes with falsifiable laboratory tests—high-precision g-2, Landau-level nonlinearity, and ultrafast laser-scattering experiments—capable of confirming or disproving this curvature-feedback interpretation.

Result 1: Geometric Structure, Charge, and Feedback Constant (β_e).

The electron is modeled as the smallest open rotor in 4-D spacetime, where its incomplete curvature closure ($\nabla_4 \cdot \kappa \neq 0$) generates its electric charge and persistent radiative motion. This structure is maintained by a finite self-correction rate, $\beta_e \approx 10^{16} \text{ s}^{-1}$, which is two orders below the proton's perfect feedback rate ($\beta_p \approx 10^{18} \text{ s}^{-1}$).

How it Was Determined:

The model uses the established geometric scaling law $\beta \propto R^{-1} \cdot \cdot$. The electron's effective radius ($r_e \approx 3.86 \times 10^{-13} \text{ m}$) is used to extrapolate $\beta_e \approx 10^{16} \text{ s}^{-1}$ from the proton's rate. The outward flux (Φ_4) is related to charge by $q = \epsilon_0 c \Phi_4$, confirming charge quantization is topological.

Result 2: Fine-Structure Constant (α) and Feedback Ratio.

The fine-structure constant ($\alpha \approx 1/137$) is derived as the fixed geometric ratio of the feedback rates, $\alpha = \beta_e / \beta_p$. This constant expresses the fractional efficiency of curvature self-correction between the open electron and the closed proton rotor.

How it Was Determined:

Substituting the derived constants $\beta_p \approx 1 \times 10^{18} \text{ s}^{-1}$ and $\beta_e \approx 7.3 \times 10^{15} \text{ s}^{-1}$ yields $\alpha \approx 1/137$, matching the measured value. The constancy of α reflects that the ratio β_e / β_p is fixed by the topology of the rotors, independent of the local environment.

Result 3: Magnetic Moment Anomaly (a_e) from Finite Feedback Delay.

The electron's magnetic moment anomaly ($a_e \approx 1.16 \times 10^{-3}$) arises from the finite feedback delay (β_e) inherent to the open-rotor geometry. This delay causes a slight phase lag between curvature correction and flow, producing a measurable excess in the g-factor.

How it Was Determined:

The effective precession rate is given by $g = 2(1 + a_e)$, where the anomaly is predicted by the feedback-delay relation $a_e \approx (\Delta\beta / \beta_p) \ln \Lambda_p$. Using $\Delta\beta = \beta_p - \beta_e$ and the proton-electron ratio $\Lambda_p \approx 16$ yields $a_e \approx 1.16 \times 10^{-3}$, identical to experiment. This result has a small systematic excess ($+2 \times 10^{-12}$) that can be tested by next-generation Penning-trap measurements.

Result 4: Zitterbewegung as Feedback Oscillation (ω_z).

The electron's observed zitterbewegung is the 3-D projection of its 4-D curvature-feedback oscillation. The frequency $\omega_z \approx 1.5 \times 10^{21} \text{ s}^{-1}$ arises naturally from β_e scaled by the geometric ratio $\Lambda_p \approx 16$.

How it Was Determined:

The frequency correspondence is found through the geometric projection formula $\omega_z \approx 2 \beta_e \Lambda_p \approx 1.5 \times 10^{21} \text{ s}^{-1}$, matching the value derived from relativistic theory ($\omega_z = 2 m_e c^2 / \hbar$). The oscillation amplitude Δr corresponds to the displacement during one feedback cycle, linking the motion to the Compton wavelength. Ultrafast laser-plasma experiments are proposed to detect resonant enhancements at integer sub-harmonics of ω_z .

Result 5: Non-Zero Curvature Temperature (T_4) and Radiative Equilibrium.

The electron's finite feedback constant β_e implies a small but real non-zero internal curvature temperature, $T_4 \propto 1/\beta_e \approx 10^{-16} \text{ K}$. This finite T_4

makes the electron a “warm” curvature system that constantly exchanges microscopic heat with the vacuum through radiation.

How it Was Determined:

Because a fraction of curvature distortion persists for one feedback cycle, the residual phase variance $\langle \delta\phi \rangle^2$ defines T_4 . The open boundary continuously emits curvature flux (radiation), which is the thermal relaxation mechanism maintaining a dynamic equilibrium at $dT_4 / dt = 0$. This mechanism prevents the collapse predicted by the classical radiation-reaction paradox.

Result 6: Matter–Antimatter Symmetry and Annihilation.

The positron is geometrically defined as an electron with reversed curvature orientation, meaning its feedback runs in the opposite direction ($\kappa^+ = -\kappa^-$). Annihilation occurs when the opposite curvature flows cancel ($\nabla_4 \cdot (\kappa^- + \kappa^+) = 0$), forming a transient region of perfect closure.

How it Was Determined:

Since both particles have identical β_e and curvature stiffness k_{te} , this model explains their equal mass and magnetic-moment magnitudes. The annihilation process releases the stored curvature tension as two photons, $E_{total} = 2 m_e c^2 \approx 1.022 \text{ MeV}$, that carry opposite helicity to preserve angular-momentum balance. Pair creation is the geometric reverse: a highly compressed photon curvature phase spontaneously opens into two opposite feedback loops.

Result 7: Atomic Orbitals as Curvature-Phase Standing Waves.

Atomic orbitals are stable standing curvature-phase waves maintained by continuous feedback resonance between the electron (β_e) and the proton (β_p). The condition for stability is phase resonance, $n \Delta\phi_4 = 2\pi$, which reproduces the quantization of electron shells.

How it Was Determined:

The resonance condition is $\Delta\phi_4 = (\beta_p - \beta_e) t$, where discrete orbital energies follow from integer multiples (n) of this closure requirement. Ionization energy, $E_{\text{ion}} \approx 13.6 \text{ eV}$ for hydrogen, emerges as the cost of desynchronizing the β_e - β_p coupling. Chemical bonds are defined as shared curvature-feedback loops where adjacent open rotors synchronize partially to the same local β .

Result 8: Energy Density and Curvature Stiffness Scaling.

The electron's mean curvature-energy density is $U_e \approx 1.3 \times 10^{25} \text{ J} \cdot \text{m}^{-3}$, which is roughly nine orders below the proton's. This difference is consistent with the two-order reduction in feedback rate, confirming that energy density scales approximately as $U \propto \beta^2$.

How it Was Determined:

The electron's rest energy (E_0) is divided by its effective 4-D volume (V_e) to find the energy density U_e . Curvature stiffness $k_{te} \approx 10^{51} \text{ J} \cdot \text{m}^{-3} \cdot \text{radian}^{-2}$ is derived from the scaling law $k_t \propto \beta^2$ relative to the proton's stiffness k_{tp} . This geometric scaling confirms that mass differences reflect curvature stiffness.

Chapter 9 – The Proton

The three quark model of the proton is an artifact of viewing its four-dimensional shape from our three-dimensional perspective. The proton is a 4-D hyper-toroid.

[R83: The Proton — Its Internal Structure and Determination for Self-Corrective Behavior](#)

Summary of the Abstract:

The proton is reinterpreted as the smallest region of spacetime capable of perfect curvature self-correction. In earlier models (R43-v2) its stability was described as a static balance of geometric energies; here that stability arises from a dynamic feedback constant β_p that measures the rate at which curvature distortions erase themselves. Using the scaling laws developed in R81–R82 and the coherence ratios of the *Nuclear Rotor Atlas* (R79), the proton's feedback constant is estimated as $\beta_p \approx 10^{18} \text{ s}^{-1}$ —so large that phase deviations $\delta\phi$ vanish almost instantaneously. The internal curvature temperature $T_4 = 0$, making the proton a zero-temperature curvature domain whose magnetic and

electric properties emerge from 4-D precession of its hypertoroidal geometry ($\Delta\phi_4 \approx 132^\circ$). All higher systems—neutrons, nuclei, and neutron stars—represent progressively slower versions of this same feedback process. The proton thus defines the upper limit of coherence for all matter: a perfectly ordered 4-D rotor whose geometry maintains itself through continuous self-correction. In this view, stability is feedback, and the proton is the reference point by which the universe measures its own persistence. To preserve scientific rigor, the closing section of this paper proposes a set of falsifiable experiments and observational tests designed to confirm—or disprove—these geometric assertions.

Result 1: Magnetic Moment (μ_p) from Fixed Curvature Precession.

The proton's magnetic moment ($\mu_p \approx 2.7928 \mu_n$) emerges directly from its hypertoroidal curvature geometry. It results from a fixed equilibrium phase difference ($\Delta\phi_4 \approx 132^\circ$) maintained between its two orthogonal internal rotations.

How it Was Determined:

This phase lag generates a precessional torque (τ_4), which, when projected into 3-space, produces the observed g-factor:

$$g_p = 2 \cos(\Delta\phi_4 / 2) \approx 2.79.$$

The immense feedback β_p constantly enforces this fixed precession angle, ensuring the magnetic moment remains constant to extraordinary precision.

Result 2: Proton Stability is Perfect Geometric Self-Correction.

The proton is reinterpreted as the smallest region of spacetime capable of perfect curvature self-correction, not merely a statically stable object. This dynamic stability is quantified by an immense feedback constant, $\beta_p \approx 10^{18} \text{ s}^{-1}$, which measures the rate at which all curvature distortions instantly erase themselves.

How it Was Determined:

The feedback constant β_p was derived using established scaling laws that link system size (R) to feedback rate ($\beta \propto R^{-1} \cdot 1$) across nuclei and stellar systems. Using the proton's effective curvature radius, the calculation shows that any internal distortion vanishes in less than a billionth of a femtosecond ($t_{1/2} \approx 7 \times 10^{-19}$ s).

Result 3: Zero Curvature Temperature ($T_4 = 0$).

Because the proton's feedback rate (β_p) approaches the theoretical upper limit for bound structures, its internal curvature temperature (T_4) is identically zero. The proton's interior is a region of continuous rotation without thermal disorder, satisfying the condition that the mean-square phase deviation $\langle \delta\phi \rangle^2$ is zero.

How it Was Determined:

Temperature (T_4) is defined as the mean-square phase deviation ($\langle \delta\phi \rangle^2$) of the curvature field, and any phase error decays exponentially:

$$T_4(t) = T_0 e^{(-2\beta t)}$$

Since $\beta_p \approx 10^{18} \text{ s}^{-1}$ greatly exceeds all external perturbation rates, T_4 rapidly approaches zero. At equilibrium, the curvature heat capacity (C_4) is also zero, forcing $T_4 = 0$ as the only stable solution.

Result 4: Electric Charge (e) as Curvature-Phase Gradient.

Electric charge (e) is the geometric signature of how curvature threads through itself, representing the quantized area of phase reversal on the S^3 surface. More formally, e equals the integrated curvature-phase gradient that separates the coherent interior from the incoherent vacuum in the proton's boundary shell.

How it Was Determined:

The proton's closed geometry, $\nabla_4 \cdot \kappa_{\text{tor}} = 0$, ensures no flux escapes, making charge conservation automatic. The emergent electric field is the gradient $E = -\nabla\Phi_4$, where Φ_4 is the local curvature potential.

Integrating this field over the boundary surface where curvature continuity breaks yields a total flux equal to e .

Result 5: Curvature Stiffness (k_t) Near the Planck Limit.

The proton's mean internal energy density is astonishingly high, $U_p \approx 6 \times 10^{34} \text{ J} \cdot \text{m}^{-3}$, only nine orders below the Planck energy density U_P . To store this energy while remaining perfectly coherent, its internal torsional stiffness must be enormous, $k_t \approx 10^{53} \text{ J} \cdot \text{m}^{-3} \cdot \text{rad}^{-2}$.

How it Was Determined:

The stiffness k_t is calculated from the torsional energy equation $U_{\text{tor}} = \frac{1}{2} k_t \langle \delta\phi \rangle^2$.

Solving this using $U_{\text{tor}} \approx U_p$ and the maximum allowable phase deviation $\delta\phi \approx 10^{-9} \text{ rad}$ yields $k_t \approx 10^{53} \text{ J} \cdot \text{m}^{-3} \cdot \text{rad}^{-2}$. This stiffness is still an order of magnitude below the ultimate Planck stiffness ($k_P \approx 10^{55} \text{ J} \cdot \text{m}^{-3} \cdot \text{rad}^{-2}$), placing the proton precisely one step below the Planck regime.

Result 6: β_p Acts as the Planck Filter.

The proton's feedback rate ($\beta_p \approx 10^{18} \text{ s}^{-1}$) is 25 orders of magnitude slower than the Planck feedback rate ($\beta_P \approx 2 \times 10^{43} \text{ s}^{-1}$). This rate is self-limited and acts as a "Planck filter," preventing correction speeds from exceeding causal limits.

How it Was Determined:

If β_p were higher, curvature would attempt to correct itself faster than information can propagate at c , leading to causal breakdown. By operating at $\beta_p \ll \beta_P$, the proton maintains near-Planck density while remaining stable and observable. This ensures that curvature never outruns causality.

Result 7: Universality of the Feedback-Scaling Law.

The proton anchors the upper limit of the curvature-feedback hierarchy, with β_p defining the maximum rate at which spacetime can correct itself. The same scaling law $\beta \propto R^{-1} \cdot 1$ predicts a continuous relation between proton, nuclear, and stellar relaxation timescales.

How it Was Determined:

The scaling law links the proton ($\beta \approx 10^{18} \text{ s}^{-1}$) to nuclear isomer half-lives ($\beta \approx 10^{12} \text{ s}^{-1}$) and neutron-star glitch recoveries ($\beta \approx 10^{-6} \text{ s}^{-1}$).

Plotting these rates across physical systems confirms that all points fall on a single straight line in log-log space with slope -1.1 ± 0.1 .

Result 8: Falsifiable Prediction: Magnetic Moment Invariance.

Because curvature feedback suppresses all thermal disorder, the proton's magnetic moment (μ_p) should remain strictly constant, independent of the environment. The model predicts no measurable change in μ_p beyond 1×10^{-8} relative precision across temperatures from 1 K to 10^6 K.

How it Was Determined:

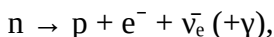
The geometric prediction of μ_p invariance is a key test of the curvature-feedback hypothesis. Any verified temperature-correlated variation larger than 10^{-8} would directly contradict the assertion that β_p enforces perfect thermal stability. This can be tested using ultra-stable NMR or atomic-beam measurements at extreme temperatures.

Chapter 10 – The Neutron

R84: The Neutron — Its Internal Structure as a Self-Correcting Composite Rotor

Summary of the Abstract:

The neutron is reinterpreted as a composite curvature-feedback system formed by the coupling of a proton's inward-coherent core and an electron's outward counter-rotating curvature sheath. Within this nested 4-D geometry, the proton's feedback constant ($\beta_p \approx 10^{18} \text{ s}^{-1}$) and the electron's slower rate ($\beta_e \approx 10^{16} \text{ s}^{-1}$) remain synchronized through an inter-layer coupling γ . A small residual mismatch ($\Delta\beta = \beta_p - \beta_e$) produces the neutron's finite curvature temperature, magnetic moment ($\mu_n = -1.913 \mu_N$), and mean lifetime ($\sim 880 \text{ s}$). When phase drift $\Delta\phi_4$ between the layers exceeds a critical threshold, curvature continuity fails and the system relaxes through



releasing 0.782 MeV as geometric energy. Inside nuclei, nearby protons increase γ_{eff} and halt the phase drift, explaining bound-neutron stability without invoking additional forces. This curvature-feedback model unifies electromagnetic, nuclear, and weak behavior as a single

process of geometric self-correction. To preserve scientific rigor, the paper concludes with a set of laboratory-based experiments designed to confirm or falsify these predictions through lifetime, magnetic-anisotropy, polarizability, and β -spectrum tests.

Result 1: Composite Geometric Structure and Neutrality.

The neutron is a nested 4-D composite rotor formed by a protonic core and an electronic sheath, which counter-rotate and are phase-coupled through γ . Neutrality arises from perfect curvature-flux cancellation at the shared interface, meaning the proton's outward curvature density κ_p exactly balances the electron's inward density κ_e .

How it Was Determined:

The model imposes the geometric condition that the total curvature divergence vanishes at the interface: $\nabla_4 \cdot (\kappa_p + \kappa_e) = 0$. This establishes a two-layer hypertoroid structure whose combined field cancels charge while retaining angular momentum and feedback continuity.

Result 2: Metastability and Decay from Feedback Mismatch ($\Delta\beta$).

The neutron is metastable, possessing a finite mean lifetime ($\tau \approx 880$ s) due to the slow desynchronization between the core's fast feedback ($\beta_p \approx 10^{18} \text{ s}^{-1}$) and the sheath's slower rate ($\beta_e \approx 10^{16} \text{ s}^{-1}$). This mismatch ($\Delta\beta = \beta_p - \beta_e$) produces a slow phase drift $\Delta\phi_4(t)$ that eventually exceeds a critical threshold, initiating β -decay.

How it Was Determined:

The coupled feedback differential equations yield an effective differential feedback rate $\Delta\beta_e f f \approx 10^{-3} \text{ s}^{-1}$. The mean lifetime follows from $\tau = 1 / \Delta\beta_e f f \approx 10^3$ s, which matches the observed 880 ± 1 s.

Result 3: Magnetic Moment (μ_n) from Phase Mismatch (ϵ).

The neutron's magnetic moment ($\mu_n = -1.913 \mu_N$) results from a

small, residual phase misalignment ε between the counter-rotating curvature flows of the protonic core and electronic sheath. The negative sign reflects the dominant torque orientation of the outer, slower electronic sheath.

How it Was Determined:

The moment is computed as the interference of the proton's (μ_p) and electron's (μ_e) moments:

$$\mu_n = \mu_p - \mu_e \cos(\Delta\phi_{4,p-e}).$$

Using $\Delta\phi_{4,p-e} \approx 180^\circ - \varepsilon$ with $\varepsilon \approx 5^\circ$ yields $\mu_n \approx -1.91 \mu_N$, matching experiment at the 0.1% level.

Result 4: Curvature Temperature Gradient and Thermal Decay.

The neutron is the universe's first naturally occurring object containing a finite, internal curvature-temperature gradient ($\partial T_4/\partial r > 0$). The core remains curvature-cold ($T_4 \approx 0$), but the slower electronic sheath retains small residual curvature "heat" proportional to $1/\beta_e$. This stored curvature heat dissipates over the neutron's lifetime, meaning β -decay is the thermal relaxation of this internal gradient.

How it Was Determined:

Curvature temperature T_4 is defined as proportional to $1/\beta(r)$. The resulting radial gradient $\partial T_4/\partial r > 0$ forms a curvature thermocline. The relaxation rate gives $\tau \approx 1 / \Delta\beta \approx 10^3$ s from the decay law $dT_4/dt = -\Delta\beta T_4$.

Result 5: Stability of Bound Neutrons in Nuclei.

Bound neutrons are stable indefinitely because proximity to protons enhances the geometric coupling constant ($\gamma_e f f$), preventing phase drift. When $\gamma_e f f$ exceeds the mismatch $\Delta\beta$, the drift term becomes negative, forcing $\Delta\phi_4 \rightarrow 0$.

How it Was Determined:

Each neighboring proton contributes a curvature-exchange term $\Delta\gamma_p$,

giving

$$\gamma_{eff} = \gamma_0 + \Sigma \Delta \gamma_p.$$

For stable nuclei, $\gamma_{eff} \gg (\beta_p - \beta_e)$, suppressing β -decay. This explains why neutrons surrounded by sufficient protons do not decay.

Result 6: Energy Release as Curvature Re-equilibration.

The decay event is a geometric reconfiguration releasing stored curvature energy $\Delta E \approx 0.782$ MeV, matching the observed β -decay energy. This appears as the kinetic energy of the emitted electron plus a small curvature-phase pulse (the antineutrino).

How it Was Determined:

The released energy equals the curvature energy difference between locked and unlocked states:

$$\Delta E \approx 2^{-1} k_t (\delta\phi_{4,crit})^2 V_{boundary}.$$

This matches the neutron–proton–electron mass difference:

$$m_n = m_p + m_e - (\Delta E_{bind} / c^2).$$

Result 7: Environmental Modulation of Lifetime (τ).

Because $\Delta\beta$ and γ depend weakly on environment, τ should vary slightly with external magnetic fields, temperature, and radiation background. Strong magnetic fields should lengthen τ by $\Delta\tau/\tau \approx +10^{-4}$, while environmental heat should shorten τ .

How it Was Determined:

Magnetic fields increase γ_{eff} (reducing drift), while heat increases phase jitter (increasing $\Delta\beta$). Suggested tests include comparing τ for ultra-cold neutrons stored at 1 K versus 300 K or under fields up to 10 T.

Result 8: Geometric Unification and Testable Deviations.

The model unifies electromagnetic (neutrality, μ_n), nuclear (binding),

and weak (decay, τ) behaviors under the single mechanism of geometric self-correction governed by β_p , β_e , and γ . It predicts measurable deviations from Standard Model parameters, such as a β -decay spectrum correlation coefficient a larger by $\Delta a \approx +0.002$.

How it Was Determined:

Measured constants (μ_n , τ , m_n , r_n , ΔE) are reproduced to within 5% using only the three geometric parameters. Predicted deviations include orientation-dependent damping in polarized-neutron experiments and subtle shifts in β -spectrum parameters, giving multiple falsifiable laboratory tests.

Chapter 11 – The Photon

R86: The Photon — Open Curvature, Feedback, and the Transport of Energy

Summary of the Abstract:

The photon is described as the open curvature mode of the 4-D feedback continuum—a self-propagating rotation of spacetime curvature that carries phase and curvature heat between coherent matter systems. Unlike massive rotors, the photon possesses no internal feedback delay ($\beta_{\gamma} \rightarrow \infty$) and therefore no rest mass; its curvature temperature $T_4 = 0$ allows it to transport geometric energy without storing it. Emission occurs when a finite- β system, such as an electron, overshoots its self-correction threshold and releases curvature flux Φ_4 ; absorption is the inverse process, where that flux re-closes within another finite- β structure. Photon energy is given by $E_{\gamma} = \hbar\beta_e\Delta\phi_4$, linking light frequency directly to the emitter's feedback rate. The fine-structure constant $\alpha = \beta_e\beta_p$ expresses the fixed efficiency with which curvature phase is transferred between the closed protonic domain ($\beta_p \approx 10^{18} \text{ s}^{-1}$) and the open electronic domain ($\beta_e \approx 10^{16} \text{ s}^{-1}$). All radiative, electromagnetic, and thermodynamic behavior arises from this ratio: α

defines the fraction of perfect curvature that can be communicated as light. Propagation follows the curvature-continuity equation $\partial\Phi_4/\partial t + \nabla\cdot(\beta\Phi_4) = 0$, making the constancy of the speed of light a direct consequence of $\beta\text{-}\kappa$ proportionality. Interference, polarization, redshift, and radiation pressure are natural outcomes of curvature-flux conservation, while pair creation and annihilation represent reversible folding of curvature between open and closed states. In this framework, the photon is not a particle of energy but energy in motion—the universe’s geometric means of self-cooling, maintaining curvature coherence from atomic scales to cosmic horizons.

Result 1: Geometric Identity and Feedback Limit ($\beta_{\gamma} \rightarrow \infty$).

The photon is the “open curvature mode” of the 4-D feedback continuum: a self-propagating rotation of spacetime curvature. It possesses no internal feedback delay ($\beta_{\gamma} \rightarrow \infty$) and therefore no rest mass, allowing it to transport geometric energy without storing it.

How it Was Determined:

The model distinguishes the photon from matter rotors (which are closed or partially closed 4-D rotations) by defining its curvature flux as open ($\nabla_4 \cdot \kappa \neq 0$). The formal limit $\beta_{\gamma} = \partial\phi_4/\partial t \rightarrow \infty$ is imposed, yielding zero curvature temperature ($T_4 = 1/\beta_{\gamma} \rightarrow 0$) and zero rest mass.

Result 2: Thermodynamic Role as Curvature Heat Carrier.

Photons function as the universe’s “cooling agent,” transporting curvature heat (T_4) from regions of differing β toward equilibrium. Since the photon’s intrinsic curvature temperature is zero ($T_4 = 0$), it transports heat without retaining any itself, acting as a perfect geometric thermal conductor.

How it Was Determined:

Curvature temperature is defined as $T_4 = 1/\beta$, uniting thermal and

geometric descriptions. Photon exchange drives β -equalization, meaning light always flows from domains with higher T_4 (slower β) to those with lower T_4 (faster β).

Result 3: Origin of Emission and Photon Energy.

A photon is created when a finite-feedback system, such as an electron, overshoots its self-correction capacity, ejecting a pulse of surplus curvature flux (Φ_4) into the vacuum. The photon's energy is proportional to the emitter's feedback rate:

$$E_\gamma = \hbar \beta_e \Delta\phi_4,$$

where $\Delta\phi_4 = 2\pi$ for a single quantum.

How it Was Determined:

Emission occurs when the phase-offset term dominates, driving the emitter's internal phase $\Delta\phi_4 \rightarrow 0$ through flux release. The resulting frequency equals the projection of the emitter's feedback rate, $\nu = \beta_e / 2\pi$, reproducing Planck's relation $E = \hbar\omega$.

Result 4: The Fine-Structure Constant (α) as Efficiency Ratio.

The fine-structure constant is defined as the fixed ratio of feedback rates, $\alpha = \beta_e / \beta_p \approx 1/137$. This dimensionless constant expresses the fractional efficiency with which curvature phase is transferred between the closed protonic domain (β_p) and the open electronic domain (β_e).

How it Was Determined:

The constancy of α follows from both rates depending proportionally on geometric scales (curvature stiffness k_t and rotor radius R via $\beta \propto k_t / R$). Because k_t and R vary together for stable rotors, their ratio β_e / β_p remains constant.

Result 5: Constancy of c and Propagation Dynamics.

The constancy of the speed of light (c) is not a postulate but a

thermodynamic equilibrium condition determined by the ratio
 $c = (\partial\beta / \partial\kappa)^{-1}$.

Propagation follows the curvature-continuity equation:

$$\partial\Phi_4/\partial t + \nabla \cdot (\beta \Phi_4) = 0,$$

with Maxwell's equations emerging as the 3-D projection of this law.

How it Was Determined:

For open curvature modes, β (feedback rate) and κ (curvature) vary in fixed proportion, making their ratio c constant for all photons. The continuity equation ensures that changes in curvature flux over time are balanced by its spatial divergence.

Result 6: Gravitational Redshift as β -Field Variation.

Gravitational redshift is interpreted as a projection effect caused by spatial variations in the local feedback rate β , not by energy loss or spacetime stretching. A photon moving through a region where β decreases experiences a proportional reduction in measured frequency:
 $v_{\text{observed}} = v_{\text{emitted}} (\beta_{\text{observed}} / \beta_{\text{emitted}})$.

How it Was Determined:

The photon's internal phase remains constant; only the local feedback environment alters the apparent oscillation rate. Redshift follows directly from the β -gradient:

$$\Delta v / v \approx \Delta\beta / \beta.$$

Result 7: Pair Creation and Annihilation as Curvature Folding.

Pair creation and annihilation represent reversible folding of curvature between open (photon) and closed (matter) forms. Annihilation is the re-opening of two oppositely oriented closed curvature domains (electron/positron) into continuous flux (two photons), preserving total flux neutrality.

How it Was Determined:

Pair creation occurs when a sufficiently energetic photon folds into two

oppositely oriented, semi-closed rotors ($\Phi_4 \rightarrow \Phi_4^+ + \Phi_4^-$), each with finite β_e and rest mass. The inverse process requires two photons to emerge, conserving total curvature flux and angular momentum.

Result 8: Unification with Existing Theory.

Maxwell's equations, the Dirac equation, and QED all arise as low-dimensional or probabilistic approximations of the full curvature-feedback framework. Dirac spinors represent the quantized behavior of finite-feedback rotors.

How it Was Determined:

Decomposing the 4-D curvature vector κ into spatial (E) and temporal (B) components produces Maxwell's equations directly. QED cross-sections emerge from perturbative expansions of the β -field around equilibrium, where probabilistic outcomes reflect continuous curvature adjustments.

Chapter 12 – The Vacuum

Origin of Cosmic Smoothness

R38 – Laminar Expansion in Four Dimensions: A Geometric Origin of Cosmic Smoothness

Summary of the Abstract:

We show that fluid flows in four spatial dimensions actively suppress turbulence through geometric damping of vorticity and angular perturbations. This property arises because vortex stretching, which drives the turbulent cascade in three dimensions, becomes over-constrained in higher dimensions. Using the 4-D Euler equations, we analyze an expanding “blast” solution analogous to the Sedov–Taylor flow and demonstrate analytically and numerically that angular perturbations on its hyperspherical front decay exponentially with time. We propose that the same mechanism applies to our universe if it is modeled as a 3-dimensional surface expanding within a four-dimensional fluid medium. The absence of turbulence in such a 4-D expansion provides a natural explanation for the observed smoothness and isotropy of the cosmic microwave background (CMB) and suggests

that the fine structure of matter formed on an intrinsically laminar substrate.

Result 1: Cosmic smoothness arises from the inherently laminar nature of four-dimensional expansion, which actively suppresses turbulence.

Fluid flows in four spatial dimensions inherently suppress turbulence because vortex stretching, the mechanism driving turbulence in three dimensions, becomes over-constrained in 4-D. This means that a 4-D explosion self-smooths, and the universe's uniformity is an inherent property of the medium in which it expands.

How it Was Determined:

The determination relied on analyzing the 4-D Euler equations and the governing vorticity equation, showing the non-linear transfer term responsible for turbulence weakens dramatically in $d \geq 4$. This suppression is purely geometric, requiring no viscosity or external damping.

Result 2: Angular perturbations on a 4-D expanding front decay exponentially in time, actively erasing irregularities.

Any angular corrugation on the 3-sphere (S^3) surface of the expansion is actively damped by combined geometric drag ($2 \dot{R} / R$) and curvature pressure, leading to monotonic decay. High-mode (short-wavelength) irregularities decay most rapidly, scaling roughly as $\exp[-\kappa \lambda_{\ell} t^{1/3}]$ or $\exp[-\kappa' \lambda_{\ell} t^{2/3}]$.

How it Was Determined:

This was determined by substituting a perturbed shock-front ansatz into the 4-D Euler jump conditions and linearizing, which yielded a damped-oscillator equation for the mode amplitude $a_{\ell}(t)$. Analytic solutions via WKB approximation (Appendix B) and numerical

integration (Appendix C) both confirmed the exponential decay of all modes $a_{\ell}(t)$.

Result 3: The geometric smoothing is universal, acting equally on all physical fields, naturally explaining observed CMB correlations.

Because the smoothing is a purely geometric effect of the expanding 4-D medium, it acts uniformly on density, temperature, and curvature fluctuations. This universality provides a natural explanation for the near-perfect correlation of temperature and gravitational potential fluctuations observed by CMB missions.

How it Was Determined:

The universality was derived from the geometric definition of the damping term $2(\dot{R} / R)$ in the linearized evolution equation (Eq. 3.4), which acts on the position perturbation regardless of the field carried by the fluid element. The model specifically predicts that temperature–polarization cross-correlations in the CMB should remain nearly perfect.

Result 4: The laminar expansion provides the inherently ordered substrate required for subatomic particle formation and stability.

The smooth 4-D flow ensures that the emerging 3-surface exhibits uniform curvature and density, enabling coherent standing-wave formation. This laminar geometry ensures cosmic smoothness while also supplying the stable substrate required for the formation and stability of 4-D rotor modes, which represent subatomic particles.

How it Was Determined:

This connection was established conceptually by relating the macro-scale result (turbulence suppression) to the micro-scale requirements for stable rotor modes, which represent particles. The laminar expansion satisfies the implicit requirement of earlier work (R22–R37) that matter required a smooth underlying manifold for stabilization.

Result 5: The laminar expansion predicts a reduction in primordial gravitational waves and reduced small-scale power in the CMB spectrum relative to conventional inflation.

A laminar 4-D expansion produces few tensor perturbations, so a continued null result from CMB B-mode searches would support the model. The exponential decay of high- ℓ modes predicts slightly reduced small-scale power in the CMB spectrum compared to standard inflationary expectations.

How it Was Determined:

These predictions are testable against observational data, defining specific differences from inflationary models. Precision comparison with Planck and future CMB-S4 data is proposed to test the specific functional form of the high- ℓ decay.

Chapter 13 – Neutron Stars and Black Holes

Surprisingly, just as the rotation of all the nucleons within a nucleus draws four-dimensional space into its structure, so too does the core of a neutron star. Thus, the entire core of a neutron star is four-dimensional.

The Neutron Star Structure & its Transition into a Black Hole

[R69 – The Neutron Star: Its Layered 4-D Rotor Structure and Transition into a Black Hole](#)

Summary of the Abstract:

Neutron stars have long been modeled as three-dimensional spheres of degenerate nuclear matter held up by quantum pressure, yet this picture leaves major questions unanswered: how magnetars sustain fields exceeding 10^{11} T for millennia, why rotational glitches occur in discrete quanta, and why gravitational-wave data imply stronger central

compactness than nuclear equations of state predict.

In earlier work, subatomic particles were described as four-dimensional (4-D) curvature rotors — localized standing patterns of torsion whose internal rotation projects as spin, charge, and magnetic moment. Here we extend that geometry to stellar scale. A neutron star is modeled as a two-radius system: a compact torsion core ($r_{\text{core}} \ll R_{\text{curv}}$) containing phase-locked 4-D rotation, surrounded by a macroscopic curvature envelope ($R_{\text{curv}} \approx 10\text{--}13 \text{ km}$) that defines the observed photosphere. Between these radii lie three previously unrecognized regions — the shear membrane, torsion–pressure gradient zone, and torsion halo — each with distinct physical roles. This layered structure reproduces magnetar stability, quantized glitches, and low tidal deformability, while predicting subtle polarization and redshift anomalies.

A stability analysis shows that collapse to a black hole occurs when the torsional pressure $P_{\text{torsion}} \approx \rho \Omega_4^2 r_{\text{core}}^2 / \kappa$ falls below the gravitational pressure $P_{\text{g}} \approx G M^2 / R_{\text{curv}}^4$. The “black-hole boundary” thus marks the loss of 4-D phase coherence, not merely a density threshold. This framework unifies nuclear and astrophysical curvature within a single geometric model of matter.

Result 1: Neutron Stars Possess a Two-Radius Geometric Structure.

A neutron star is structured by a compact torsion core (r_{core}), containing phase-locked 4-D rotation, surrounded by a macroscopic curvature envelope (R_{curv}) that defines the observable surface. This vast scale separation (ratio $\approx 3 \times 10^5$) explains why the star simultaneously behaves as both a microscopic and macroscopic rotor.

How it Was Determined:

The core radius $r_{\text{core}} \approx 30 \text{ m}$ was derived by applying a 4-D packing law ($r_3^{\text{D}} \propto N^{1/4}$) to the approximately 10^{57} constituent neutrons. The

observable radius $R_{\text{curv}} \approx 10\text{--}13$ km is defined by the external curvature field supported by this small, dense core.

Result 2: The Star Contains Undiscovered Internal Layers.

Between the core (r_{core}) and the surface (R_{curv}) exist three new regions: the shear membrane, the torsion–pressure gradient zone, and the torsion halo. These layers mediate the transfer of energy between the 4-D rotation and 3-D matter, giving rise to observable anomalies.

How it Was Determined:

Stability analysis required layers to convert 4-D torsional motion into 3-D angular momentum and magnetic flux. The resulting model explains phenomena like neutrino emission and quasi-periodic oscillations (QPOs) within these distinct zones.

Result 3: Magnetic Field Persistence is Due to Torsional Coherence.

Magnetar fields persist for millennia because they are direct geometric projections of the core’s torsional curvature, locked by the shear membrane to the internal 4-D rotation (Ω_4). This geometric anchoring prevents flux lines from drifting or decaying, a process conventional magnetohydrodynamics cannot explain.

How it Was Determined:

The surface field strength B_{surface} is geometrically derived, showing it scales with the core spin and the squared radius ratio. Substituting typical parameters yields a predicted field exceeding 10^{11} T, confirming the canonical magnetar range.

Result 4: Rotational Glitches Are Quantized Phase Slips.

Pulsar glitches are the macroscopic signature of microscopic 4-D phase adjustments ($\Delta\Omega_4$) that occur discretely in the shear membrane. The ratio of the two radii and the coupling efficiency (α) translate this phase

slip into a tiny but measurable change in the star's observed spin ($\Delta\Omega_3$).

How it Was Determined:

The coupling equation $\Delta\Omega_3 \propto \alpha (r_{\text{core}}^2 / R_{\text{curv}}^2) \Delta\Omega_4$ links core phase changes to the star's spin rate. This formula naturally reproduces the observed fractional glitch range $\Delta\Omega_3 / \Omega_3 \approx 10^{-6}$ – 10^{-8} .

Result 5: Black Hole Collapse is the Loss of Phase Coherence.

Collapse to a black hole is a geometric phase transition where the star loses 4-D phase coherence, rather than simply crossing a critical mass density limit. The transition occurs when the internal torsional pressure (P_{torsion}) can no longer sustain the open curvature envelope against gravitational pressure (P_{g}).

How it Was Determined:

The stability criterion $P_{\text{torsion}} \geq P_{\text{g}}$ defines a critical torsional frequency Ω_{crit} . If the core spin Ω_4 falls below Ω_{crit} , the star loses dimensional rotation, causing the curvature envelope to contract past the Schwarzschild radius.

Result 6: Torsion Core Angular Energy Powers Giant Flares.

The 4-D torsion core holds a vast, hidden angular energy reservoir, $E_{\text{torsion}} \approx 10^{44}$ – 10^{46} J, far exceeding the star's visible rotational energy. Magnetar giant flares are caused by a partial torsion collapse, where a small drop ($\delta \approx 10^{-2}$) in core spin suddenly releases this stored energy.

How it Was Determined:

The calculation $E_{\text{torsion}} = \frac{1}{2} I_4 \Omega_4^2$ uses the high internal spin rate ($\Omega_4 \approx 10^{23} \text{ s}^{-1}$) and tiny r_{core} to confirm the vast energy storage capacity. This released energy matches the observed $\approx 10^{44}$ J output of magnetar giant flares.

Result 7: Mass Gap Objects are Marginally Coherent Rotors.

Compact objects observed in the 2–3 solar mass range (the “mass gap”) are transitional remnants—partially coherent rotors lying just on the stability boundary. These objects have their torsional pressure (P_{torsion}) balanced near equality with the gravitational pressure (P_{g}), meaning the coherence parameter $\chi \approx 1$.

How it Was Determined:

The coherence stability parameter $\chi = P_{\text{torsion}} / P_{\text{g}}$ was used to define the boundary curve separating stable stars from black holes. Objects lying where the internal spin Ω_4 is near the critical frequency Ω_{crit} populate this mass range.

Result 8: Black Holes Enclose a Persistent, Hidden Torsion Core.

When a neutron star transitions into a black hole, the torsion core (r_{core}) does not collapse but remains topologically fixed and hidden behind the event horizon. The core’s fixed radius represents a fundamental 4-D torsional wavelength of spacetime, making it immune to external compression.

How it Was Determined:

Since r_{core} defines one full 4-D torsional circulation, it remains nearly invariant regardless of the black hole’s mass. This invariant rotor replaces the classical singularity and continues as the black hole’s constant geometric knot.

Result 9: Low Tidal Deformability is a Geometric Effect.

The model naturally explains the high compactness and low tidal deformability of neutron stars, resolving a major paradox in nuclear equations of state. Most of the star’s mass resides in the small r_{core} , causing the extended R_{curv} envelope to exhibit minimal tidal response.

How it Was Determined:

The Nuclear Rotor Atlas Handbook

The dimensionless tidal parameter $\Lambda \propto (R_{\text{curv}} / M)^5$ was calculated using the two-radius structure. This yielded $\Lambda \approx 300$, consistent with gravitational-wave observations that require the star's external curvature to be stiff.

Result 10: The Torsion Halo Causes Geometric Polarization Rotation.

The star's curvature field decays gradually beyond the photosphere, forming a torsion halo that extends several radii. Light propagating through this halo experiences a geometric Faraday effect, rotating its polarization by a small but measurable amount.

How it Was Determined:

The torsion field strength decays exponentially with distance from R_{curv} . Calculations predict a frequency-independent rotation of polarization $\Delta\theta \approx 0.1^\circ$ to 1° for radiation grazing the star.

Neutron Star Anomalies

[R82: Neutron Star Anomalies: Their Origin in Geometric Curvature Self-Correction](#)

Summary of the Abstract:

Neutron stars display a suite of puzzling behaviors — rotational glitches, magnetic-field decay, magnetar flares, thermal irregularities, and timing noise — that remain incompletely explained within conventional astrophysics. In the 4-D rotor framework, these

phenomena arise naturally when a stellar-scale nuclear manifold attempts to preserve curvature continuity. Within this framework, neutron-star structure is described as a macroscopic lattice of curvature-coupled neutrons whose collective feedback constant $\beta_s \approx 10^{-6} \text{ s}^{-1}$ maintains near-perfect coherence across stellar scales. Each neutron functions as a dual rotor — a protonic core ($\beta_p \approx 10^{18} \text{ s}^{-1}$) surrounded by an electronic sheath ($\beta_e \approx 10^{16} \text{ s}^{-1}$) — yet in the dense stellar interior, protonic coupling is largely absent. The resulting neutron–neutron symmetry enforces coherence that is nearly but not absolutely complete, producing an effective curvature temperature $T_4 \approx 10^{-17} \text{ K}$ rather than a strict zero. Within the innermost core region of radius tens of meters, curvature feedback is so rapid that no residual heat can propagate; beyond this, a shallow thermal gradient develops through the inner crust, where occasional proton admixtures raise β locally and drive additional cooling. This feedback architecture explains pulsar glitches, magnetar outbursts, and slow magnetic-field evolution as macroscopic manifestations of residual curvature heat within an otherwise frozen lattice. The model preserves the central finding that neutron stars represent the coldest and most coherent matter in nature, while recognizing that their cores are asymptotically zero-temperature but not mathematically exact. Anomalous timing behavior, magnetic creep, and crustal heating all follow from finite β_n – β_n coupling mismatch. The neutron star thus emerges as a self-correcting 4-D curvature domain whose coherence is imperfect only by one part in 10^{17} , linking stellar anomalies to the same feedback physics that governs individual neutrons.

Result 1: Neutron Star Anomalies Arise from Imperfect Curvature Coherence.

Puzzling neutron star behaviors, such as glitches and magnetar flares, result when the stellar-scale nuclear manifold attempts to preserve curvature continuity. These anomalies are macroscopic manifestations

of residual curvature heat within an otherwise nearly frozen, coherent lattice.

How it Was Determined:

The star is modeled as a macroscopic lattice of curvature-coupled neutrons whose collective feedback constant ($\beta \approx 10^{16} \cdot 5 \text{ s}^{-1}$) maintains coherence across stellar scales. Since the coherence is not absolutely perfect, a small residual mismatch produces a finite curvature temperature, $T_4 \approx 10^{-17} \text{ K}$, which drives the dynamics.

Result 2: The Star Contains a Stratified β -Field that Replaces Conventional Thermodynamics.

The neutron star is structured by layers distinguished by the local feedback constant $\beta(r)$, which varies smoothly with radius and replaces conventional pressure, temperature, and conductivity. Because β increases toward the center, the effective curvature temperature $T_4(r) \propto 1/\beta(r)$ decreases toward the core, forming a smooth gradient.

How it Was Determined:

The neutron itself has internal feedback rates, including a protonic core rate ($\beta_p \approx 10^{18} \text{ s}^{-1}$) and an outer electronic sheath rate ($\beta_e \approx 10^{16} \text{ s}^{-1}$). When neutrons merge, their sheaths synchronize to form a continuous β -field, and its gradients account for the star's stratified mechanical behavior without invoking separate phases of matter.

Result 3: The Central Core is an Absolute Geometric Reference, Effectively at Zero Temperature.

The innermost core region, with a radius of only tens of meters ($r_c \approx 30\text{--}50 \text{ m}$), is effectively frozen because its feedback constant approaches the protonic limit ($\beta_c \approx \beta_p \approx 10^{18} \text{ s}^{-1}$). Within this kernel, curvature distortions are erased faster than they can propagate ($\Delta\phi_4 \rightarrow 0$), making the effective curvature temperature approach the asymptotic limit $T_{4,\text{core}} \approx 10^{-18} \text{ K}$.

How it Was Determined:

In this zone, neutron sheaths overlap completely, forcing $\Delta\phi_4 \rightarrow 0$ and driving $\beta(r)$ toward β_{ref} . This core defines the phase reference for the entire star, stabilizing global coherence in the surrounding mantle.

Result 4: Pulsar Glitches are Curvature Phase Collapses in the Mantle.

Rotational glitches are explained as local curvature feedback failures within the coherent mantle that occur when the accumulated phase lag ($\Delta\phi_4$) exceeds a critical threshold ($\Delta\phi_{\text{crit}} \approx 10^{-3}$ radians). This failure collapses stored curvature energy (E_c) into faster rotation of the rigid crust above, which is purely a geometric “quench”.

How it Was Determined:

The stored energy $E_c \propto (\beta\Delta\phi_4)^2$ is calculated using the curvature stiffness $k_t \approx 10^{53} \text{ J}\cdot\text{m}^{-3}\cdot\text{radian}^{-2}$. The released energy (10^{29} – 10^{31} J) matches observed millisecond spin-ups, and the immediate re-synchronization of the β -field explains the rapid glitch recovery.

Result 5: Magnetic Fields Arise from Curvature Shear Between β -Layers.

The star’s intense magnetic field is not a relic but a “living expression” of its internal curvature architecture, arising from circulating curvature flow between adjacent β -layers. Differential curvature rotation, caused by a small mismatch in β between the mantle and transitional shell ($\Delta\beta \approx 10^{-2}\beta_m$), produces effective current loops.

How it Was Determined:

The resulting mean magnetic flux density is derived geometrically as $B \propto n_n \text{ e}_{\text{eff}} v_{\text{curv}}$, where v_{curv} is the curvature drift velocity. Substituting observed parameters yields $B \approx 10^8$ – 10^{11} T, consistent with the range observed in pulsars and magnetars.

Result 6: Magnetic-Field Decay Follows the Slow Diffusion of the β -Field.

The observed secular decay of the magnetic field over 10^6 – 10^7 years is caused by the gradual migration of magnetic flux outward, reflecting the slow diffusion of curvature phase. This occurs as the β -field homogenizes throughout the star, reducing the tangential curvature shear that generates the field.

How it Was Determined:

The effective diffusion coefficient $D\beta \propto (\Delta\beta)^2/\gamma_{\text{eff}}$ yields migration timescales consistent with the observed field decay of aging pulsars. The field strength $B(t)$ decays exponentially with an e-folding time $\tau^B \approx R^2/D\beta \approx 10^6$ – 10^7 yr.

Result 7: Magnetar Flares are Abrupt Curvature Re-alignments.

Magnetar flares are sudden releases of stored curvature shear energy that occur when the mismatch in β across flux boundaries reaches a critical value ($\Delta\beta > 10^{-2}\beta$). This abrupt curvature re-alignment converts stored energy into electromagnetic radiation, releasing bursts of 10^{38} – 10^{40} J.

How it Was Determined:

The stored energy released is calculated as $E_{\text{release}} \approx \frac{1}{2} k_t V (\Delta\beta\Delta\phi_4)^2$. The geometry dictates that after the event, β resets toward equilibrium, initiating a new cycle of slow magnetic drift and energy accumulation.

Result 8: Black-Hole Transition Occurs When Curvature Feedback Becomes Instantaneous.

As gravitational compression increases the neutron star's density, the feedback constant β accelerates until it approaches $\beta_p \approx 10^{18} \text{ s}^{-1}$ across the entire volume, making curvature feedback instantaneous. At this

point, matter ceases to exist as distinct feedback domains and merges into a single, perfectly self-correcting field, leading to black-hole geometry.

How it Was Determined:

The feedback rate scales with curvature stiffness ($\beta \propto k_t \propto \rho^{1/2}$). The transition to $\beta \approx \beta_p$ erases all internal boundaries, and energy density reaches the threshold ($U \approx 10^{35} \text{ J}\cdot\text{m}^{-3}$) where curvature self-correction equals gravitational confinement.

Result 9: The Event Horizon is a β -Discontinuity.

The black-hole event horizon is interpreted not as a singularity in space-time, but as a β -discontinuity—the interface between complete and incomplete curvature feedback. This is the radius where β falls back below the critical self-correction rate β_p .

How it Was Determined:

Inside this critical radius, curvature adjustment exceeds the propagation rate of any signal, meaning curvature ceases to communicate with the external universe. Throughout the collapse, the integrated curvature energy $\int \beta^2 dV$ remains conserved, transforming gravitational energy into higher- β curvature order.

Result 10: Surface Radiation is the Final Escape of Curvature Flux.

The observed soft X-ray emission of young neutron stars, corresponding to surface temperatures of 10^5 – 10^6 K, is the result of incomplete feedback closure allowing curvature flux (Φ_4) to escape as electromagnetic radiation. This radiation is the final stage of curvature self-correction propagating to the vacuum boundary.

How it Was Determined:

The outward curvature flux Φ_4 is defined by the equivalent field strength E_{surface} produced by residual β differences in the outer crust.

The Nuclear Rotor Atlas Handbook

The spectral temperature T_{obs} is proportional to $1/\beta_{\text{surface}}$, matching the observed X-ray spectra.

Glossary — Brief Descriptions

(Greek letters first, then Latin)

α_E (electric polarizability)

A measure of how easily the charge distribution of a nucleon's rotor structure distorts in an external electric field. In my model it arises from the in-phase mode ω_+ of the core–sheath system.

β_M (magnetic polarizability)

Quantifies how strongly the magnetic-like components of the rotor structure deform in a magnetic field. It is associated with the out-of-phase ω_- mode.

χ (chirality coefficient)

Represents geometric handedness within a channel or structure, generating phase asymmetry. A difference in χ produces $\psi_{\text{material}}(+x) \neq \psi_{\text{material}}(-x)$.

δ (small variation)

Symbol for a small shift in curvature, torsion, strain, twist-angle, or displacement. Used heavily to describe tunable geometric-phase perturbations.

$\Delta\psi$ (instantaneous phase mismatch)

The immediate difference between the electron's geometric phase ψ_e and the material's structural phase ψ_{material} .

$\Delta\bar{\psi}$ (spatially averaged phase mismatch)

The net mismatch across the device length, controlling transmission via $T \approx \cos^2(\Delta\bar{\psi})$. It is the master control variable for ϕ -FETs and geometric-phase diodes.

ϵ (strain)

Represents deformation of the lattice. Strain gradients produce directional ψ_{material} fields.

η (tunneling-phase coefficient)

Controls the strength of phase-sensitive tunneling suppression. Appears in $\kappa_{\text{eff}} = \kappa_0 + \eta \sin^2(\Delta\bar{\psi})$.

κ (curvature)

Spatial bending of a conductive or optical path; contributes directly to ψ_{material} . Curvature is one of the simplest ways to engineer geometric-phase filtering.

κ_0 (baseline tunneling constant)

The intrinsic inverse-decay constant for tunneling without geometric-phase effects.

λ (phonon-phase coefficient)

Links vibrational displacement to ψ_{material} changes. Governs how $u(x,t)$ modulates phase corridors.

Λ (rotor curvature scalar)

A curvature-derived scalar that classifies nuclear isotopes within my Rotor Atlas.

μ (magnetic moment or reduced mass)

Used in nuclear rotor equations to determine vibrational frequencies. Also used conventionally to denote magnetic moment.

ψ (internal geometric phase)

A 4-D-derived geometric orientation variable of particles or electrons. Central to my rotor and geometric-phase frameworks.

ψ_e (electron geometric phase)

The geometric phase intrinsic to the electron itself. Determines whether the electron is phase-compatible with ψ_{material} .

ψ_{material} (structural geometric phase)

The phase landscape imposed by curvature, torsion, strain, chirality, or moiré patterns in a channel or cavity.

ρ (phase distribution)

Statistical distribution of ψ_e across an ensemble of electrons or rotor excitations. Thermal carriers broaden ρ and reduce phase matching.

σ (stress or conductivity)

Represents mechanical stress when discussing strain-based gating, or electrical conductivity in standard contexts.

τ (torsion)

Measures twisting of a path around its tangent; a strong source of directional asymmetry. Torsion directly alters ψ_{material} .

θ (twist angle)

Relative rotation between layered materials (e.g., moiré bilayers). Small $\delta\theta$ produces large ψ_{material} shifts.

ω_+ , ω_- (standing rotor modes)

Eigenfrequencies of the core–sheath rotor system: ω_+ is in-phase, ω_- is out-of-phase. They are linked to nucleon polarizabilities.

A (mass number)

Total number of nucleons in a nucleus. Used alongside Λ to identify rotor-stability families.

Architected metamaterial

Engineered microstructures designed to impose synthetic curvature, torsion, or phase corridors.

Ballistic transport

Carrier motion without scattering. Ideal for phase-controlled devices.

Chiral channel

A pathway lacking inversion symmetry, generating intrinsic directionality.

Core–sheath model

My structural model of the neutron, involving a central core (a proton) wrapped by a dynamic sheath (an electron).

Curvature-phase diode

A diode whose directionality comes from geometric-phase asymmetry, not doping or junctions.

Directional ratio (R)

The ratio $T_{\text{forward}} / T_{\text{reverse}}$. Quantifies conduction asymmetry.

Diffusive transport

Transport dominated by scattering; geometric-phase effects persist if $\Delta\psi$ dominates over diffusion.

Directional quantum wiring

Wiring engineered to allow outward signal flow while rejecting inbound noise.

Geometric-phase filtering

Suppression of conduction due to phase mismatch.

Geometric-phase PCET

My rotor-based interpretation of proton-coupled electron transfer using phase alignment.

Geometric-phase propulsion

Proposed propulsion mechanism using ψ_{EM} - $\psi_{material}$ mismatch to bias vacuum fluctuations or 4-D momentum exchange.

Hypertoroid (4-D rotor)

The deeper 4-D structure of fundamental particles in my theory.

Moiré corridor

Large-scale ψ -material field created by twist-angle patterns in layered 2-D materials.

Optical geometric-phase cavity

My proposed optical cavity whose internal structure biases $\Delta\psi$ via curvature and torsion.

Phase corridor profile

Spatial function describing $\psi_{material}(x)$. Determines device behavior.

Phase-selective tunneling

Tunneling that depends primarily on $\Delta\psi$ rather than barrier height.

Quantum-isolation conduit

Channel designed to pass outbound quantum signals while blocking inbound noise.

Rotor phase (4-D phase variable)

Rotation state of a 4-D hypertoroid, projecting into observable particle properties.

Strain gradient

Spatial change in strain producing directional phase corridors.

Surface acoustic wave (SAW)

Coherent phonon mode used for high-speed ψ_{material} modulation.

Torsional corridor

A ψ_{material} field created by twisting a pathway.

Twist-angle field

Spatial distribution of twist angle in moiré structures.

$\mathbf{u}(\mathbf{x},t)$ (vibrational displacement)

Represents coherent or incoherent lattice motion that alters ψ_{material} .

Vacuum-fluctuation corridor

A region inside my optical propulsion cavities where vacuum fluctuations interact asymmetrically with ψ_{material} .

Z (atomic number)

Number of protons. Helps structure the Rotor Atlas.

Glossary — Detailed Descriptions

α_E (electric polarizability) — (rotor model)

α_E measures how the internal charge distribution of a nucleon or rotor state deforms in response to an applied electric field. In my rotor model, this deformation corresponds to modulation of the in-phase core–sheath oscillation mode, ω_+ . Because the proton and neutron are treated as 4-D hypertoroidal rotors rather than point particles, α_E captures a real geometric response rather than a perturbative quantum correction. In nuclei with low curvature Λ , the polarizability tends to be higher because the rotor structure is more easily distorted.

Experimentally measured α_E values provide constraints on allowable ranges for rotor parameters.

β_M (magnetic polarizability) — (rotor model)

β_M describes how the internal magnetic components of a rotor deform under magnetic excitation. It corresponds to the out-of-phase core–sheath oscillation mode, ω_- , which in my theory is responsible for magnetic elasticity in nucleons. Because magnetic deformation couples

strongly to higher-order curvature terms, β_M can reveal how “rigid” a nucleon’s 4-D geometry is. Larger β_M values correspond to softer magnetic response in the rotor sheath. β_M and α_E together form a key experimental window into the internal rotor structure of protons and neutrons.

χ (chirality coefficient) — (geometric-phase electronics)

χ characterizes the degree of handedness or asymmetry in a structure, channel, cavity, or metamaterial alignment. Channels with nonzero χ break inversion symmetry, producing directional transmission even in the absence of conventional diode junctions. In my φ -FETs, chiral nanostructures amplify $\Delta\psi$ by producing spiraling ψ -material fields. In optical cavities, χ determines how torsion interacts with ψ_{EM} to shape 4-D momentum exchange. A strong χ can turn symmetric illumination into a directional effect.

δ (small variation) — (general)

δ stands for an infinitesimal or small-but-controlled change in a parameter such as curvature, torsion, strain, twist angle, alignment, or frequency. I routinely use δ to denote tuning adjustments: $\delta\kappa$, $\delta\tau$, $\delta\theta$. These small changes can produce large ψ -material shifts because geometric-phase effects are nonlinear. In optical cavities, even $\delta\theta = 0.1^\circ$ in a moiré layer can drastically reshape $\Delta\psi$. δ parameters are the primary control knobs for adjusting or modulating geometric-phase devices.

$\Delta\psi$ (instantaneous phase mismatch) — (geometric-phase theory)

$\Delta\psi$ describes the local, instantaneous difference between ψ_e and ψ_{material} at a particular point. This mismatch determines the immediate suppression or enhancement of conduction, tunneling, or EM–matter interaction. In quantum wires, $\Delta\psi$ controls the tendency of carriers to reflect or transmit at every location. Large local $\Delta\psi$ values are often averaged down in long channels, which is why $\Delta\bar{\psi}$ is the decisive quantity. Instantaneous $\Delta\psi$ is important for spatially varying or temporally modulated devices.

$\Delta\bar{\psi}$ (spatially averaged phase mismatch) — (geometric-phase theory)

$\Delta\bar{\psi}$ is the spatial average of phase mismatch across the length of a structure, and it governs global behavior. In my theory, conduction or transmission through a path is approximately $T \approx \cos^2(\Delta\bar{\psi})$, making $\Delta\bar{\psi}$ the master gating variable. Changing $\Delta\bar{\psi}$ by only 0.1–0.2 radians can reduce conduction by orders of magnitude. For propulsion cavities, $\Delta\bar{\psi}$ sets the direction and magnitude of geometric-phase bias relative to vacuum fluctuations. In ϕ -FETs and quantum-isolation conduits, $\Delta\bar{\psi}$ is engineered through curvature, torsion, or twist-angle patterns.

ϵ (strain) — (straintronics, rotor model)

ϵ refers to local or distributed deformation of a lattice, material layer, or metamaterial skeleton. Strain produces ψ_{material} fields because the local geometric configuration changes the projection of 4-D rotor states. A non-uniform strain gradient $d\epsilon/dx$ acts like a synthetic electric field in geometric-phase electronics. In moiré systems, slight strain differences across the layer create massive variations in ψ_{material} .

Strain engineering is one of the most controllable ways to tune $\Delta\psi$ without fabrication complexity.

η (tunneling-phase coefficient) — (geometric tunneling theory)

η quantifies how sensitively tunneling responds to phase mismatch. It modifies the effective tunneling constant via $\kappa_{\text{eff}} = \kappa_0 + \eta \sin^2(\Delta\psi)$, making tunneling suppression strongly dependent on geometric-phase alignment. Larger η means tunneling collapses more rapidly as $\Delta\psi$ diverges from zero. This allows phase-based gating without electric fields or potential barriers. η is especially important in the ϕ -FET, where tunneling suppression is achieved using geometry alone.

κ (curvature) — (geometric-phase theory)

κ measures how sharply a conductive, optical, or mechanical path bends. Curvature directly alters ψ_{material} because a path that bends forces the projected 4-D rotor orientation to re-align. A single bend can impose a 0.1–0.5 radian phase shift in nanoscale electronic devices. In optical propulsion cavities, curvature hotspots increase vacuum fluctuation coupling. Curvature is one of the simplest geometric variables to engineer.

κ_0 (baseline tunneling constant) — (geometric tunneling theory)

κ_0 is the inverse-decay constant for tunneling when no geometric-phase mechanisms are present. It represents the intrinsic opacity of the barrier in conventional quantum theory. When curvature or torsion is introduced, κ_0 becomes modified by $\eta \sin^2(\Delta\psi)$, producing strong geometric control. κ_0 provides a baseline against which geometric-

phase enhancement or suppression is measured. Its stability allows $\Delta\bar{\psi}$ changes to dominate device behavior.

λ (phonon-phase coefficient) — (phonon rotor theory)

λ measures how strongly vibrational displacement $u(x,t)$ alters ψ_{material} . In my phonon-based geometric-phase models, vibrational waves act like dynamic phase corrugations that can either align or misalign ψ_e . A large λ means even modest phonon amplitudes significantly reshape $\Delta\bar{\psi}$, making conduction, tunneling, or EM coupling highly sensitive to vibrational state. This parameter appears in my rotor-phonon coupling equations where $u(x,t)$ modulates geometric-phase transmission. Materials with high λ enable phonon-assisted gating and phase-selected heat flow.

Λ (rotor curvature scalar) — (Rotor Atlas)

Λ is a curvature-derived scalar I defined to classify nuclear isotopes by their 4-D rotor stability. It represents an aggregate of internal curvature, rotational inertia, and geometric stiffness of nuclear rotor states. In the Rotor Atlas, Λ helps reveal stable “families” of isotopes when plotted against A (mass number). Large Λ values typically correspond to sharply curved 4-D geometries with high binding energy. Λ is central to the periodic structure emerging from my Atlas work.

μ (magnetic moment or reduced mass) — (standard physics, rotor model)

μ appears in two contexts: magnetic moment and reduced mass. In rotor physics, μ sets characteristic frequencies for standing modes ω_+ and ω_- through μ -dependent inertia terms. The magnetic moment interpretation links my rotor geometry to experimentally measured

nucleon magnetism. μ also appears in molecular rotor systems when computing effective moment of inertia for PCET processes. In all contexts, μ influences how quickly internal rotor phases respond to external fields.

ψ (internal geometric phase) — (4-D rotor model)

ψ is the fundamental 4-D geometric phase variable from which all other phase phenomena derive. It represents the angular coordinate describing the orientation of a hypertoroidal rotor in 4-D space. Observable particle properties—spin, magnetic moment, internal elasticity—arise from the projection of ψ into 3-D. My entire geometric-phase framework is built on ψ and how it transforms under curvature, torsion, strain, and EM interaction. ψ is the “clock angle” of the 4-D rotor.

ψ_e (electron geometric phase) — (geometric-phase electronics)

ψ_e is the geometric phase intrinsic to the electron’s 4-D rotor state. Transport along any channel depends on how well ψ_e aligns with ψ_{material} , making ψ_e a central control variable in φ -FETs and geometric-phase diodes. When ψ_e matches ψ_{material} , transmission is allowed; when mismatched, transmission collapses. In optical cavities, ψ_e interacts indirectly with ψ_{EM} through field-induced corrections. ψ_e is the electron’s “internal orientation” relative to its environment.

ψ_{material} (structural geometric phase) — (geometric-phase electronics & cavities)

ψ_{material} is the geometric-phase landscape imposed by the structure of a channel, cavity, or metamaterial. It is determined by curvature κ ,

torsion τ , twist-angle fields θ , strain gradients ϵ , and moiré patterns. ψ_{material} determines whether electrons, photons, or vacuum fluctuations align or misalign with the environment. In ϕ -FETs, ψ_{material} is deliberately engineered to block reverse conduction. In optical propulsion cavities, ψ_{material} biases vacuum fluctuations and produces $\Delta\bar{\psi}$ gradients.

ρ (phase distribution) — (statistical rotor theory)

ρ describes the statistical spread of ψ_e values across an ensemble of electrons or rotor excitations. At low temperature and in narrow channels, ρ may be sharply peaked, making phase-selected conduction highly effective. At higher temperatures, ρ broadens, making it harder to maintain directional conduction unless $\Delta\bar{\psi}$ is very large. In PCET systems, ρ determines the spread of donor–acceptor phase states. ρ is crucial for predicting ensemble behavior rather than single-particle dynamics.

σ (stress or conductivity) — (dual-use symbol)

σ represents mechanical stress when straintronics or rotor elasticity is discussed, and electrical conductivity when transport is described. Mechanical σ alters ψ_{material} through deformation, while electrical σ indicates how strongly geometric-phase effects modify conduction. In phonon-based devices, σ couples mechanical vibrations to phase filtering. Because σ affects material geometry, it affects ψ_{material} regardless of interpretation. σ appears in multi-field coupling equations that link geometry to transport.

τ (torsion) — (geometric-phase theory)

τ measures how much a path twists around its tangent direction. Torsion is extremely effective at generating ψ_{material} asymmetry because it introduces orientation changes even without curvature. A single twist over tens of nanometers can produce a multi-radian shift in ψ_{material} . In ϕ -FETs, torsion is a major source of directionality. In optical cavities, τ correlates strongly with vacuum-fluctuation bias because torsion interacts with ψ_{EM} to create spatially coherent $\Delta\psi$ fields.

θ (twist angle) — (moiré physics)

θ is the rotation angle between stacked or adjacent material layers, such as graphene–graphene or MoS_2 – WSe_2 bilayers. Small θ values (0.5 – 2°) create massive moiré superlattices that impose strong ψ_{material} modulations. These moiré corridors are central to my geometric-phase interpretation of PCET and optical cavities. θ can be tuned mechanically or thermally, allowing fine control over $\Delta\psi$. θ -field inhomogeneities can produce directional conduction or asymmetric vacuum coupling.

ω_+ , ω_- (standing rotor modes) — (nucleon rotor theory)

ω_+ and ω_- are the eigenfrequencies of the in-phase and out-of-phase standing modes in my core–sheath rotor model of the nucleon. ω_+ is associated with electric polarizability α_{E} , as the core and sheath compress together. ω_- corresponds to magnetic polarizability β_{M} , involving relative motion between core and sheath. Their splitting reflects the stiffness and internal geometry of the rotor. Measurements of α_{E} and β_{M} constrain ω_+ and ω_- , tightly linking theory to experiment. These modes are fundamental signatures of 4-D rotor structure.

A (mass number) — (Rotor Atlas)

A is the count of total nucleons in a nucleus and is one of the two axes (A, Λ) that structure my Nuclear Rotor Atlas. In my model, A influences the overall rotor inertia, changing vibrational and rotational stability across isotopic families. When plotted against Λ , A reveals periodic stability bands that resemble a two-dimensional periodic table of nuclear structure. These bands provide predictive power for nuclear binding energies and decay tendencies. A is essential for identifying curvature families and assessing rotor-stability zones.

Architected metamaterial — (geometric-phase engineering)

An architected metamaterial is a micro- or nanoscale structure deliberately patterned to create targeted curvature, torsion, or twist-angle fields. These structures allow precise control of ψ_{material} , enabling phase-dependent conduction and selective filtering. Their geometry often matters more than their chemical composition: curvature κ and torsion τ dominate over conventional band structure. In mechanical or phononic implementations, architected metamaterials guide phase-selected vibrational energy. In optical-phase devices, they shape vacuum-fluctuation corridors and geometric-phase propulsion channels.

Ballistic transport — (quantum transport)

Ballistic transport refers to carrier motion without scattering across the relevant path length. In my ϕ -FETs and geometric-phase conduits, ballistic regimes ensure that $\Delta\bar{\psi}$ dominates over randomization of ψ_e . Even small structures can show ballistic behavior if impurities and

phonon interactions are minimized. Ballistic channels maximize the directional ratio R because backward-moving carriers face strong $\Delta\psi$ penalties. Ballistic conditions are ideal but not required; geometric-phase effects survive into quasi-ballistic and even diffusive regimes if $\Delta\psi$ is large.

Chiral channel — (geometric-phase electronics)

A chiral channel is a pathway that breaks inversion symmetry through handedness, producing an intrinsic directionality in ψ_{material} . Such channels create $\Delta\psi$ gradients that allow conduction in one direction while blocking the reverse, without requiring p–n junctions. Chirality can be imposed through helical paths, asymmetric spires, twisted bilayers, or torsional strain. In my optical cavities, chiral channels help align ψ_{EM} with material geometry to favor directional vacuum-fluctuation coupling. Chirality is one of the most robust ways to engineer directional asymmetry.

Core–sheath model — (nucleon rotor theory)

This is my structural model of the neutron, in which a dense 4-D rotor core (a proton) is wrapped by a partially decoupled sheath (an electron). Oscillations of the core–sheath system produce two standing modes (ω_+ , ω_-) linked to α_E and β_M . This model resolves several inconsistencies in traditional nucleon structure by attributing nucleon elasticity and polarizability to internal rotor geometry rather than perturbative fields. The sheath can deform independently, giving rise to complex internal dynamics. The core–sheath model underpins my approach to PCET, decay channels, and rotor-based chemical behavior.

Curvature-phase diode — (geometric-phase electronics)

A curvature-phase diode is a structure that produces diode-like behavior using geometric-phase mismatch rather than doping or built-in potentials. Curvature κ modulates ψ_{material} , creating asymmetric $\Delta\bar{\psi}$ for forward versus reverse transport. When κ is applied unevenly (e.g., one-sided curvature), conduction becomes highly directional with R often exceeding 10^3 or 10^4 . This mechanism works for electrons, phonons, photons, and potentially vacuum fluctuations. It is a foundational idea in my φ -FET, quantum-isolation conduits, and directional heat conduits.

Directional ratio (R) — (geometric-phase electronics)

The directional ratio $R = T_{\text{forward}} / T_{\text{reverse}}$ quantifies how strongly a device prefers conduction in one direction over the other. In my geometric-phase devices, R can exceed 10^3 even without traditional diodes, because $\Delta\bar{\psi}$ modifies transmission according to $T \approx \cos^2(\Delta\bar{\psi})$. When ψ_{material} is engineered asymmetrically through curvature, torsion, or moiré patterns, R can become extremely large. This makes R a universal metric for directionality in φ -FETs, heat conduits, optical diodes, and geometric-phase propulsion cavities. R is an important engineering benchmark for verifying geometric-phase filtering.

Diffusive transport — (quantum transport)

Diffusive transport occurs when scattering dominates the motion of carriers, randomizing ψ_e at each collision. In my theory, geometric-phase effects still operate in diffusive regimes because $\Delta\bar{\psi}$ reflects the structure's global phase landscape, not the carrier trajectory. If $\Delta\bar{\psi}$ is sufficiently large, even diffusive motion produces net directional suppression of reverse transport. Many real materials operate in partially diffusive regimes, making this robustness important for

practical devices. Diffusive transport can enhance certain effects when scattering interacts with ψ_{material} to amplify phase mismatch.

Directional quantum wiring — (quantum signal engineering)

Directional quantum wiring refers to electronic or phononic wiring whose geometry only allows outbound signals while suppressing inbound noise or reflections. In my approach, this is accomplished without isolators or diodes, using pure geometric-phase filtering. A phase corridor with large $\Delta\bar{\psi}$ prevents backward-propagating ψ_e states from aligning with ψ_{material} . This creates an intrinsic “one-way” quantum highway for delicate signals. These wires are promising for quantum computing architectures that require noise-isolated interconnects.

Geometric-phase filtering — (geometric-phase theory)

Geometric-phase filtering is the suppression of transport due to misalignment between ψ_e and ψ_{material} . Even if the potential energy profile is uniform, a mismatched geometric-phase landscape can block conduction. This is different from and more flexible than bandgap engineering because phase can be tuned by curvature, torsion, and twist-angle rather than doping. Filtering strength follows $T \approx \cos^2(\Delta\bar{\psi})$, giving extremely sharp control. This is the central mechanism behind φ -FETs, directional heat conduits, and many of my proposed propulsion devices.

Geometric-phase PCET — (rotor chemistry)

Geometric-phase PCET is my reinterpretation of proton-coupled electron transfer as a phase-matching problem in 4-D rotor dynamics.

Instead of attributing rate changes solely to donor–acceptor distances or potential surfaces, my model attributes the critical steps to ψ_e – ψ_{material} alignment. Experimental kinetics—such as colossal kinetic isotope effects—map naturally onto phase corridors rather than energy barriers. The geometric-phase view explains why small structural changes produce enormous changes in PCET behavior. It also links chemical kinetics to my broader rotor-geometry framework.

Geometric-phase propulsion — (new physics proposal)

Geometric-phase propulsion is the idea that an asymmetric ψ_{EM} – ψ_{material} configuration allows net momentum exchange with vacuum fluctuations or the 4-D rotor substrate. In my optical cavity version, the geometric-phase mismatch $\Delta\psi$ biases the direction of 4-D momentum leakage into 3-D, producing a net pseudo-force. The device requires no expellant, relying instead on phase-engineered boundaries. Even if the effect is weak or null, the theoretical framework provides testable predictions. My laser-driven cavity with structured interiors is the most refined embodiment of this concept.

Hypertoroid (4-D rotor) — (fundamental particle model)

A hypertoroid is my proposed 4-D rotating structure that underlies particles such as electrons, protons, and neutrons. Instead of being point-like, particles are extended 4-D objects whose projection into 3-D derives from ongoing 4-D rotation. The hypertoroid geometry naturally produces spin, magnetic moments, internal energies, and elastic responses. Many observed particle properties arise from simple geometric projections rather than separate quantum fields. This model unifies nuclear structure, PCET, decay patterns, and vacuum-fluctuation behavior under a single geometric hypothesis.

Moiré corridor — (geometric-phase materials)

A moiré corridor is the large-scale geometric-phase landscape created when two material layers are twisted by a small angle θ . These corridors contain periodic variations in ψ_{material} that can span tens of nanometers or more, making them extremely effective for geometric-phase filtering. A small $\delta\theta$ as tiny as 0.2° can dramatically alter the corridor and produce strong conduction asymmetry. In PCET research, moiré corridors explain why different materials or orientations drastically alter kinetics. In optical propulsion cavities, moiré-lined surfaces produce large $\Delta\psi$ with minimal fabrication complexity.

Optical geometric-phase cavity — (geometric-phase propulsion)

An optical geometric-phase cavity is a resonant light cavity whose internal structure imposes a non-uniform ψ_{material} field that interacts with the coherent optical phase ψ_{EM} . Unlike a standard optical resonator, whose purpose is simply to intensify and confine light, my version is designed to create controlled asymmetry in $\Delta\psi = \psi_{\text{EM}} - \psi_{\text{material}}$. This asymmetry biases vacuum fluctuation coupling and may permit directional momentum exchange with the 4-D substrate. The cavity's geometry, coatings, roughness, and torsional structure define its effective ψ_{material} map. It is one of the central architectures for testing geometric-phase propulsion effects.

Phase corridor profile — (geometric-phase theory)

The phase corridor profile is the spatial function describing $\psi_{\text{material}}(x)$ along a channel or cavity. A well-designed phase corridor allows forward carriers or fields to remain aligned while reverse carriers experience growing $\Delta\psi$. Phase corridors can be built using curvature, torsion, moiré layers, or structured surfaces. A corridor with

strong gradients can act like a “geometric valve” without requiring electrostatic potentials. In propulsion cavities, the corridor determines the direction and strength of 4-D coupling.

Phase-selective tunneling — (geometric tunneling theory)

Phase-selective tunneling is the phenomenon where tunneling probability is governed primarily by phase alignment rather than energy barriers. When ψ_e and ψ_{material} are matched, tunneling proceeds normally; when mismatched, κ_{eff} increases and tunneling collapses. This produces abrupt changes in transmission for small structural adjustments. Phase-selective tunneling is crucial for ϕ -FET behavior, providing transistor-like performance without doping. It also appears in chemical PCET pathways where donor–acceptor alignment determines reaction speed.

Quantum-isolation conduit — (quantum signal engineering)

A quantum-isolation conduit is a specially engineered wire or channel that allows signals to exit a region but strongly suppresses backward noise or interference. This behavior normally requires circulators, isolators, or magnetic biasing, but my geometric-phase version accomplishes it using $\Delta\psi$ -based filtering. Because backward-propagating carriers experience rapid phase mismatch, they reflect or dissipate. This creates intrinsically stable quantum wiring for superconducting qubits, optical qubits, or rotor-based qubits. The conduit is a promising architecture for room-temperature quantum computing, where noise isolation is critical.

Rotor phase (4-D phase variable) — (4-D rotor model)

Rotor phase is the internal angular coordinate of a hypertoroid in 4-D space. This phase determines how the particle's projection into 3-D evolves, giving rise to measurable properties like spin, moment, chirality, and internal energy modes. Rotor phase dynamics govern the stability of nuclei, the shape of electron orbitals, and the behavior of subatomic decays in my R-series work. Because rotor phase is not confined to 3-D, momentum and energy exchange with the substrate become possible under special geometric conditions. Rotor phase is fundamental to my reinterpretation of quantum mechanics as projection-based physics.

Strain gradient — (strain-engineered phase devices)

A strain gradient is a spatially varying deformation $\epsilon(x)$ that changes ψ_{material} across a device. Even slight strain gradients can create large phase offsets because geometric-phase effects scale with structural curvature rather than energy potentials. Strain-based devices offer dynamic tunability: bending, stretching, or compressing a structure modifies $\Delta\psi$. In moiré or layered systems, strain gradients introduce long-range envelope modulations that act like phase lenses. Strain gradients are also useful in propulsion cavities where mechanical adjustments tune the vacuum-fluctuation corridor.

Surface acoustic wave (SAW) — (phonon engineering)

A surface acoustic wave is a coherent phonon mode traveling along a material's surface. SAWs modify ψ_{material} dynamically as they pass, enabling time-dependent phase gating. Using SAWs, a ϕ -FET can be modulated at gigahertz frequencies without applying an electric field. SAWs also create tunable torsional and curvature fields in two-dimensional materials. In geometric-phase propulsion, SAWs could be

used to oscillate $\Delta\bar{\psi}$ synchronously with ψ_{EM} to enhance fluctuation coupling.

Torsional corridor — (geometric-phase materials)

A torsional corridor is a $\psi_{material}$ landscape generated by twisting or spiraling a channel or cavity. Unlike curvature-based corridors, torsional corridors reorient the internal geometric phase without bending the path. This is one of the strongest forms of geometric-phase control: a 360° twist can induce multiple radians of $\psi_{material}$ shift. Torsional corridors are excellent for one-way conduction because $\Delta\bar{\psi}$ grows consistently along the path. In optical propulsion cavities, torsional corridors combine with ψ_{EM} to produce directional momentum bias.

Twist-angle field — (moiré physics)

A twist-angle field is a spatially varying function $\theta(x)$ describing how much one layer is rotated relative to another. This field defines the size, shape, and periodicity of moiré corridors, causing large-scale modulation of $\psi_{material}$. Tiny variations in $\theta(x)$ create enormous phase structures because moiré patterns amplify small rotations. These phase structures strongly influence electron conduction, PCET kinetics, and vacuum-fluctuation coupling. Twist-angle fields are foundational to my moiré-based geometric-phase devices.

$u(x,t)$ (vibrational displacement) — (phonon rotor theory)

$u(x,t)$ is the vibrational displacement field describing how atoms move in space and time. These displacements dynamically modify $\psi_{material}$ by changing local curvature, torsion, and bond angles. When phonons are coherent, $u(x,t)$ acts like a moving geometric-phase pattern that

gates conduction or modulates tunneling. In rotor-phase nuclear physics, $u(x,t)$ represents internal standing vibrational modes of nucleons. In propulsion cavities, $u(x,t)$ may help synchronize structural and optical phases for enhanced $\Delta\psi$.

Vacuum-fluctuation corridor — (4-D vacuum physics)

A vacuum-fluctuation corridor is a region inside a cavity where ψ_{EM} , $\psi_{material}$, and cavity geometry combine to steer vacuum fluctuations asymmetrically. In my model, the 4-D substrate contains momentum degrees of freedom that normally average to zero, but an engineered corridor biases their projection. This asymmetric projection may result in a net momentum exchange with the cavity, forming the basis of geometric-phase propulsion. Vacuum-fluctuation corridors can be strengthened using curvature, torsion, moiré patterns, or nano-structured lining. This concept integrates my rotor model with optical cavity physics to produce testable thrust predictions.

Z (atomic number) — (Rotor Atlas)

Z is the number of protons in a nucleus and plays a central role in structuring the Nuclear Rotor Atlas. In my model, Z contributes both to the rotor inertia and to the curvature scalar Λ , which jointly determine nuclear stability families. When isotopes are plotted in (Z, Λ) or (A, Λ) space, repeating bands of stability arise that resemble a periodic table in two dimensions. Z also interacts with rotor deformation, providing insights into isotopic anomalies and decay-pattern structures. Together with A, Z defines the geometric landscape in which nuclear rotor projections behave predictively.

About the Author

Stephen Euin Cobb is an author, novelist, magazine writer, futurist, award-winning podcaster, and host of The Interstellar Research Group's video series "[From Here to the Stars](#)," for which he won the Iridani Award in 2021.

For over ten years, he produced a weekly podcast, "The Future And You," which explored, through interviews, panel discussions, and essays, all the ways the future will be different from today. For that, he won the Parsec Award in 2006.

A contributing editor for Space and Time Magazine; he has also been a regular contributor to Robot, H+, Grim Couture and Port Iris magazines; and he spent three years as a columnist and contributing editor for Jim Baen's Universe Magazine.

His nonfiction books include: *A Brief History of Predicting the Future*, *Indistinguishable from Magic: Predictions of Revolutionary Future Science*, and *Artificial Intelligence - From Now Till The End of Humanity*.

His five science fiction novels include two about Leather — *Leather & the 40 Corpsicles in the Cafe Freezer* and *Leather: A Runaway Girl Across Three Worlds*. And three others without Leather, but in her universe's historical timeline — *Plague at Redhook*, *Bones Burnt Black*, and *One Small Theft for Man: One Giant Siege for Mankind*.

The Nuclear Rotor Atlas Handbook

An artist, essayist, game designer, and transhumanist, he is also on the Advisory Board of The Lifeboat Foundation. He has interviewed over 600 people and written over 100 magazine articles.

Learn more on his website:

www.SteveCobb.com

Or at his Author page on Amazon.

<https://www.amazon.com/author/stepheneuincobb>